

HZDR-064

RELAXATION DYNAMICS IN PHOTOEXCITED SEMICONDUCTOR QUANTUM WELLS STUDIED BY TIME-RESOLVED PHOTOLUMINESCENCE

Sabine Zybell

Wissenschaftlich Technische Berichte
HZDR-064 · ISSN 2191-8716

WISSENSCHAFTLICH-
TECHNISCHE BERICHTE

hzdr



HELMHOLTZ
ZENTRUM DRESDEN
ROSSENDORF

Wissenschaftlich-Technische Berichte
HZDR-064

Sabine Zybell

**RELAXATION DYNAMICS IN PHOTOEXCITED
SEMICONDUCTOR QUANTUM WELLS STUDIED BY
TIME-RESOLVED PHOTOLUMINESCENCE**

HZDR

 **HELMHOLTZ
ZENTRUM DRESDEN
ROSSENDORF**

Druckausgabe: ISSN 2191-8708

Elektronische Ausgabe: ISSN 2191-8716

Die elektronische Ausgabe erscheint unter Creative Commons License (CC BY):

Qucosa: <http://fzd.qucosa.de/startseite/>

Die vorliegende Arbeit wurde sowohl als Dissertation an der Fakultät Mathematik und Naturwissenschaften der Technischen Universität Dresden, sowie als Wissenschaftlich-Technischer Bericht des Helmholtz-Zentrum Dresden – Rossendorf mit der Berichtsnummer **HZDR-064** veröffentlicht.

2015

Herausgegeben vom

Helmholtz-Zentrum Dresden - Rossendorf

Bautzner Landstraße 400

01328 Dresden

Germany

Relaxation dynamics in photoexcited semiconductor
quantum wells studied by time-resolved
photoluminescence

DISSERTATION

zur Erlangung des akademischen Grades
Doctor rerum naturalium (Dr. rer. nat.)

vorgelegt

der Fakultät Mathematik und
Naturwissenschaften der Technischen Universität Dresden

von

Dipl.-Phys. Sabine Zybell

geboren am 11.09.1981 in Freiberg

Die Dissertation wurde im Institut für Ionenstrahlphysik und
Materialforschung am Helmholtz-Zentrum Dresden-Rossendorf (HZDR)
angefertigt.

Eingereicht am: 30. April 2015

Erstgutachter: Prof. Dr. M. Helm,
Technische Universität Dresden & HZDR

Zweitgutachter: Prof. Dr. R. Bratschitsch,
Westfälische Wilhelms-Universität Münster

Verteidigung: 28. August 2015

Kurzfassung

Gegenstand der vorliegenden Arbeit ist die Untersuchung der Photoluminenzdynamik von Halbleiter-Quantentöpfen (Quantum Wells), die durch Anregung von Intraband-Übergängen mittels resonanter Laserpulse im mittleren Infrarot- und Terahertz-Spektralbereich verändert wird. Diese Zweifarbenexperimente wurden mit Hilfe eines optischen Aufbaus für zeitaufgelöste Photolumineszenzspektroskopie am Großgerät Freie-Elektronen Laser FELBE am Helmholtz-Zentrum Dresden-Rossendorf realisiert. Zeitlich verzögert zur gepulsten optischen Anregung über die Bandlücke wurden Intersubband- oder Intraexziton-Übergänge in den Quantum Wells resonant angeregt. Die dadurch erreichte Ladungsträgerumverteilung zeigt sich in einer deutlichen Verringerung der Photolumineszenzintensität zum Zeitpunkt des zweiten Anregepulses, die im Folgenden als Photolumineszenz-Quenching bezeichnet wird.

Zunächst wird die Stärke des Photolumineszenz-Quenchings in Abhängigkeit der Polarisationsrichtung des midinfraroten Laserstrahls ausgewertet. Während die Absorption durch freie Ladungsträger für beide Polarisationsrichtungen nachweisbar ist, wird experimentell gezeigt, dass Intersubbandabsorption nur möglich ist, wenn ein Anteil der anregenden Strahlung senkrecht zur Quantum-Well-Ebene polarisiert ist.

Das Photolumineszenzsignal ist überwiegend an der energetischen Position der $1s$ -Exzitonresonanz unterhalb der Bandkante messbar. Die intraexzitonischen Übergangsenergien in Quantum Wells liegen typischerweise im Terahertzbereich. Unter intraexzitonischer $1s$ - $2p$ Anregung erscheint auch auf dieser Energieskala ein abrupter Intensitätsverlust in der langsam abklingenden Photolumineszenztransiente. Erstmals wurde im Photolumineszenzspektrum bei höheren Energien im Abstand der Terahertz-Photonenenergie ein zusätzliches $2s$ -Photolumineszenzsignal detektiert. Eine detaillierte theoretische Beschreibung dieses Problems durch unsere Kooperationspartner Koch et al. von der Phillips-Universität Marburg zeigt, dass unter intraexzitonischer $1s$ - $2p$ Anregung eine effiziente Coulombstreuung zwischen den nahezu entarteten exzitonischen $2p$ - und $2s$ -Zuständen stattfindet. Während der $2p$ -Zustand optisch dunkel ist, kann die $2s$ -Population strahlend rekombinieren, was zu dem besagten $2s$ -Photolumineszenzsignal führt. Die Zeitkonstanten der untersuchten Ladungsträgerdynamik werden durch ein phänomenologisches Modell bestimmt, das die experimentellen Kurven sehr gut abbildet.

Es wird ein Ratengleichungsmodell eingeführt, bei dem die involvierten Zustände auf optisch helle und optisch dunkle Besetzungsdichten reduziert werden.

Darüber hinaus werden mit einem modifizierten Versuchsaufbau die Terahertz-induzierten Photolumineszenzsignaturen von Magnetoexzitonen untersucht. Die Stärke des 1s-Photolumineszenz-Quenchings ändert sich dabei entsprechend der magnetoexzitonischen Übergänge, die im betrachteten Feldstärkebereich zwischen 0 T und 7 T liegen. Für Magnetfelder größer als 3 T sind keine 2s-Photolumineszenzsignale mehr messbar, da durch das externe magnetische Feld die Entartung der 2p- und 2s-Zustände aufgehoben wird.

Contents

Kurzfassung	iii
1 Introduction	1
2 Spectroscopy of semiconductor quantum wells	5
2.1 Quantum well fundamentals	5
2.2 Optical properties	7
2.3 Excitons	10
2.4 Exciton Mott transition	14
2.5 Quantum-well-confined magnetoexcitons	16
2.6 Photoluminescence	18
3 Spectroscopic tools and sample characterization	21
3.1 Titanium-Sapphire laser	21
3.2 Free-electron laser	22
3.3 Streak camera	23
3.4 Experimental setup and pulse synchronization	24
3.5 Magneto-optical system	25
3.6 GaAs quantum well samples	27
3.6.1 Sample 1267	28
3.6.2 Sample DBR42	30
3.6.3 Sample H063	30
4 Photoluminescence dynamics under pulsed intersubband excitation	33
4.1 Photoluminescence quenching under resonant intersubband excitation	33
4.2 Modeling the induced photoluminescence dynamics	35
4.2.1 Photoluminescence transients without quenching	37
4.2.2 Photoluminescence transients with induced quenching	40
4.3 Probing of local lattice heating	41
4.4 Polarization dependent photoluminescence quenching	44
4.5 Summary and outlook	47

5	Photoluminescence dynamics under pulsed intraexcitonic excitation	49
5.1	Resonant THz spectroscopy	49
5.2	Observation of dipole-forbidden exciton transitions	50
5.3	Coulomb-induced state mixing	52
5.4	Characterizing intra-exciton Coulomb scattering in THz excitations	55
5.4.1	Rate-equation model for intraexcitonic transition	57
5.4.2	PL dynamics at the 1s energy and the 2s energy	63
5.5	Summary and outlook	66
6	Magnetic control of excitonic photoluminescence emission	69
6.1	THz induced intra-magnetoexcitonic transitions	69
6.2	Magnetic-field control of THz induced 1s PL quenching	70
6.3	Magnetic-field control of the THz induced 2s PL emission	73
6.3.1	Rate-equation analysis	74
6.4	Comparison between experiment and theory	77
6.5	Summary and outlook	79
	Bibliography	80
	List of figures	88
	List of tables	90
	List of author publications	91
	Acknowledgements	94

1 Introduction

Optical properties of matter are of high scientific interest in fundamental and applied research. Particularly, the electromagnetic response of semiconductors has become a multifaceted research field of continuously growing importance. In the past decades, there was a great development on the fundamental and the technical aspects of spectroscopy. Today, tailored nanostructures can be grown with atomic precision and time-resolved spectroscopy is established from the terahertz to the ultraviolet spectral range corresponding to the wavelength region between 1 mm and 100 nm, respectively.

Semiconductor quantum-well heterostructures are semiconductor layers with several nanometer thickness which are embedded in a different semiconductor material featuring a larger band gap. In order to avoid strain effects and dislocations, the lattice constants of the materials are typically very similar. If the layer thickness reaches nanometer scale, quantum size effects result in modified optical properties and the semiconductor characteristics become size dependent, see e.g., [Bal00]. The new feature of the one-dimensional quantum well potential is the formation of discrete states in the conduction and valence bands, so-called subbands. For many semiconductor materials, interband transitions across the bandgap cover the spectral region between 0.4 μm (GaN) and 5.3 μm (InSb) [Vur01] that corresponds to energies in the order of 1 eV. Another energy scale is covered by the excitation of intersubband transitions where the initial and the final states belong to the same band. For semiconductor quantum wells, the intersubband transitions are typically in the infrared spectral region between 2.5 μm and 250 μm that corresponds to energies between 500 meV and 5 meV. First investigations of strong intersubband absorption were performed in 1985 on highly doped GaAs/AlGaAs multiple quantum wells [Wes85]. Mechanisms that influence intersubband relaxation in quantum wells are interesting concerning the fundamental physics involved and possible device applications. The first observation of intersubband luminescence from a GaAs/AlGaAs superlattice was shown in a resonant-tunneling experiment [Hel89]. Since the 1990s, intersubband transitions determine the functionality of unipolar devices based on heterostructures like quantum well infrared photodetectors (QWIPs) [Sch06a] and quantum cascade lasers (QCLs) [Fai94].

After optical excitation across the band gap, one electron and one hole can form a quasiparticle that exhibits a hydrogen-like spectrum of discrete states close to the fundamental band gap. Those neutral electron-hole pairs with finite lifetimes are known as excitons

with eigenstates that are labeled with a principal quantum number $n = 1, 2, 3, \dots$ and an orbital quantum number $\ell = 0, 1, 2, \dots$ (s, p, d, \dots). In typical semiconductors, the effective electron and hole masses and the permittivity of the material lead to exciton binding energies in the terahertz range which is about 1000 times weaker than the Rydberg energy ($1 \text{ Ry} = 13.6 \text{ eV}$) of a hydrogen atom. Note that the frequency $1 \text{ THz} = 10^{12} \text{ Hz}$ corresponds to an energy of 4.1 meV . Due to these low binding energies, excitonic effects are enhanced at low temperatures. The intraexcitonic transition follow the same selection rules as the dipole transitions in hydrogen atoms. In the past decades, an enormous amount of publications focused on the exciton topic as these pair states have a strong influence on the optical properties of semiconductors [Kir11]. While many results of the unique exciton characteristics have been published, even fundamental questions like the exciton formation time are subject of large controversies [Kum96, Szc04, Koc06]. The dynamical processes of excitons are of particular interest as they determine the speed of devices that are based on excitons in quantum wells.

Radiative interband recombination after optical excitation is called photoluminescence (PL) and is one possibility to induce light emission from a semiconductor material. PL spectroscopy is a well established method and provides fundamental physics information about the sample. In the experiment, light is focused on the sample and the emitted PL emission is spectrally resolved and sent to a detector. Because of the small momentum of the photon, PL measurements are only sensitive to low-momentum states and not suitable to give a universal picture of the exciton dynamics in the system under study. The excitons with finite momentum do not contribute to the PL intensity due to momentum conservation rules, i.e., they are in optically dark states and need to scatter before they can recombine radiatively [Koc06]. Using a pulsed laser source, the transient behavior of the characteristic spectral PL lines is determined by the energetic properties and the dynamical processes of the involved carrier populations. It has been shown that the transient PL signal is strongly influenced by the underlying exciton dynamics even for a negligible excitonic population [Cha03, Hoy05]. Enhanced carrier confinement in a quantum well can be achieved by externally applied fields. It has been found that the combination of PL measurements with electric [Men82, Qui92] or magnetic fields [Sak85, Cer96] modify the emitted radiation and are powerful tools to approach the characteristics of quasi zero-dimensional states.

The purpose of this thesis is the characterization of the relaxation dynamics in photoexcited semiconductor quantum wells by addressing internal transitions that involve optically active and dark excitonic states. A unique experimental technique is established to perform two-color time-resolved PL spectroscopy, where the detection of the transient PL spectra is combined with selective optical excitation processes within the bound states of the quantum well. Optical pulses excite carriers across the band gap while temporally

delayed mid-infrared or terahertz laser pulses excite intersubband transitions, intraexcitonic transitions or transitions within magnetoexcitons, respectively. All the experiments have been performed in the optical labs at the Helmholtz-Zentrum Dresden-Rossendorf with direct access to the beam line of the tunable free-electron laser FELBE. This intense narrowband light source runs in continuous pulsing mode and is suitable for the synchronization with table-top lasers. Results are presented that have been taken on three undoped high-quality quantum well samples that differ by composition and quantum well width. Both, intersubband and intraexcitonic excitation, result in a transient quenching of the PL intensity on a 100 ps time scale starting at the arrival time of the free-electron laser pulse. With a polarization dependent study of the induced dip, free-carrier heating and intersubband transitions are identified as two competing processes that occur under irradiation with resonant mid-infrared laser pulses.

Under resonant intraexcitonic $1s$ -to- $2p$ excitation, a quenching of the excitonic $1s$ PL is observed, which is accompanied by an enhanced PL emission from the $2s$ state clearly separated from the $1s$ PL emission by the photon energy of the THz pulse. This first observation of radiative $2s$ PL signal is an unexpected effect as the direct $1s$ -to- $2s$ excitation is dipole forbidden. The experimental observations are found to be well explained by a microscopic many-body theory developed by our collaborators S. Koch et al. from the Philipps-Universität of Marburg. With this theoretical approach, the terahertz-induced $2s$ PL signature is identified as Coulomb mediated state mixing revealing energetic properties unique to excitons. In a second part of the resonant terahertz excitation experiment, the induced PL features from magnetically confined excitons in quantum wells are investigated. In the modified set up, the GaAs quantum well sample is placed in a magneto-optical cryostat which can generate a magnetic field up to 7 T. With the increase of the magnetic field, the lifting of the $2s$ and $2p$ state degeneracy and the involved reduction of the scattering rate is evidenced by the continuous shrinkage of the $2s$ PL emission strength. By changing the photon energy of the exciting THz pulse, the exciton energy shift is tracked, which is caused by the magnetic field. The observed results show the increase of the energy separation between the excitonic ground and excited state and are compared with calculated transition energies in the magnetic field range between 0 T and 3 T. Additionally, time constants of the carrier dynamics are determined with a phenomenological model based on rate equations that reproduces accurately the experimental curves. In case of the intraexcitonic transitions, we show that the derived functions are also predicted by the theoretical model under certain presumptions.

In summary, internal transitions between subbands and excitonic states in semiconductor quantum wells have been investigated via the change of the photoluminescence dynamics under resonant short pulse excitation with photon energies in the mid-infrared and terahertz spectral range.

2 Spectroscopy of semiconductor quantum wells

In this chapter, photoluminescence spectroscopy of semiconductor quantum wells is introduced. In particular, quantum well fundamentals and optical selection rules are discussed that strongly influence the emission spectra. After optical excitation, free electrons and holes can bind via Coulomb interaction and form excitons. These quasi-particles have different characteristics and the excitonic effects are enhanced in low-dimensional structures. In a last part, the basic characteristics and the induced modification of the energy spectrum by an externally applied magnetic field are introduced.

2.1 Quantum well fundamentals

Optical properties of a bulk material typically do not depend on the size of the studied sample. However, if it comes to nanoscale dimensions, quantum confinement effects play a major role and dominate the spectrum. Nanoscale systems can be classified according to their dimensionality resulting in reduced degrees of freedom of the carrier motion. Typical examples are quantum wells (2D), quantum wires (1D), and quantum dots (0D). The dimensionality changes the linear and nonlinear optical characteristics of a material.

A quantum well is an epitaxially grown heterostructure that consists of a thin layer of a semiconductor material between two layers of another semiconductor with larger band gap. Tailored materials have similar lattice constants in order to avoid strain and defects during the growth process. With techniques like molecular beam epitaxy, thin layers can be grown with high precision resulting in rectangular shaped quantum well potentials. Typical examples are GaAs/ $\text{Al}_x\text{Ga}_{1-x}\text{As}$ quantum wells, where the valence band offset and the conduction band offset vary with the Al doping concentration x , $0 < x \leq 1$. The individual layers are only few atomic layers thick, which results in quantum well widths of typically less than 10 nm. The carriers can move freely in the x,y -layer plane while in the growth direction z , electrons and holes occupy confined states in the conduction and valence band, respectively. The number of confined states and their eigenenergy depend on the conduction and valence band offset, the effective mass, and the layer thickness.

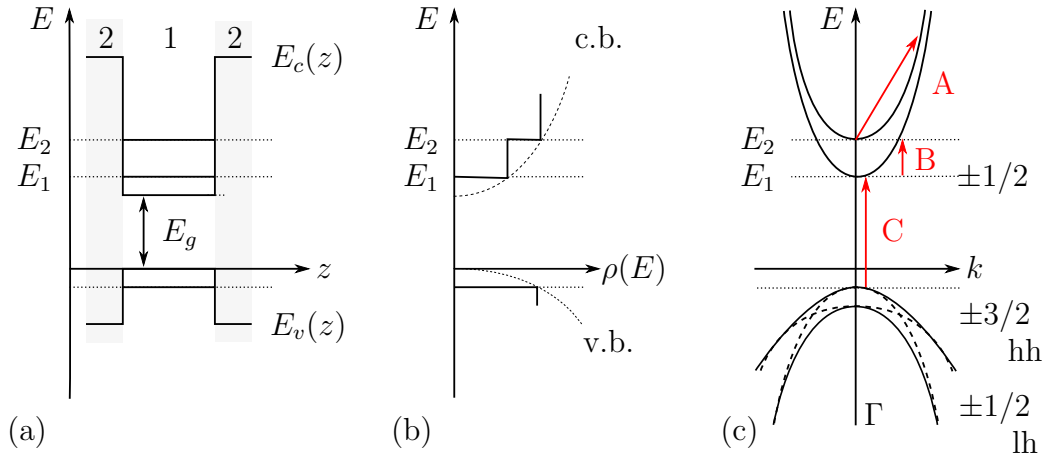


Figure 2.1: (a) Conduction (c.b.) and valence band (v.b.) profile in a 2-1-2 heterostructure. The sharp band-gap discontinuity between well (1) and barrier (2) materials forms a quantum well with band gap E_g . The labels E_1 and E_2 indicate the energy of two confined states in the conduction band. (b) The 2D density of states $\rho(E)$. The dotted line shows the 3D scenario for comparison. (c) Band-structure of the quantum well in momentum space at the Γ -point. Possible optical transitions are intrasubband transitions (A), intersubband transitions (B), and interband transitions (C).

In order to increase the signal strength, multiple periods are grown. In Figure 2.1(a), the conduction and valence band profiles in a heterostructure are shown for the case where electrons and holes are confined in the same material layer. The sharp band-gap discontinuity between the well and barrier materials forms a one-dimensional potential well $V(z)$ where the electrons and holes occupy quantized states. The continuous conduction band is now divided into subbands which effectively changes the band gap of the material, which can be seen in Figure 2.1(b). In quantum wells, the barriers are much thicker than the penetration depth of the wave function into the barriers. In contrast, superlattices are systems with consecutive wells and thin barriers where the wavefunctions of different wells interact and form so-called minibands.

According to Bloch's theorem, the total wave function $\psi(\mathbf{r})$ of an electron in a crystal can be expressed as the product of a lattice-periodic Bloch function $u(\mathbf{r})$ and an envelope function $f \propto e^{i\mathbf{k}\cdot\mathbf{r}}$, where $\mathbf{r} = (r_x, r_y, r_z)$ and $\mathbf{k} = (k_x, k_y, k_z)$ are the position of the electron and its wave vector, respectively [Bal00]. In case of a quantum well, the total wave function can be written as

$$\psi(\mathbf{r}) = u_{\nu\mathbf{k}}(\mathbf{r}) f_{n\mathbf{k}}(\mathbf{r}) \quad , \quad (2.1)$$

where ν and n are the band index and the subband index, respectively. The envelope function varies slowly over the dimension of the quantum well. The motion in the x, y -

plane is free and the electron wave functions can be described by plane waves. The quantum confined part of the wave function is denoted by $\chi_n(z)$. It can be separated as

$$f_{n\mathbf{k}}(\mathbf{r}) = e^{i\mathbf{k}_\perp \cdot \mathbf{r}_\perp} \chi_n(z) \quad , \quad (2.2)$$

with the in-plane momentum $\mathbf{k}_\perp = (k_x, k_y)$ and the in-plane position $\mathbf{r}_\perp = (r_x, r_y)$ of the electron. These subbands result in a staircase density of states, see Figure 2.1(b). In momentum space, see Figure 2.1(c), carriers occupy parabolic bands which are shifted in energy. The total energy E of the system is the sum of the energy E_n of the n th subband and the kinetic energy $\hbar^2 \mathbf{k}_\perp^2 / 2m_e$ of the electron, where m_e is the effective electron mass and $\hbar = h/2\pi$ denotes the reduced Planck constant, i.e.,

$$E = E_n + \frac{\hbar^2 \mathbf{k}_\perp^2}{2m_e} \quad . \quad (2.3)$$

The band bending for holes differs from that of the electrons due to their huge effective mass. Because of the spin-orbit interaction and the interaction with the lattice, the degenerated states of the valence band intermix and split at the Γ -point. The resulting heavy hole (hh) and light hole (lh) bands are sketched in Figure 2.1(c). Through the band structure of the semiconductor, the conduction band minimum is s -like with orbital angular momentum $L = 0$ and the valence band maximum is p -like with $L = 1$. Together with the spin $S = 1/2$, the radiative recombination across the band gap is characterized by a change of the total angular momentum $J = S + L$. In Figure 2.1(c), the states are labeled with the z -component of the total angular momentum $J_z = m_j \hbar$, where $-j \leq m_j \leq j$.

2.2 Optical properties

The red arrows in Figure 2.1(c) indicate possible optical absorption processes in a quantum well. In the case of intrasubband transitions (denoted by A), the carriers are excited within the same subband that requires a momentum change. Details on the free-carrier absorption process are given below. Intersubband transition (B) means that the carriers are excited between subbands of the same band. In interband transitions (C), the carriers are excited between subbands of the valence band to subbands in the conduction band. In the case of a direct band gap material, such as GaAs, these absorption processes occur without changing the momentum, i.e., vertical in k -space.

Free-carrier absorption

Free-carrier absorption is an intraband process, where freely moving carriers are excited to a higher energy state within the same band. The energy increases through the absorption of a photon, while the required momentum change is assisted by phonon scattering. For free-carrier absorption, the number of carriers does not increase but the conductivity changes because of a change in mobility. The process can be described in terms of the Drude model that is based on the classical equations of motion of an electron in an oscillating electric field. The complex conductivity $\tilde{\sigma}(\omega)$ in the Drude expression for free carriers yields

$$\tilde{\sigma}(\omega) = \frac{ne^2\tau}{m_e} \frac{1}{1 - i\omega\tau} \quad , \quad (2.4)$$

where n_e is the electron density, m_e is the effective electron mass, and τ the scattering time [Bal00]. The real part $\text{Re } \tilde{\sigma}(\omega) = \sigma_1$ of the Drude conductivity is

$$\sigma_1(\omega) = \sigma_0 \frac{1}{1 + (\omega\tau)^2} \quad , \quad (2.5)$$

where $\sigma_0 = ne^2\tau/m_e$ is the Drude direct-current conductivity for $\omega = 0$. The absorption coefficient $\alpha(\omega)$ satisfies the equation $I(z) = I_0 e^{-\alpha(\omega)z}$, where $I(z)$ is the light intensity after travelling a distance z in a crystal as compared with the incident intensity I_0 . Generally, it can be expressed as

$$\alpha(\omega) = \frac{2\omega n_2(\omega)}{c} = \frac{\omega \varepsilon_2(\omega)}{c n_1(\omega)} \quad , \quad (2.6)$$

[Bal00], where $n_2(\omega)$ is the imaginary part of the refractive index $\tilde{n}(\omega) = n_1(\omega) + in_2(\omega)$. Using the relation for the complex dielectric function $\tilde{\varepsilon}(\omega) = \varepsilon_1(\omega) + i\varepsilon_2(\omega)$, given by

$$\tilde{\varepsilon}(\omega) = i \frac{\tilde{\sigma}(\omega)}{\varepsilon_0 \omega} \quad (2.7)$$

[Bal00], the electron plasma frequency ω_P is defined as $\varepsilon_1(\omega_P) = 0$. For semiconductors, the typical range of interest is the high-frequency region, $\omega\tau \gg 1$, corresponding to the infrared and ultraviolet regimes, where the relation $\omega \gg \omega_P$ is generally satisfied. In these cases, the absorption coefficient $\alpha(\omega)$ for free-carrier absorption in semiconductors is proportional to the real part of the Drude conductivity given in Equation (2.5),

$$\alpha(\omega) \propto \text{Re } \tilde{\sigma}(\omega) \propto \omega^{-2} \quad , \quad (2.8)$$

and increases strongly for long wavelengths.

Optical selection rules

In case of intersubband (B) and interband transitions (C), the photon absorption induces a transition from an occupied state to an unoccupied state of another band or subband. These processes require a quantum mechanical description. The optical selection rules of intersubband and interband transitions are derived in detail in [Bas88, Hel00, Bal00]. Following the ideas explained in these references, the transition rate W_{if} for an optical transition between initial E_i and final state E_f induced by the time-dependent perturbation H' can be calculated using Fermi's golden rule,

$$W_{if} = \frac{2\pi}{\hbar} |\langle i | H' | f \rangle|^2 \delta(E_f - E_i - \hbar\omega) \quad , \quad (2.9)$$

where $\delta(E_f - E_i - \hbar\omega)$ is the energy conservation term. The canonical momentum $\mathbf{p} = -i\hbar\nabla$ of a particle is changed by an electromagnetic field to $\mathbf{p} - q\mathbf{A}$, where q is the charge and \mathbf{A} the vector potential. For the case of an electron with charge $-e$ and effective mass m_e moving in a potential $V_e(\mathbf{r})$, the Hamiltonian H is given by

$$H = \frac{1}{2m_e} (\mathbf{p} + e\mathbf{A})^2 + V_e(\mathbf{r}) \quad (2.10)$$

$$= H_0 + H' \quad , \quad (2.11)$$

$$\text{where} \quad H' = \frac{e}{2m_e} (\mathbf{p} \cdot \mathbf{A} + \mathbf{A} \cdot \mathbf{p}) + \frac{e^2 \mathbf{A}^2}{2m_e} \quad (2.12)$$

is the light-matter interaction Hamiltonian. The second-order term is neglected as \mathbf{A}^2 can be shown to be small at low intensities. Using the Coulomb gauge, $\nabla \cdot \mathbf{A} = 0$, allows \mathbf{A} to commute with \mathbf{p} , and simplifies Equation (2.12) to

$$H' = \frac{e}{m_e} \mathbf{p} \cdot \mathbf{A} \quad . \quad (2.13)$$

In the dipole approximation, $\mathbf{A}(\mathbf{r}, t) \simeq \mathbf{A}(t)$, the vector potential $\mathbf{A}(t) = \mathbf{e} A_0 \sin \omega t$ varies like the electric field \mathbf{E} and the magnetic field \mathbf{B} of the light wave, where $\mathbf{e} = (e_x, e_y, e_z)$ is the polarization of the light field. The problem given in Equation (2.9) reduces to $|\langle i | \mathbf{e} \cdot \mathbf{p} | f \rangle|^2$ and can be rewritten as the sum of two terms [Bas88],

$$|\langle i | \mathbf{e} \cdot \mathbf{p} | f \rangle|^2 = \langle u_\nu | \mathbf{e} \cdot \mathbf{p} | u_{\nu'} \rangle \langle f_n | f_{n'} \rangle + \langle u_\nu | u_{\nu'} \rangle \langle f_n | \mathbf{e} \cdot \mathbf{p} | f_{n'} \rangle \quad . \quad (2.14)$$

The momentum matrix element $\langle u_\nu | \mathbf{e} \cdot \mathbf{p} | u_{\nu'} \rangle$ describes the interband transition between valence and conduction band, where the $\langle f_{n'} | f_n \rangle$ defines the interband selection rules. In symmetric quantum wells, the interband selection rules between conduction and valence

band are determined by

$$\Delta n = 0, \pm 2, \pm 4, \dots \quad , \quad (2.15)$$

where transitions between states with equal subband index n are most probable [Pel12].

The second term of Equation (2.14), $\langle f_n | \mathbf{e} \cdot \mathbf{p} | f_{n'} \rangle$, representing the intersubband transitions exists only within the same band ν because of the orthogonality term $\langle u_\nu | u_{\nu'} \rangle = \delta_{\nu\nu'}$. Further evaluation of the dipole matrix element of the envelope function $f_{n\mathbf{k}_\perp}$ given by Equation (2.2) leads to

$$\langle f_{n\mathbf{k}_\perp} | \mathbf{e} \cdot \mathbf{p} | f_{n'\mathbf{k}'_\perp} \rangle = (e_x \hbar k_x + e_y \hbar k_y) \delta_{nn'} \delta_{\mathbf{k}_\perp \mathbf{k}'_\perp} + e_z \langle \chi_n | p_z | \chi_{n'} \rangle \delta_{\mathbf{k}_\perp \mathbf{k}'_\perp} \quad . \quad (2.16)$$

The first term accounts for intrasubband transitions within the same subband n under the restriction $\mathbf{k}_\perp = \mathbf{k}'_\perp$, where the initial and final state are the same. The second term implies that the optical pulse for intersubband transition has to be polarized in the quantum well plane z for an efficient coupling to the free motion of the carriers, where only vertical optical transitions in momentum space are possible.

2.3 Excitons

The properties of electron-hole plasma are closely related to the existence of an excitonic population. Under certain conditions, excitons can form from free electrons and holes after optical excitation across the band gap . An exciton is a quasi-particle with bosonic characteristics comparable to a hydrogen atom. Before deriving the properties of an exciton, the basic equations for a hydrogen atom are recalled. In a second step, the quantities are rescaled according to the different ratio of the electron and hole effective masses of the exciton and the permittivity $\varepsilon = \varepsilon_r \varepsilon_0$ of the medium with the vacuum permittivity $\varepsilon_0 \approx 8.85 \times 10^{-12} \text{ C}^2 \text{ N}^{-1} \text{ m}^{-2}$).

The hydrogen atom consists of a proton and a light electron that circulates around that heavy nucleus. The nucleus can be assumed to be at rest, which reduces the problem to the electron's motion in a spherically symmetric potential

$$V(r) = -\frac{1}{4\pi\varepsilon_0} \frac{e^2}{r} \quad , \quad (2.17)$$

where r is the distance to the nucleus. For symmetry reasons, the Schrödinger equation for the hydrogen atom,

$$\hat{H}\psi = E\psi \quad , \quad (2.18)$$

$$\left(-\frac{\hbar^2}{2m_0}\nabla^2 + V(r)\right)\psi = E\psi \quad , \quad (2.19)$$

is solved by searching solutions of the type $\psi(r, \theta, \phi) = R(r)\Theta(\theta)\Phi(\phi)$ in spherical coordinates r, θ, ϕ . The solutions to the separated Equations (2.19) have to obey the constraints on a wavefunction concerning continuity and normalization and can be found in any quantum mechanics textbook. The final energy eigenfunctions of the hydrogen atom are of the general form $\psi_{n\ell m} = R_{n\ell}(r)Y_\ell^m(\theta, \phi)$ with the radial wave function $R_{n\ell}(r)$ and the spherical harmonics $Y_\ell^m(\theta, \phi)$. The three integer quantum numbers n, ℓ, m satisfy

$$n > \ell \geq |m| \quad . \quad (2.20)$$

Since the lowest possible value of the principal quantum number n is one, the ground state of the lowest energy state E_1 is the eigenfunction ψ_{100} . Typically, the states of the neutral excitons are labeled in three-dimensional hydrogenic notation. While the principal quantum number n denotes the energy level, the orbital angular momentum ℓ indicates the subshell. It can reach the values $\ell = 0, 1, \dots, n - 1$, where $\ell = 0$ is the s orbital, $\ell = 1$ is the p orbital, and $\ell = 2$ is the d orbital. The magnetic quantum number m indicates the projection of the orbital angular momentum L in z -direction, $L_z = m\hbar$, where $-\ell \leq m \leq \ell$.

The allowed orbital radius r_n at any n is

$$r_n = 4\pi\epsilon_0 \frac{n^2 \hbar^2}{m_0 e^2} = n^2 a_B \quad , \quad (2.21)$$

where m_0 is the rest mass of the electron and the smallest possible electron orbit a_B is $5.3 \times 10^{-11} \text{ m} = 0.53 \text{ \AA}$, the so called Bohr radius. The energy eigenvalues E_n are given by

$$E_n = -\frac{m_0 e^4}{8 \epsilon_0^2 h^2} \frac{1}{n^2} = -\frac{Ry}{n^2} \quad . \quad (2.22)$$

and only depend on the principal quantum number n . The effective Rydberg energy $Ry = 13.6 \text{ eV}$ is the ground state energy E_1 of a hydrogen atom as defined by

$$Ry = \frac{m_0 e^4}{8 \epsilon_0^2 h^2} \quad . \quad (2.23)$$

In contrast to the hydrogen atom, the exciton consists of an electron and a hole with comparable effective electron and hole masses m_e and m_h . In order to calculate the exciton radius and the energy, the heavy proton is replaced by the hole. The reduced mass of an exciton μ_X is

$$\mu_X = \frac{m_e m_h}{m_e + m_h} \quad , \quad (2.24)$$

which results in a larger orbital radius compared to the hydrogen atom. The permittivity $\varepsilon = \varepsilon_r \varepsilon_0$ of the background material reduces the attractive electrostatic force between the constituents and further increases the exciton radius. With the substitutions $m_0 \rightarrow \mu_X$ and $\varepsilon_0 \rightarrow \varepsilon_0 \varepsilon_r$, the allowed orbital radius r_n given by Equation (2.21) changes to the radius of a free exciton $a_{X(n)}$ for any n ,

$$a_{X(n)} = \frac{m_0 \varepsilon_r}{\mu_X} n^2 a_B \quad . \quad (2.25)$$

The energy given by Equation (2.22) changes to the exciton energy levels $E_{X(n)}$

$$E_{X(n)} = -\frac{\mu_X}{m_0 \varepsilon_r^2} \frac{Ry}{n^2} \quad , \quad (2.26)$$

where the exciton binding energy $E_{X(1)} = E_X$ is

$$E_X = -\frac{\mu_X}{m_0 \varepsilon_r^2} Ry \quad . \quad (2.27)$$

The Coulomb interaction of an exciton in a semiconductor is up to three orders of magnitude less than that of a free-space hydrogen atom, which strongly influences the exciton stability. As further aspect is that hydrogen atoms are stable, while excitons have characteristic lifetimes in the order of nanoseconds, see e.g., [Suz09]. Thus, the analysis of excitonic properties and relaxation dynamics is difficult due to the exciton dissociation and recombination processes.

Excitons can be classified into two groups depending on the permittivity ε of the background material shielding the attractive electrostatic force. Schematic drawings of a hydrogen atom and possible electron-hole configurations in a perfect lattice are shown in Figure 2.2. Table 2.1 lists typical values for comparison. The large-radius Wannier excitons (b) are typical in semiconductors and have a Bohr radius a_X of about 100 Å that is larger than some lattice constants. Frenkel excitons (c) with a high binding energy of 1 eV and a smaller Bohr radius of 10 Å are typical in organic materials.

In the following, the characteristics of Wannier excitons that move freely in a perfect lattice is considered. The excitons occupy confined states below the band edge E_g within the energy gap. Together with Equation (2.26), the total energy of the exciton is given

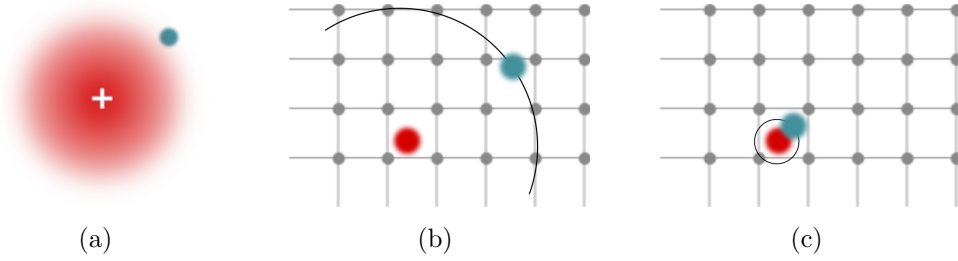


Figure 2.2: (a) Hydrogen atom in free space (set to scale). A light electron (blue) circulates around a heavy proton (red). (b)–(c) Schematic drawing of excitons in a perfect lattice, where the electron circulates around the hole and vice versa. (b) Wannier exciton and (c) Frenkel exciton.

	(a) Hydrogen atom	(b) Wannier exciton	(c) Frenkel exciton
Ry	13.6 eV	5 meV	1 eV
radius	0.5 Å	100 Å	10 Å
ε_r	1	12.9 (GaAs)	1 (Bchl)

Table 2.1: Comparison of hydrogen atom, Wannier exciton in the typical semiconductor material GaAs [Rum96], and Frenkel exciton in the organic material bacteriochlorophyll (Bchl) [Pse03, Sch06b].

by

$$E_{(n)}(k) = E_g + E_{X(n)} + \frac{\hbar^2 k^2}{2(m_e + m_h)} . \quad (2.28)$$

Figure 2.3(a) shows the corresponding in-plane energy dispersion of the $1s$, the $2s$, and the $2p$ excitons lying below the continuum of unbound electron-hole pairs. From the absorption spectrum, a strong peak is visible at the $1s$ exciton absorption line. Lines that arise from excited excitonic states ($3s$, $4s$, ...) merge energetically with the free carrier emission at the band edge E_g , see Figure 2.3(b).

In quantum wells with layer thicknesses smaller than the exciton radius, the wave functions are modified and the exciton binding energy is larger compared to that of bulk material. The two-dimensional Rydberg energy is

$$Ry_{2D} = 4 Ry \quad (2.29)$$

[Bal00], which results in a four times larger separation of the $1s$ peak from the interband absorption continuum, see Figure 2.3(b). Furthermore, due to the increased binding energy and the reduced Bohr radius, excitons dominate the optical properties of GaAs quantum wells even at room temperature [Bal00].

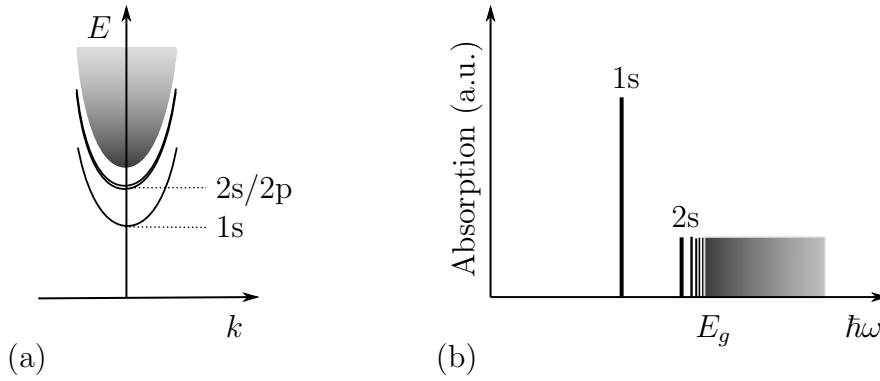


Figure 2.3: (a) The in-plane energy dispersion of the 1s and 2s/2p excitons lying below the continuum of unbound electron-hole pairs (gray area). (b) Near-infrared absorption spectrum at the fundamental band edge. The 1s exciton absorption line is about 10 meV below E_g . Higher excitonic transitions merge with the interband absorption continuum. This figure is adapted from [Koc06].

2.4 Exciton Mott transition

In condensed matter, the Mott transition marks the phase change of the material's electrical conductivity from insulating to metallic. One important example is the breakup of excitons as a function of induced pair density N . The characteristics of the system changes from an isolating pure exciton population to a conducting electron-hole plasma [Kai03, Kap05, Amo06, Ste08]. The different phases of an exciton Mott transition are shown in Figure 2.4. At the critical Mott density N_M , the screening potential of the free carriers is strong enough to merge many of the bound electron-hole pairs [Pel12]. Due to ongoing exciton formation and dissociation processes, there is a transient change of the ratio between the exciton and electron-hole populations. The actual exciton formation rate is hard to detect. Under the aspect of carrier density, the interaction potential of the

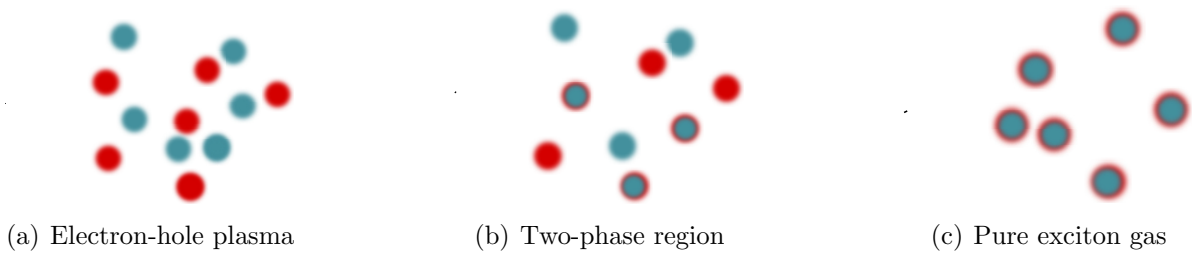


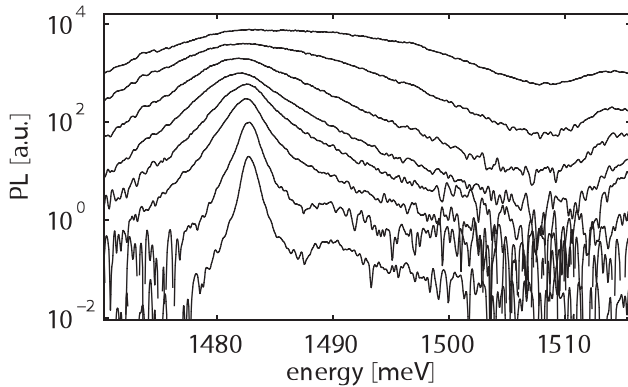
Figure 2.4: Different phases of an electron-hole system. This figure is adapted from [Kai03].

exciton given by Equation (2.17) can be expressed as

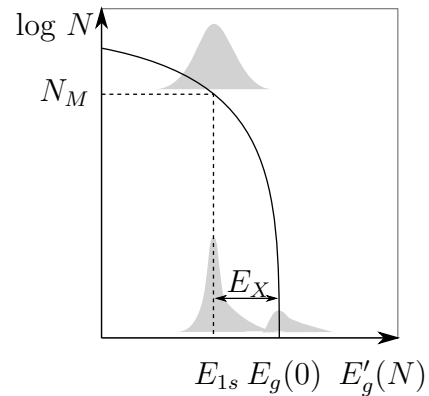
$$E_{\text{pot}}(r) = -\frac{1}{4\pi\epsilon} \frac{e^2}{r} e^{-k_s r} \quad , \quad (2.30)$$

where $k_s > 0$ is the screening factor. The screening length $\lambda_s(N) = k_s^{-1}$ decreases with the number of free electron-hole pairs. Above a critical density, where the average distance between the excitons is equal the exciton radius, the electron-hole interaction is screened and bound pairs easily break, see e.g., [Hen07].

The set of PL spectra for a single 8 nm wide $\text{In}_{0.05}\text{Ga}_{0.95}\text{As}$ quantum well sample in Figure 2.5(a) exemplarily shows the gradual change of the spectral shape for increasing excitation powers measured by [Kap05]. For lowest intensities, a sharp peak at 1482 meV marks the excitonic transition. At about 1490 meV, the free carrier emission is visible with a sharp rise on the low-energy side. The exciton binding energy E_X can be read from the distance between the exciton peak and the band-edge emission. While for a low excitation density, the spectrum shows excitonic characteristics, broad peaks indicate the transition to pure plasma for higher densities. Apparently, the spectral shape changes gradually with the Mott transition. Surprisingly, the maximum emission peak does not shift in energy, i.e., even a pure electron-hole plasma luminescences at the free-exciton energy E_{1s} . With increasing electron-hole pair density beyond the Mott density, $N > N_M$, the band gap reduces below the given value $E_g(0)$ in the one-electron approximation. Figure 2.5(b) schematically shows the underlying band-gap renormalization $E'_g(N)$ due to many-body effects [Kap05, Pel12, Man12]. The Mott density N_M marks the intersection of the gap energy $E'_g(N)$ and the ground exciton level E_{1s} [Pel12].



(a) Gradual change of PL spectra with increasing excitation powers from lower ($1.6 \times 10^9 \text{ cm}^{-2}$) to upper curve ($6.2 \times 10^{11} \text{ cm}^{-2}$). The Figure is taken from [Kap05]. Copyright (2005) by The American Physical Society.



(b) The renormalized band gap E'_g as a function of electron-hole pair density N . The gray areas depict the luminescence spectra; N_M is the Mott density. The Figure is adapted from [Pel12].

Figure 2.5: Visualization of the gradual Mott transition with increasing pair density N .

From the PL emission energy, it cannot be concluded whether exciton or free carrier states are populated. However, at low temperatures and for low and intermediate densities, the 1s PL signal is dominated by excitonic recombination [Koc06, Hen07] even though reported bright exciton fractions are less than 0.04% compared to the total amount of

electrons and holes [Cha04]. Both, excitons and free carriers influence the PL line shape. Even at room temperature, excitonic effects have to be considered to explain the PL line shape [Chr90].

2.5 Quantum-well-confined magnetoexcitons

It was shown in the previous section that the exciton binding energy strongly increases in quantum wells with increasing electron-hole confinement, see Equation (2.29). In the following, quantum-well-confined magnetoexcitons are studied under the influence of a magnetic field that is directed perpendicular to the well layer. The magnetic field acts as an external perturbation and induces modifications on the excitonic properties and the energy levels of the system. Through the Lorentz force, electrons and holes localize in the quantum well layer forming Landau levels. The additional confinement reduces the degrees of freedom by two. This results in a quasi-zero dimensional system with discrete energy states.

The Hamiltonian of bound electrons and holes in a quantum well with an externally applied magnetic field can be written as the sum of the magnetic field modified kinetic energies H_i , the confining quantum well potentials $V_i(\mathbf{r}_i)$, the Coulomb attraction H_{e-h} , and the Zeeman perturbation $-\boldsymbol{\mu} \cdot \mathbf{B}$,

$$H = H_e + V_e(\mathbf{r}_e) + H_h + V_h(\mathbf{r}_h) + H_{e-h} - \boldsymbol{\mu} \cdot \mathbf{B} \quad , \quad (2.31)$$

where $-\boldsymbol{\mu}$ is the magnetic moment. The intertwining of Zeeman and Coulomb interaction [Koh54, Lut56] is not considered throughout the present dissertation. For recent discussion of this topic the reader is referred, e.g., to [Obe12]. The external magnetic field induces an additional energy to the (n, ℓ, m) state. For a weak magnetic field in z -direction, the Zeeman term can be expressed as $\sigma_z g \mu_B B_z$, where σ_z is the z -component of the spin quantum number ($\sigma_z = \pm 1/2$), g is the Landé g -factor for an electron, and $\mu_B = e\hbar/(2m_e)$ is the Bohr magneton.

The electron, hole, and the Coulomb attraction parts of the Hamiltonian are

$$H_e = \frac{1}{2m_e} (\mathbf{p}_e + e\mathbf{A})^2 \quad , \quad (2.32)$$

$$H_h = \frac{1}{2m_h} (\mathbf{p}_h - e\mathbf{A})^2 \quad , \quad (2.33)$$

$$H_{e-h} = -\frac{1}{4\pi\epsilon} \frac{e^2}{|\mathbf{r}_e - \mathbf{r}_h|} \quad . \quad (2.34)$$

For a magnetic field applied perpendicular to the wells, $\mathbf{B} = (0, 0, B_z)$, the vector potential \mathbf{A} can be expressed in Landau gauge, $\mathbf{A} = (-yB_z, 0, 0)$, which fulfills the condition $\nabla \times \mathbf{A} = \mathbf{B}$ [Bal00]. In this special case, the electron Hamiltonian given by Equation (2.32) changes to

$$H_e = \frac{1}{2m_e} \left((p_x - e y B_z)^2 + p_y^2 \right) + \frac{p_z^2}{2m_e} . \quad (2.35)$$

With the replacement $p_x \rightarrow \hbar k_x$ and the cyclotron resonance frequency $\omega_c = eB/m_e$, the Hamiltonian has the form of a harmonic oscillator,

$$H_e = \frac{1}{2} m_e \omega_c^2 \left(y - \frac{\hbar k_x}{m_e \omega_c} \right)^2 + \frac{p_y^2}{2m_e} + \frac{p_z^2}{2m_e} , \quad (2.36)$$

where the potential minimum is shifted by $-\hbar k_x/m_e \omega_c$. The Landau levels of a free electron in a quantum well are equidistant one-dimensional magnetic subbands with energy eigenvalues

$$E_{ln\sigma_z} = \hbar \omega_c \left(\ell + \frac{1}{2} \right) + \sigma_z g \mu_B B_z + E_n , \quad (2.37)$$

where $n = 1, 2, 3, \dots$ denote the subbands and $\ell = 0, 1, 2, \dots$ are the Landau levels. The Landau levels of holes are derived analogously.

The externally applied magnetic field has two effects on the energy levels. Firstly, the levels spin-split linearly with magnetic field. Secondly, the energy of both spin-split levels increases which is called diamagnetic shift [Wal98]. For our experiment, the spin splitting is small and can be neglected [Sne92]. For GaAs systems, the diamagnetic shift for quantum wells is typically higher than that for bulk. However, this shift strongly decreases for narrow wells due to the reduced in-plane electron-hole separation [Bug86, Wal98].

In theory, magnetoexcitons according to Equation (2.31) are treated either as electrons and holes with Coulomb interaction or as quasi-particles with hydrogen atom like states. The energy spectrum is strongly influenced by the magnetic field. For strong magnetic fields with

$$\hbar \omega_c \gg Ry ,$$

the Coulomb energy is small compared to the cyclotron energy. The electrons and holes occupy electron-hole Landau levels and the Coulomb interaction acts as a weak perturbation of the quantized cyclotron orbits. In the high field limit, magnetoexcitons act like noninteracting particles [Sta90]. In the weak field regime, that is characterized by

$$\hbar \omega_c \ll Ry ,$$

the magnetic field acts as an external perturbation on the excitonic energy states. The induced diamagnetic shift is small compared to the exciton binding energy, and the level energy increases quadratically with magnetic field [Wal98].

2.6 Photoluminescence

Generally, the term ‘luminescence’ denotes all optical radiation that arises from the transition of an excited system to its ground state. The emitted luminescence is classified depending on the type of the initial excitation, e.g., electroluminescence by electric field and thermoluminescence by heating. Photoluminescence (PL) produces an optical emission spectrum after excitation with photons probing the electronic levels of the structure. PL spectroscopy on undoped semiconductors requires the excitation of electrons into the conduction band. The minimum photon energy of the exciting laser is equal to the band gap. The number of induced carriers depends on material properties and the excitation density, i.e., the number of photons per unit time and area. Under continuous-wave laser excitation, there is a dynamic equilibrium between created and decaying electron-hole pairs whereas short-pulse excitation provides access to the internal carrier dynamics. The spectral features depend on the internal excitonic structure of the sample. While intrinsic PL originates exclusively from carriers in defect-free crystalline material, impurities and lattice defects act as luminescence centres of extrinsic PL. In the latter case, free excitons get localized at impurity atoms and lose their kinetic energy.

Radiative recombination

The recombination process between an excited state and the ground state can occur on radiative and nonradiative channels. In case of a radiative transition, luminescence photons are emitted that carry the excitation energy, while non-radiative transitions occur via phonon emission, excitation of impurities, and excitation of carriers (Auger recombination). The mean lifetimes of the radiative and the non-radiative transitions are denoted as the radiative recombination time τ_r and the non-radiative recombination time τ_{nr} , respectively. The total luminescence decay rate is

$$\frac{1}{\tau} = \frac{1}{\tau_r} + \frac{1}{\tau_{nr}} \quad , \quad (2.38)$$

where τ denotes the luminescence decay time. From this definition it follows that the quantum efficiency of luminescence, i.e., the ratio of the radiative recombination rate $1/\tau_r$

and the total recombination rate $1/\tau$ given by Equation (2.38), can be expressed as

$$\eta = \frac{1/\tau_r}{1/\tau_r + 1/\tau_{nr}} = \frac{\tau}{\tau_r} \leq 1 \quad , \quad (2.39)$$

according to [Pel12]. This simple equation expresses the essential fact that the experimentally derived luminescence decay time does not equal the radiative lifetime. Furthermore, in case of a very low quantum efficiency $\eta \ll 1$, the non-radiative lifetime dominates the luminescence decay, $\tau_{nr} \approx \tau$, as can be directly derived from Equation (2.38).

Possible radiative scenarios after weak excitation are schematically shown in Figure 2.6. These are band-to-band recombination, radiative recombination of a free exciton, a free electron with a neutral acceptor, a free hole with a neutral donor, and a donor-acceptor pair. All the scenarios result in different emission energies and PL decay times τ . In highly excited semiconductors, more PL signatures arise from excitonic molecules and inelastic collisions of free excitons [Pel12].

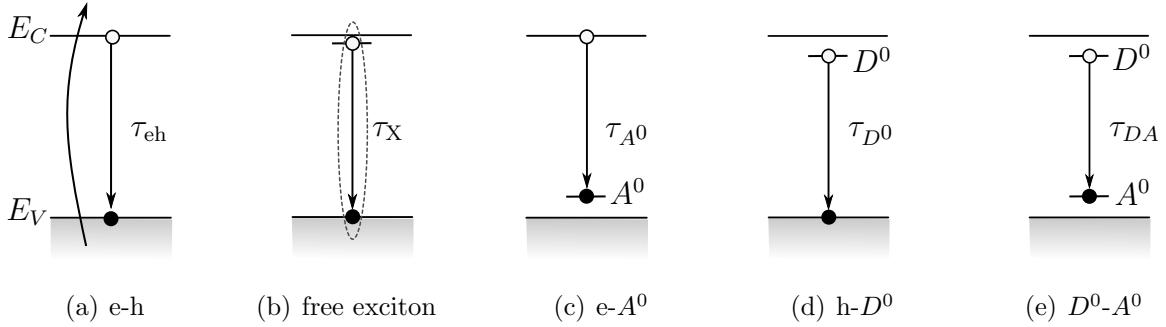


Figure 2.6: Schematics of possible recombination scenarios after optical excitation from the valence band to the conduction band. The time-constants label the radiative recombination channel. (a) band-to-band (e-h) (b) free exciton (X), (c) free electron and a neutral acceptor ($e-A^0$), (d) free hole with a neutral donor ($h-D^0$), (e) donor-acceptor pair (A^0-D^0).

Photoluminescence dynamics

Under laser excitation with pulses shorter than the lifetime of the created carriers, the PL dynamics can be studied until the system reaches equilibrium or experiences subsequent excitation. After non-resonant laser excitation, the induced plasma occupies a large momentum space in the conduction band. The carriers thermalize on a 100 fs time scale [Els91] into a hot Fermi distribution with a carrier temperature T_C higher than the lattice temperature T_L . Excitons form with a finite center of mass momentum $k \neq 0$ which do not participate to the PL signal intensity. The subsequent energy and momentum relaxation of the hot carrier distribution towards the zero momentum

state is mediated by phonon emission [Leo88, Tse01]. The lattice interaction via optical phonon relaxation occurs on subpicosecond time scales, while the acoustic phonon emission takes nanoseconds [Kas84, Lob89] and dominates the relaxation process. Reported LO phonon emission rates in GaAs/AlGaAs quantum wells are in the order of $5 \times 10^{12} s^{-1}$, see e.g., [Lee95]. The subsequent recombination process results in a depopulation of the zero momentum state and the decay of the PL signal. However, the origin of the excitonic luminescence in quantum wells is determined by the coexistence of excitons and electron-hole pairs and has been the topic of numerous discussions. From early time-resolved PL data, the rise time of the $1s$ PL signal was associated with the exciton formation time [Kus89, Dam90, Ecc91, Blo93, Kum96], and the PL decay time corresponds to the exciton relaxation [Fel87, Dev91]. In various articles, a PL signal at the $1s$ energy has been taken as an indication of an excitonic population [Kus89, Dam90, Blo93, Kum96], whereas [Gal05] proposed excitonic PL emission without the existence of an excitonic population at $k = 0$. In a recent review article on semiconductor excitons [Koc06], the authors expressed their fundamental findings as follows:

[...] in reality, the electron-hole pairs constitute a strongly interacting many-body system. The emission of a photon should therefore not be viewed as the recombination of any given electron-hole pair in whatever bound or unbound state, but rather as a transition from a many-particle configuration with N interacting pairs to one with $N-1$ pairs. [...]

In summary, the PL dynamics results from a distribution of electron-hole pairs that occupy bright and dark states, and it not directly unveils the exciton formation, relaxation, and recombination processes [Kai03, Kai09].

3 Spectroscopic tools and sample characterization

In this chapter, the experimental details including the two different pulsed infrared laser sources, the detection unit, and the experimental setup are described for the two-color time-resolved PL measurements without and with externally applied magnetic field. Particularly, the synchronization of the free-electron laser with the table-top system in the lab was realized. The optical beam paths have been installed such that the different laser pulses are brought to spatial and temporal overlap at the sample position. Furthermore, details on the three high quality GaAs quantum well samples are presented. An overview is given on the basic parameters of the samples and the PL emission spectra.

Parts of this chapter have been published previously [Bha11].

3.1 Titanium-Sapphire laser

The near-infrared pulse source is a tunable Titanium:Sapphire (Ti:Sapph) laser (Spectra Physics: Tsunami 3960) providing short pulses over a broad range of near-infrared wavelengths. For decades, this laser type has been an essential tool for many time-resolved studies featuring broad tunability and high stability. The active medium of this solid-state laser is a sapphire (Al_2O_3) crystal doped with titanium ions and pumped at 532 nm by a Nd:YVO₄ continuous-wave laser (Spectra Physics: Millennia Pro). The working principle is based on soft aperture Kerr-lens mode locking in the gain medium. In this regime, mode-locking is promoted by the stronger overlap of the pulsed high intensity radiation with the pump radiation induced by self-focusing. Since the overlap of the continuous-wave radiation at lower intensity is weaker, stable mode locking is achieved. For our experiments, the Ti:Sapph laser runs in picosecond mode delivering 3 ps to 4 ps long optical pulses with a repetition rate of 78 MHz. With the chosen optics, the system is tunable between 690 nm and 1100 nm with an average output power of 2 W at 750 nm. The laser pulses can be synchronized to other lasers with the Lok-to-Clock[®] electronics (Spectra Physics: Model 3930) that actively stabilizes the cavity length.

3.2 Free-electron laser

Free-electron lasers are powerful radiation sources tunable over wide frequency ranges. Relativistic electrons in a magnetic field represent the active medium in a simple cavity of two mirrors. The electrons are linearly accelerated to relativistic velocities and injected into the cavity. A periodic set of alternating static magnets (undulator) placed around the cavity bends the electrons' path. Due to this defined oscillatory motion in a periodic field, the relativistic electrons spontaneously emit light. In turn, the reflected light field interacts within the resonator with newly injected electron bunches, leading to stimulated emission, optical gain and amplification. After passing the undulator, the electrons are dumped behind the cavity. The emitted wavelength can be tuned by the electron energy and the variable gap between the magnets which influences the curvature of the electron path. The resonator length defines the repetition rate of the emitted optical pulses. The emitted wavelength λ_0 ,

$$\lambda_0 = \frac{\lambda_u}{2\gamma^2} \left(1 + \frac{K^2}{2} \right) \quad (3.1)$$

[Zvy09], is controlled by the magnetic field amplitude B , the undulator period λ_u , and the relativistic energy of the electrons $\gamma m_0 c^2$, where

$$\gamma = \frac{1}{\sqrt{1 - (\frac{v}{c})^2}} \quad \text{and} \quad K = \frac{\lambda_u e B}{2\pi m_0 c} \quad . \quad (3.2)$$

FELBE is an acronym for the free-electron laser (FEL) at the Electron Linear accelerator with high Brilliance and Low Emittance (ELBE) located at the Helmholtz-Zentrum Dresden-Rossendorf. The facility FELBE consists of two independent cavities each with a length of 11.53 m. While the undulator U27 works for the shorter wavelengths from 4 μm to 25 μm , the second undulator U100 is optimized for the wavelength range between 20 μm and 250 μm . The system runs in 13 MHz mode providing short pulses between 1 ps to 25 ps length and up to 20 W average power depending on the set wavelength.

Together with the unique optical characteristics, the system is highly suitable for two-color experiments on semiconductor systems as it covers the far-infrared and mid-infrared spectral region where the internal transitions of the studied quantum well systems are expected. In particular, the continuous pulsing mode that is enabled by the superconducting accelerator technology of ELBE, is unique in Europe. This mode is essential for the two-color experiments described in this thesis. The free-electron laser beamline has several outlets providing direct access to each of the optical labs. For more details of FELBE the reader is referred to [Wag09a, Zvy09].

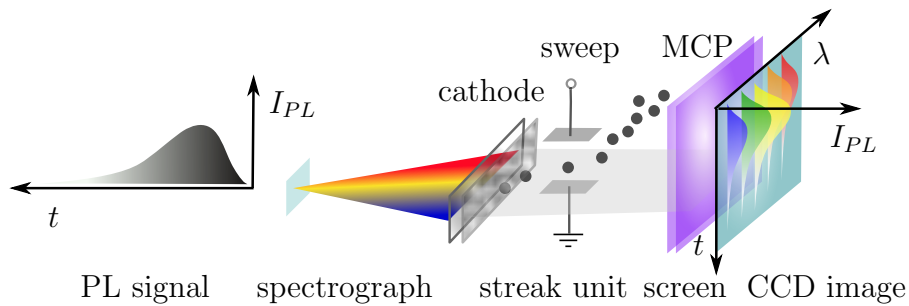


Figure 3.1: Operation principle of a streak camera. After passing a spectrograph, the dispersed light enters a cathode-ray tube. This evacuated streak unit is equipped with a sweep electrode deflecting the accelerated photoelectrons onto the micro-channel plate (MCP). The induced light emission at the phosphor screen is imaged by a CCD camera.

3.3 Streak camera

Streak cameras are sensitive detectors that convert the temporal and the spectral information of a light pulse into spatial coordinates on a phosphorescence screen. The working principle of a streak camera is a combination of a cathode-ray tube and an oscilloscope [Pel12]. It is schematically shown in Figure 3.1. The light pulses pass through the entrance slit of the device and hit a photocathode. The photoelectric effect induces the emission of photoelectrons which are accelerated between two oppositely charged plates within a vacuum tube. A sweep field between two electrodes is arranged perpendicular to the flight direction of the electrons. The applied voltage varies in a way such that the electrons which come first are deflected most strongly while the later ones get less deflected onto the micro-channel plate (MCP). One sweep matches the diameter of the phosphor screen where the electrons generate light. The induced light emission is imaged by a charged-coupled device (CCD) camera. The colors of the computer processed streak image map the time-resolved intensity profile of the signal.

We use a streak camera (Hamamatsu: C5680-27) connected to a 0.25 m Czerny-Turner type grating spectrometer (Bruker: Chromex 250is/is) where the incoming polychromatic light passes the entrance slit and is collimated by a curved mirror. A grating diffracts the light under different angles depending on the wavelength. The dispersed light is collected by a second mirror and refocused into the exit slit. The spectrometer is equipped with three different gratings with 300 lines/mm, 600 lines/mm, and 1200 lines/mm and with a nominal resolution of 1.8 nm, 0.6 nm and 0.15 nm, respectively. Both systems and the high resolution CCD camera (Hamamatsu: ORCA-ER C4742-95) are electronically controlled via HPD-TA 8.3.0 software. The streak camera can be operated in time-integrated or time-resolved mode with a maximum time window of 2.1 ns and about 4 ps time resolution. Using a streak camera, we gain spectral information from 300 nm to 1600 nm limited by

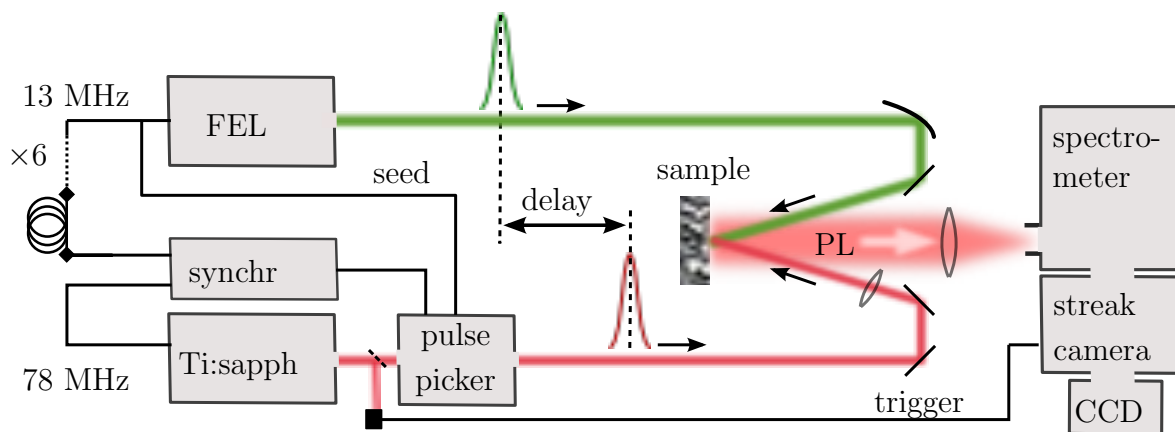


Figure 3.2: Scheme of the experimental setup for two-color time-resolved photoluminescence measurements. Red and green lines indicate the near-infrared and the THz beam paths, respectively. Black lines are cable connections for synchronization. The temporal delay between the near-infrared laser pulse and the THz pulse is adjusted with a variable coaxial line.

the photocathode sensitivity and the spectrometer setting. The studied energy range depends on the set grating of the spectrometer. The streak camera software is used for data acquisition and analysis. With intensity profiles along the horizontal and vertical axes of the streak images, measured PL spectra are spectrally and temporally characterized.

3.4 Experimental setup and pulse synchronization

The basic experimental setup for time-resolved PL measurements consists of the Ti:sapph laser, a beam path with silver mirrors, focusing lenses, and a computer controlled streak camera as the detection unit. The PL is free-space guided and focused by a lens into the entrance slit of the spectrometer. For two-color experiments, a second beam path with gold coated mirrors was installed guiding the free-electron laser pulses onto the sample. The free-electron laser beam is focused by means of a parabolic mirror. Figure 3.2 schematically shows the experimental setup for two-color time-resolved PL measurements including the two pulse sources and beam paths, the synchronization unit, and the detection part. Behind the Ti:sapph laser, two beam splitters are installed so that a fraction of the near-infrared beam is reflected into a spectrometer (APE Berlin: WaveScan) and an autocorrelator (APE Berlin: PulseScope) for monitoring the actual wavelength and the pulse widths, respectively.

The focus diameters at the sample position of the near-infrared and the THz beam are $30\ \mu\text{m}$ and $350\ \mu\text{m}$, respectively. The laser fluence Φ is a measure used to describe the energy that is delivered per unit area. In this thesis, the fluence in units of J cm^{-2} is

calculated from the average laser power divided by the focal spot area and by the pulse repetition rate.

The pulse synchronization is performed in two steps as the pulse repetition rates need to match. First, the Ti:Sapph laser repetition rate is reduced using an acoustic optically pulse picker (APE Berlin: PulseSelect) which is externally triggered by the electronic signal of the free-electron laser (FEL clock). While passing a crystal, the beam diffracts from an ultrasonic grating. Our experimental setup requires a division ratio of $f_{\text{NIR}}/6$. For the operation with this ratio, the average power output of the pulse picker is about 2% of the power input featuring a very good contrast ratio. In our experiment, the near-infrared first order beam (78 MHz) gets reduced to the 13 MHz repetition rate of the free-electron laser. Secondly, the near-infrared pulses from the Ti:Sapph laser get phase-locked to the FEL clock. To this end, the 13 MHz FEL clock signal is upconverted electronically to 78 MHz and employed as a master clock signal to the synchronization unit (Spectra Physics: Model 3930). The time delay between the two pulses is fine tuned using a coaxial line of variable length. The free-electron laser pulses are temporally monitored using a non-commercial broadband superlattice detector [Kla01] suitable for wavelengths above 40 μm or using a photoelectromagnetic mercury cadmium telluride (MCT) detector (Vigo System PEM10.6 detector) with working range between 2 μm and 11 μm . For the near-infrared pulses from the Ti:sapph laser, we use a fast silicon photodiode (Thorlabs DET210). The laser profile is detected using a pyroelectric array camera (Ophir Photonics: Spiricon Pyrocam), which is sensitive to near-infrared and THz wavelengths. A pyroelectric crystal converts the absorbed light to heat that creates measurable charges on the surface. During the measurements, the sample is kept at liquid helium temperature (4 K) in a continuous flow cryostat. Diamond windows stand out due to their high transmittance up to far-infrared which meets the requirements of our two-color experiments.

3.5 Magneto-optical system

The magnetoluminescence experiments were performed with the PL setup using a split-pair superconducting magneto-optical system (Oxford SM4000-8). This special cryostat (spectromag) is equipped with a vertical split pair magnet producing a nearly uniform field up to 8 T in horizontal direction. Figure 3.3(a) shows the cylindrical vacuum isolated dewar with connection ports and valves on top and a cuboid shaped cryostat tail unit at the bottom. In total, the spectromag has a height of 1.4 m and a diameter of 0.5 m. It has four z-cut quartz windows, one on each side. The dewar is shielded by an outer evacuated isolation chamber, a nitrogen chamber, and an inner helium chamber with a volume of 41 liter, 24 liter, and 20 liter, respectively. In the 0 T modus, the helium

and nitrogen consumption is as low as 0.2 liter and 0.5 liter per hour. For operation, the superconducting coils need to be fully covered by liquid helium to prevent them from sudden heating. Otherwise, the coils might be driven to normal conduction and the magnet can be damaged by high voltage, high temperature, and high forces. The

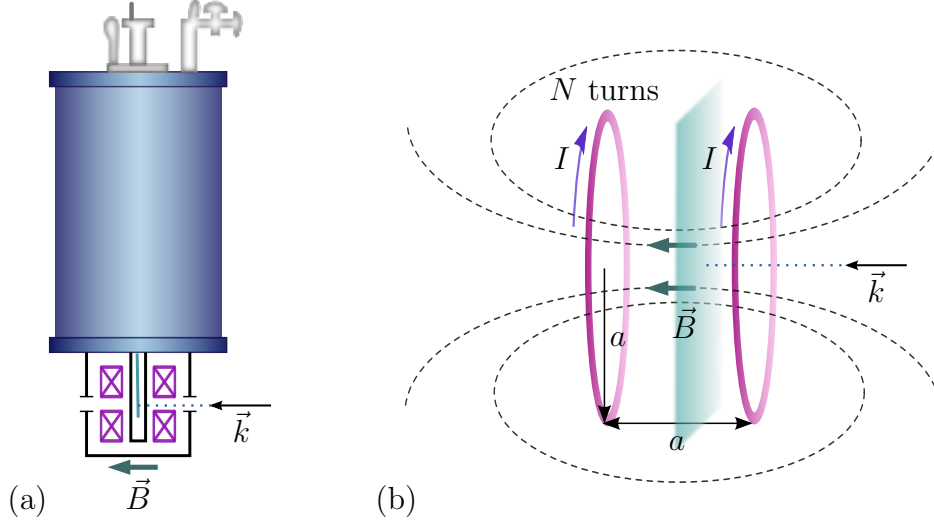


Figure 3.3: (a) Scheme of the magneto-optical superconducting magnet system producing a horizontal magnetic field. (b) Current flow Helmholtz coils with radius a . The violet arrows indicate the current I and the dashed lines the magnetic field. The incident light wave vector k is parallel to the magnetic field direction (Faraday configuration).

variable temperature insert (VTI) keeps the sample in the center and controls the lattice temperature. It is connected to the helium chamber by a tunable needle valve.

The sample rod is a long copper stick with temperature sensing and a wiring system for controlled heating. It can be manually turned on its vertical axis. The spectromag is a top loading system which enables sample change even while the dewar is kept at low temperature. A tailored frame places the spectromag on the optical table allowing for precise lateral shift relative to the beam height. In the spectromag, the sample is positioned between two identical superconducting coils (Helmholtz coils) separated by a distance equal to the radius. The current flow is the same in both coils, where each of them generates a magnetic field. The configuration which is designed such that both coils are on the same horizontal axis generates a finite volume with nearly homogeneous magnetic field. All our measurements have been performed in Faraday geometry where the magnetic field direction is parallel to the incident light wave vector k . In Figure 3.3(b), the dotted line indicates the incident light. For measurements in Faraday configuration, we use the windows along the bore which is 80 mm in diameter. However, the cold window of the VTI is 10 mm in diameter limiting the clear access to the sample space. The stray magnetic field influences the operation of the streak tube as the Lorentz force bends the electron

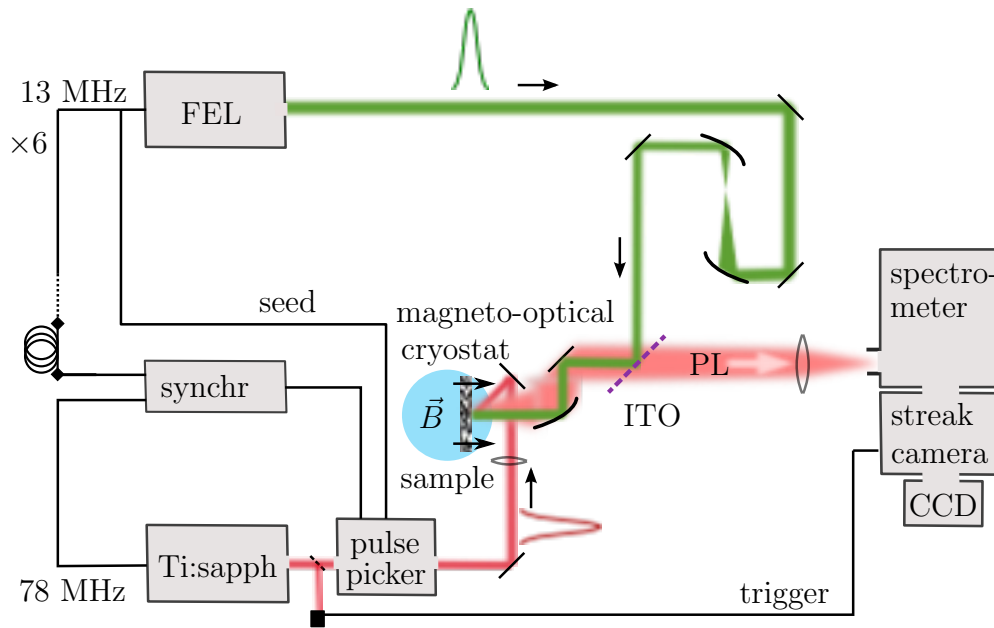


Figure 3.4: Scheme of the experimental setup for two-color time-resolved photoluminescence measurements with external magnetic field. Red and green lines indicate the near-infrared and the THz beam paths, respectively. Black lines are cable connections for synchronization. The PL is free-space guided and focused into the entrance slit of the spectrometer.

beam. According to the manual, a magnetic field strength of 2 mT can be detected for 7 T in a distance of 1 m from the center of the magnet. At a distance of 2 m, the reported stray field is smaller than 0.5 mT. We left a working distance of 3.2 m between the magnet and the streak camera to ensure negligible deflection of the electron beam of the streak tube. To fulfill the requirements for magneto PL detection, the standard experimental setup in Figure 3.2 was modified. The new scheme of the magneto PL setup is shown in Figure 3.4. In this configuration, the THz beam diameter is narrowed by means of two parabolic mirrors. The beam splitter is an indium tin oxide (ITO) layer on quartz glass which is highly reflective to the THz radiation and transmits the visible light. The emitted PL propagates in free space with one mirror after the cryostat window towards the entrance slit of the spectrometer. Nothing changes with respect to synchronization. The temporal delay between the near-infrared laser pulse and the THz is adjusted with a variable coaxial line.

3.6 GaAs quantum well samples

Gallium arsenide (GaAs) is a III-V compound semiconductor material with a zinc blende crystal structure. GaAs is a direct gap material with a band gap of 1.52 eV at 4 K [Sze07]. The valence band maximum and the conduction band minimum correspond to

sample	composition (well/barrier)	well width	PL emission	line width
1267	40× GaAs/Al _{0.35} Ga _{0.65} As	6 nm	1.604 eV	8 meV
DBR42	20× In _{0.06} Ga _{0.94} As/GaAs	8 nm	1.471 eV	1 meV
H063	60× GaAs/Al _{0.34} Ga _{0.66} As	8.2 nm	1.573 eV	3 meV

Table 3.1: Characteristics of the studied samples.

zero momentum, and radiative recombination is possible without phonon emission or absorption. Popular ternary alloys are, e.g., Al_xGa_{1-x}As, where the Ga is exchanged by Al atoms to a certain fraction x . These materials have different band gaps but similar lattice constants compared to GaAs, which is the requirement for the growth of multiple quantum wells without strain or lattice defects. The samples are grown by molecular beam epitaxy. This technique produces layers with high precision on atomic length scale and high purity of less than 10^{14} cm^{-3} foreign atoms. The typical exciton Bohr radius for bulk GaAs of 13 nm [Pel12] is much larger than the lattice constant 0.56 nm [Sze07] making this material a preferred candidate to grow quantum wells. The investigated multiple quantum well samples and their basic characteristics are listed in Table 3.1. In the following subsections, details on the sample's PL characteristics are given.

3.6.1 Sample 1267

The quantum well sample 1267 is a layer stack of 40 periods of 6 nm thick undoped GaAs wells grown on GaAs substrate by Klaus Köhler, Fraunhofer Institute for Applied Solid State Physics, Freiburg. The wells are separated by 15 nm thick Al_{0.35}Ga_{0.65}As barriers. As a first characterization, typical PL spectra and transients measured at 4 K lattice temperature are plotted in Figure 3.5. For all studied excitation densities, the excitonic PL peak is detected at 1.604 eV with a linewidth of 8 meV, see Figure 3.5. The logarithmic scale in 3.5(b) emphasizes the fast rise and the monoexponential decay of the PL intensity. Furthermore, we performed temperature dependent studies of the 1267 quantum well sample. The corresponding PL spectra and transients are shown for eight different lattice temperatures between 10 K and 65 K measured with the same excitation density. A single PL emission peak is observed for all studied temperatures. While the energy shift is negligibly small in the range between 10 K and 55 K, see Figure 3.6(a), a redshift is observed for higher lattice temperatures due to band gap narrowing. As can be seen in Figure 3.6(b), the signal intensity and the PL dynamics are strongly influenced by the lattice temperature. For higher temperatures, the free excitons occupy mostly high momentum states which reduces the radiative recombination rate. Thermal dissociation of excitons might explain the decrease of the PL intensity [Cer95].

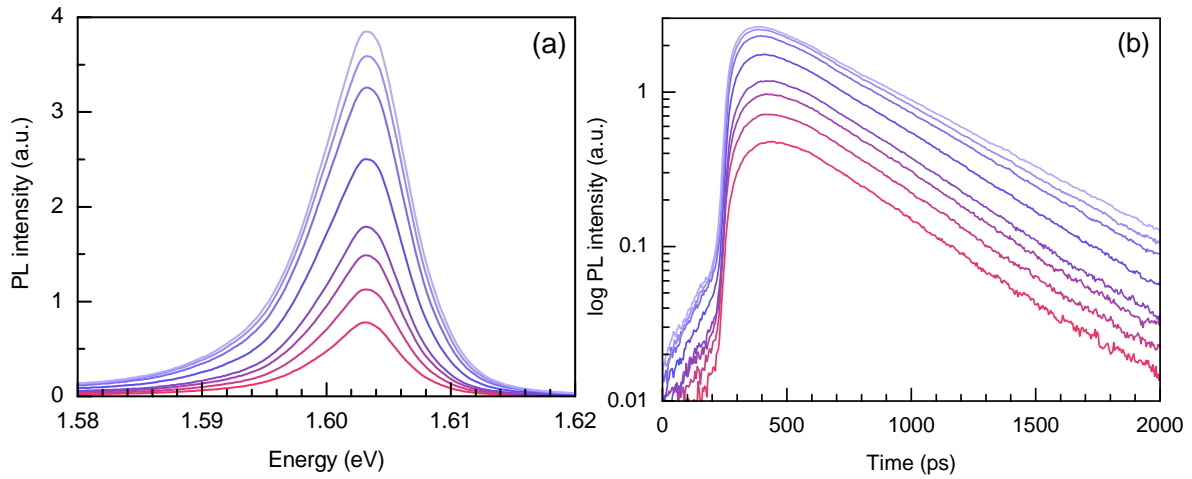


Figure 3.5: Photoluminescence emission of sample 1267 after non-resonant excitation with near-infrared laser pulses. (a) PL spectra and (b) time-evolution of the PL signal at the maximum emission peak in logarithmic scale. The excitation fluences are (from lower to upper curve): $4 \mu\text{J cm}^{-2}$, $5 \mu\text{J cm}^{-2}$, $7 \mu\text{J cm}^{-2}$, $9 \mu\text{J cm}^{-2}$, $13 \mu\text{J cm}^{-2}$, $18 \mu\text{J cm}^{-2}$, $22 \mu\text{J cm}^{-2}$, and $27 \mu\text{J cm}^{-2}$.

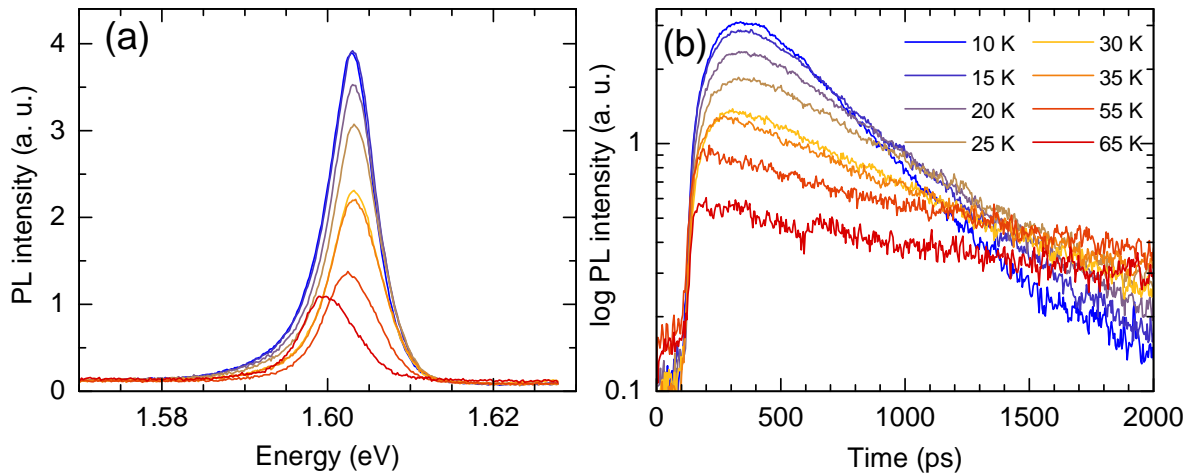


Figure 3.6: PL spectra (a) and transient PL signal (b) for different lattice temperatures between 10 K and 65 K. The excitation fluence is $1 \mu\text{J cm}^{-2}$ for all measured curves.

3.6.2 Sample DBR42

The quantum well sample DBR42 has 20 periods of 8 nm wide $\text{In}_{0.06}\text{Ga}_{0.94}\text{As}$ wells separated by 130 nm GaAs barriers grown by G. Khitrova and H. Gibbs, University of Arizona, Tucson, USA. The sample is grown on semi-insulating, undoped GaAs substrate. An anti-reflection coating reduces Fabry-Perot interference fringes. The indium atoms induce strain and increase the heavy hole-light hole splitting compared to GaAs quantum wells. The $1s(\text{hh})$ PL line is shifted well below the GaAs band gap energy. As the residual substrate absorption is small, InGaAs quantum wells are suitable for measurements in transmission geometry. The exciton line is at 1.471 eV at 4 K lattice temperature with an exciton linewidth as narrow as 0.96 meV full width at half maximum. For this sample, the $2s$ resonance is 6.9 meV above the $1s$ resonance. More details on sample DBR42 including absorption spectra are presented in [Cha03, Cha04].

3.6.3 Sample H063

The quantum well sample H063 is a sample with 60 periods grown on semi-insulating GaAs substrate by the group of G. Strasser, Micro- and Nanostructure Center, TU Wien, Austria. The GaAs wells are 8.2 nm thick and separated by 19.6 nm wide barriers of $\text{Al}_{0.34}\text{Ga}_{0.66}\text{As}$. The emitted PL shows a linewidth of less than 3 meV. The intraexcitonic level separation has been determined to 8.7 meV in previous studies [Wag09b, Wag10]. As a first characterization, two sets of time-integrated PL spectra of this high-quality

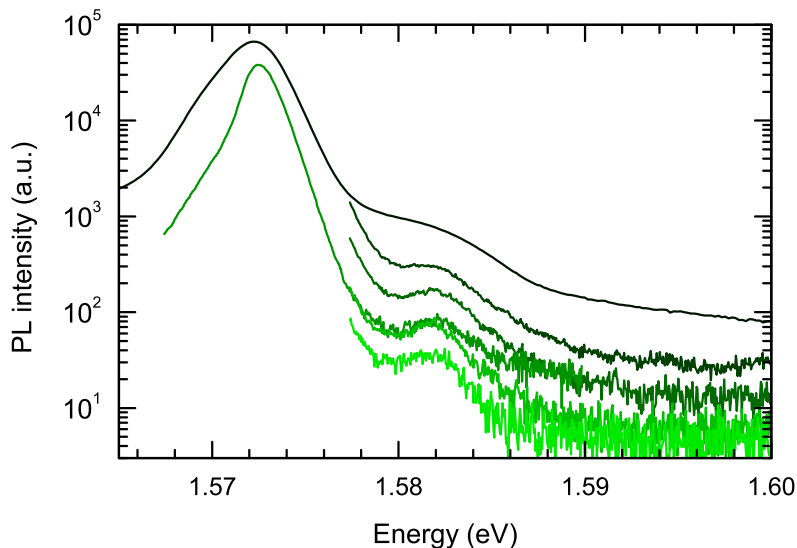


Figure 3.7: Time integrated spectra of sample H063 for high excitation densities. The estimated carrier densities induced by the near-infrared excitation are (from the upper to the lower curve) as follows: $8 \times 10^{10} \text{ cm}^{-2}$, $4 \times 10^{10} \text{ cm}^{-2}$, $2 \times 10^{10} \text{ cm}^{-2}$, $6 \times 10^9 \text{ cm}^{-2}$, $6 \times 10^9 \text{ cm}^{-2}$ (detected with half slit width), and $3 \times 10^9 \text{ cm}^{-2}$.

quantum well sample are plotted in Figure 3.7 for near-infrared excitation densities between $8 \times 10^{10} \text{ cm}^{-2}$ and $3 \times 10^9 \text{ cm}^{-2}$. While the two curves showing both PL peaks are measured with the 600 lines/mm grating, the four curves showing only the $2s$ PL peak are taken with the higher resolution 1200 lines/mm grating. With increasing density, the $1s$ exciton line at 1.572 eV broadens. The $2s$ PL emission is clearly visible for low densities and merges with the $1s$ PL emission peak for higher densities indicating the transition from excitonic characteristics to electron-hole plasma.

4 Photoluminescence dynamics under pulsed intersubband excitation

In this chapter, we investigate transient quenching of PL signals from the undoped GaAs quantum well sample 1267 induced by mid-infrared pulses from the free-electron laser. The photon energy of the laser is tuned to resonance with the intersubband transition leading to efficient carrier excitation. When performing polarization sensitive measurements, free-carrier absorption and intersubband transition are distinguished as the two competing processes that cause the decrease of the PL intensity under resonant mid-infrared irradiation. A function is fitted to the experimental data which is based on solutions of rate equations where the system is reduced to two effective levels.

Parts of this chapter have been published previously [Zyb11].

4.1 Photoluminescence quenching under resonant intersubband excitation

As introduced in the Chapter 2, intersubband transitions occur between quantized states within the same band. Thus, either electrons or holes are involved in the transition which results in the same dispersion relation in momentum space for the initial and the final state. The emitted infrared light emission monitors the carriers in the conduction band that recombine radiatively while dark states with high momentum do not contribute to the PL intensity. An approach to unveil the hidden carrier dynamics are time-resolved PL studies under simultaneous excitation processes. Transient PL quenching using a second delayed interband excitation pulse was demonstrated in [Amo08, Amo10]. Earlier, the suppression of time-integrated PL under far-infrared radiation was explained by exciton ionization as well as inhibited exciton formation [Qui92, Cer96].

In order to gain more insight into the intersubband carrier dynamics, we performed time-resolved PL measurements on undoped quantum wells under resonant mid-infrared excitation. A near-infrared laser pulse from the Ti:sapph laser induces an interband transition leading to radiative recombination of the excited population. The emitted PL signal is efficiently quenched by the absorption of a delayed pulse from the free-electron laser,

which is in resonance to the intersubband energy. Thus, our two-color experiment ensures a pure redistribution of the prepared carrier distribution in the conduction band without injection of new carriers. This fact has been proven by time-integrated measurements that show that integrated PL intensities with and without THz excitation are the same. The in-plane energy dispersion of the two subbands is schematically shown in Figure 4.1, where the vertical arrows indicate possible absorption processes. After the near-infrared excitation pulse has excited carriers over the bandgap, a delayed mid-infrared pulse induces resonant intersubband absorption and free-carrier heating which result in transient quenching of the PL signal. Note that free-carrier absorption is a second-order process, where phonons or elastic scattering processes are required to fulfill energy and momentum conservation rules. The absorption coefficient $\alpha(\omega)$ for free-carrier absorption is proportional to λ^2 , see Equation (2.8). Therefore, this process is particularly important in the THz range.

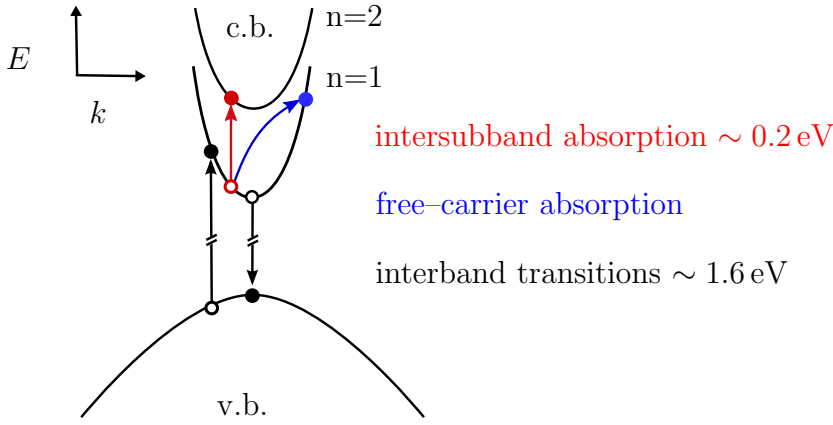


Figure 4.1: The in-plane energy dispersion of the two subbands. Vertical arrows indicate interband absorption by near-infrared excitation (black). Intersubband absorption (red) and free-carrier absorption (blue) might occur under resonant mid-infrared excitation.

We have studied intersubband transitions on the GaAs/AlGaAs quantum well sample 1267 with 6 nm wide wells. The transition between the two lowest confined subbands in the conduction band is allowed by parity selection rules. The two-color experiments are performed with two pulse sources, the synchronization unit, and the streak camera detection as described in Chapter 3 and depicted in Figure 3.2. The sample was mounted in an optical cryostat and kept at a lattice temperature of 10 K. The near-infrared pulses from the Ti:sapph laser were about 2 ps long with a photon energy of 1.635 eV which is larger than the energy gap of the quantum well sample. The average power was 2 mW creating a free carrier density of approximately $5 \times 10^{10} \text{ cm}^{-2}$ per well via interband excitation. The free-exciton PL peak is detected at 1.604 eV with a line width (FWHM) of 8 meV. The intersubband spacing of 172 meV is larger than the LO phonon energy

in GaAs bulk material of 36 meV. With this experiment, the carrier relaxation mediated by the emission and absorption of phonons was studied. For lattice temperatures below 10 K, the cooling due to the emission of LO phonons occurs on a picosecond time scale while the emission of acoustic phonons is in the range of nanoseconds. After intersubband excitation, the created population in the upper subband energetically relaxes to the lower subband.

The time delay t_{MIR} between the near-infrared and mid-infrared pulses is set through the Ti:Sapph laser synchronization to the FEL clock. As the mid-infrared pulses are short, the transient PL signal monitors the quenching and carrier relaxation after external perturbation. In Figure 4.2, streak images of time-resolved PL from the quantum well sample 1267 are shown in (a) without and in (b) and (c) with mid-infrared excitation. Temporal profiles at the peak energy are plotted in Figure 4.2(d) for mid-infrared fluences varied between $1.5 \mu\text{J cm}^{-2}$ and $51.4 \mu\text{J cm}^{-2}$. These profiles are compared with the reference PL transient taken without a second excitation. Dotted vertical lines indicate the arrival time of the optical and the mid-infrared laser pulse. At the arrival time of the mid-infrared excitation pulse, the PL signal intensity drops abruptly. Carriers are excited from bright states into dark states and do not longer contribute to the emitted PL signal.

The amount of quenching increases with increasing mid-infrared fluence and saturates for stronger excitation. After reaching a minimum, the PL intensity recovers to a value higher than the reference trace. In the studied mid-infrared intensity regime, the PL signal overshoot compensates the PL quench perfectly. This fact has been verified by time-integrated PL measurements indicating negligible carrier losses due to non-radiative channels.

4.2 Modeling the induced photoluminescence dynamics

In order to quantify the PL dynamics under mid-infrared excitation, we introduce a rate equation model based on two effective levels, which describes the measured transients well. This simple approach reduces the system to a carrier population that occupies either radiative (optically bright) or non-radiative (optically dark) states. This model does not distinguish between momentum relaxation and exciton formation, both processes together constitute here the slow PL rise time. In previous publications [Tak92, Tsa01, Gal05], transient PL signals of narrow InGaAs/GaAs quantum well samples have been modeled with similar approaches that are based on two effective levels. In a first subsection, we develop the rate equations that are sufficient to describe the dynamics of the radiative and non-radiative population of the unperturbed system after an initial excitation at $t_0 = 0$. In a second step, the induced relative quenching and the PL recovery are included.

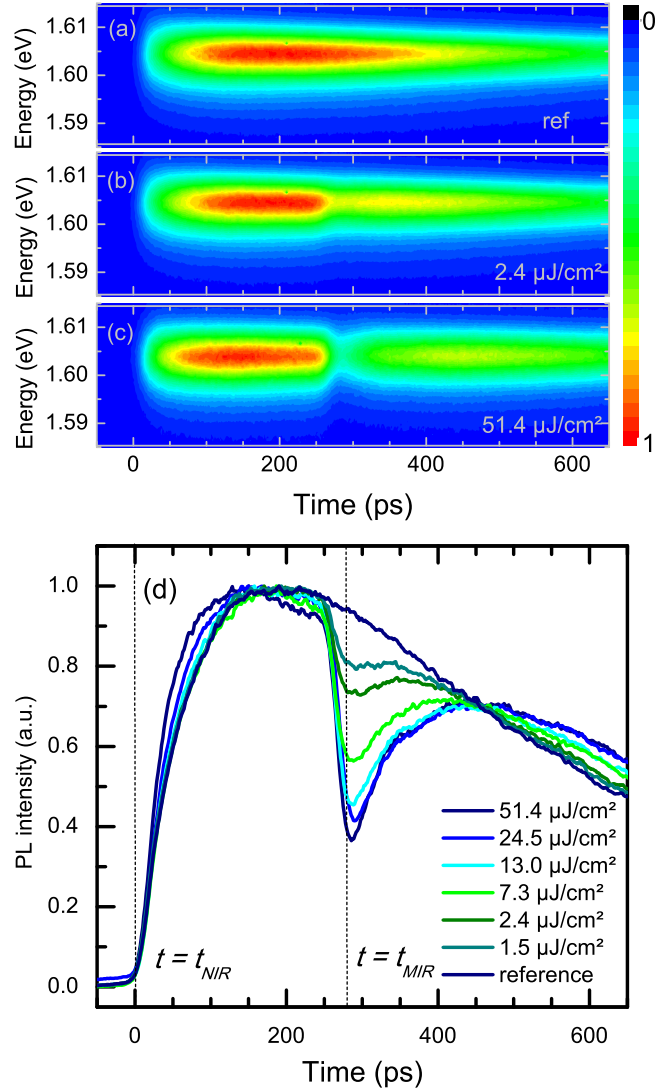


Figure 4.2: Time-resolved PL signal from quantum wells of the sample 1267 showing a PL quenching under pulsed mid-infrared irradiation. The subfigures show the streak images (a) without free-electron laser irradiation, (b) with $2.4 \mu\text{J cm}^{-2}$, and (c) with $51.4 \mu\text{J cm}^{-2}$ mid-infrared excitation density. The colors indicate the signal intensity from minimum (blue) to maximum (red). (d) Normalized PL transients taken under mid-infrared irradiation of $1.5 \mu\text{J cm}^{-2}$ (green) to $51.4 \mu\text{J cm}^{-2}$ (blue) as well as the reference trace without quenching (dark blue). The dotted lines mark the temporal position of the near-infrared excitation ($t_{\text{NIR}} = 0$) and the delayed mid-infrared laser pulse ($t_{\text{MIR}} = 280$ ps) from the free-electron laser.

4.2.1 Photoluminescence transients without quenching

Based on the in-plane energy dispersion with two subbands shown in Figure 4.1, the scheme of the induced PL emission from the quantum well system is depicted in Figure 4.3(a). The dispersion curves of the involved subbands are reduced to a two-level problem. Under these simplified conditions, we assume a population transfer from the valence band into the conduction band through a laser pulse excitation that exceeds the band gap energy. The induced hot carrier distribution in the lowest subband of the conduction band relaxes due to photon emission towards low momentum states and radiatively recombines with a characteristic PL decay time τ_{PL} . Figure 4.3(b) depicts the levels and relaxation times which are regarded for building the rate-equation system.

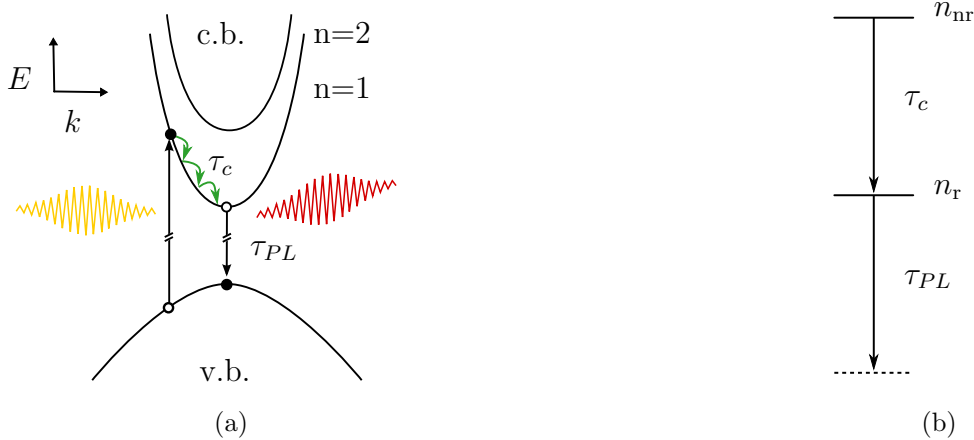


Figure 4.3: (a) Scheme of the excitation and relaxation processes within the quantum well dispersion curves. The parameter τ_c quantifies the cooling process in the conduction band (c.b.) due to LO phonon emission (green arrows). The emitted PL signal with time constant τ_{PL} is indicated in red. (b) Flow diagram of the model with the non-radiative level n_{nr} , the radiative level n_r , and the ground state (dotted line).

The detected PL intensity is assumed to be proportional to the dimensionless occupation number of the radiative state $n_r(t)$ as a function of time t . Strictly speaking, $n_r(t)$ expresses a cold exciton distribution that is almost completely composed of dark states. The remaining fraction of bright states has a picosecond life time. The precise composition of the radiative state $n_r(t)$ is taken into account by a microscopic many-body theory which has been developed by Koch et al. [Kir04, Koc06]. The parameter τ_c is the cooling time of the carriers from the non-radiative to the radiative state. From the effective radiative state, the carriers recombine on a nanosecond time scale to the ground state resulting in a PL decay constant τ_{PL} . The dimensionless occupation number of the non-radiative state is $n_{nr}(t)$. For a simple solution, the arrival time of the near-infrared

pulse t_0 is set to 0 and the near-infrared induced initial occupation number to 1, i.e., a 100% occupation. Under these assumptions, two coupled rate equations

$$\frac{d}{dt} \begin{pmatrix} n_{\text{nr}}(t) \\ n_{\text{r}}(t) \end{pmatrix} = \begin{pmatrix} -\frac{1}{\tau_{\text{c}}} & 0 \\ \frac{1}{\tau_{\text{c}}} & -\frac{1}{\tau_{\text{PL}}} \end{pmatrix} \begin{pmatrix} n_{\text{nr}}(t) \\ n_{\text{r}}(t) \end{pmatrix} \quad (4.1)$$

are built with the initial conditions $n_{\text{r}}(0) = 0$ and $n_{\text{nr}}(0) = 1$. Equation (4.1) forms a system of first order ordinary differential equations. The solution that fulfills the initial conditions is

$$n_{\text{nr}}^{\text{I}}(t) = e^{-\frac{t}{\tau_{\text{c}}}} \quad (4.2)$$

$$n_{\text{r}}^{\text{I}}(t) = \frac{\tau_{\text{PL}}}{\tau_{\text{PL}} - \tau_{\text{c}}} \left(e^{-\frac{t}{\tau_{\text{PL}}}} - e^{-\frac{t}{\tau_{\text{c}}}} \right), \quad t > 0. \quad (4.3)$$

Thus, the transient PL intensity can be expressed by the sum of two exponential functions that describes the carrier relaxation between an upper non-radiative and the lower radiative level. The label I indicates the solution for the unperturbed system and will be of importance below when the functions with quench are derived.

For data analysis, the detected PL signal is assumed to be proportional to the radiative population given in Equation (4.3). In order to account for the time resolution of the experimental setup, the calculated PL dynamics is convoluted with a Gaussian function,

$$G_{\sigma}(t) = \frac{1}{\sqrt{2\pi}\sigma} e^{-\frac{t^2}{2\sigma^2}}, \quad t \in \mathbb{R}, \quad \sigma > 0, \quad (4.4)$$

where σ is the standard deviation of the Gaussian function with full width at half maximum (FWHM) of $\sqrt{2 \ln 2} \sigma$. The resulting function $I_{\text{PL}}(\sigma, t)$ that is applied to the experimental data can be written as the convolution

$$I_{\text{PL}}(\sigma, t) = I_0 (n_{\text{r}}^{\text{I}} * G_{\sigma})(t) \quad (4.5)$$

$$= I_0 \int_0^{\infty} n_{\text{r}}^{\text{I}}(s) G_{\sigma}(t-s) ds, \quad (4.6)$$

where the amplitude scaling factor I_0 adjusts for the measured signal intensity. A user-defined fit function *fit-PL* is created that is based on $I_{\text{PL}}(\sigma, t)$, see Equation (4.5), using the data analysis and graphing software OriginLab[®]. The free parameters are the cooling time τ_{c} , the PL decay time τ_{PL} , and the amplitude scaling factor I_0 . The time resolution σ is adjusted depending on the individual experimental conditions.

As an example, PL transients from sample 1267 are analyzed for different lattice temperatures between 5 K and 65 K. Figure 4.4 shows two normalized intensity profiles and the respective model fits that accurately describe the measured data. The temporal res-

olution σ of the experiment is about 15 ps. With increasing lattice temperature, the PL rise time decreases while the PL decay time increases.

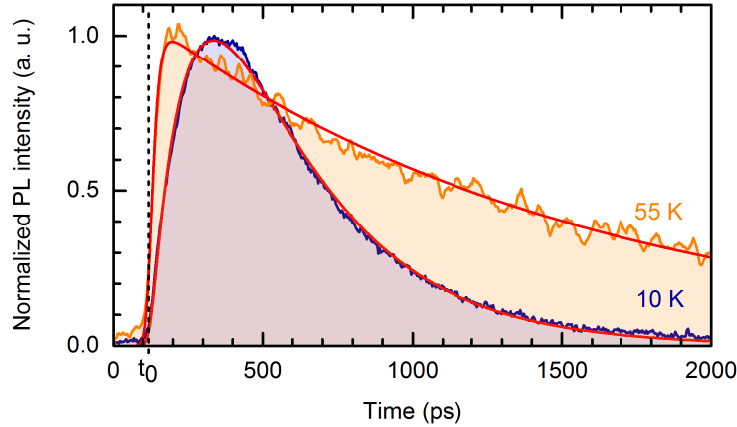


Figure 4.4: Normalized PL transients measured with lattice temperatures 10 K (blue line) and 55 K (orange line), respectively. The red lines are modeled curves with the parameters $\sigma = 15$ ps, $\tau_c^{10\text{K}} = 123$ ps, $\tau_{\text{PL}}^{10\text{K}} = 0.4$ ns, and $\tau_c^{55\text{K}} = 23$ ps, $\tau_{\text{PL}}^{55\text{K}} = 1.9$ ns. The arrival time of the near-infrared laser pulse t_0 is marked with a dashed line.

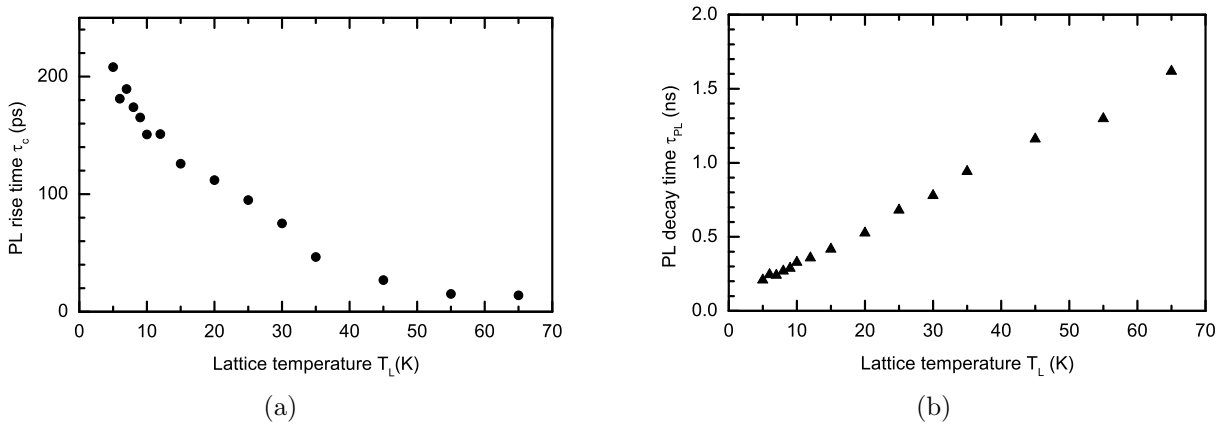


Figure 4.5: The results of the rate equation fit on the temperature dependent data. (a) PL rise time τ_c as a function of lattice temperature T_L . (b) PL decay time τ_{PL} as a function of lattice temperature T_L .

The results of this temperature study are plotted in Figure 4.5 as a function of lattice temperature T_L . The PL rise time τ_c linearly decreases between 5 K and 55 K, see Figure 4.5(a). The data analysis is limited by the time resolution σ of the experiment and the signal-to-noise ratio. In Figure 4.5(b), the linear rise of the PL decay time is shown.

4.2.2 Photoluminescence transients with induced quenching

In order to evaluate the PL transients with quench, the simple model for the rate equation analysis is modified. A partition of the time axis is defined, where regime I denotes the unperturbed time span starting at t_0 . Regime II starts with the arrival time of the mid-infrared pulse t_{MIR} , where a fraction q of the population is transferred from the radiative effective level to the non-radiative one. The quenching parameter q , $0 \leq q \leq 1$, parameterizes the observed dip depth in the measured PL transient. Note that a full quench ($q = 1$) does not mean population inversion but depletion of the radiative state due to efficient carrier redistribution. As in the previous case, the initial near-infrared pulse excites carriers nonresonantly across the bandgap into hot states, and the total amount of carriers is kept constant for all modeled curves. The mid-infrared pulse causes a redistribution of the population but no injection of new carriers. With the adjusted initial conditions

$$n_{\text{nr}}^{\text{II}}(t_{\text{MIR}}) = n_{\text{nr}}^{\text{I}}(t_{\text{MIR}}) + q n_{\text{r}}^{\text{I}}(t_{\text{MIR}}) \quad , \quad (4.7)$$

$$n_{\text{r}}^{\text{II}}(t_{\text{MIR}}) = (1 - q) n_{\text{r}}^{\text{I}}(t_{\text{MIR}}) \quad , \quad (4.8)$$

the solution of the rate equation (4.1) is

$$n_{\text{nr}}^{\text{II}}(t) = e^{-\frac{t-t_{\text{MIR}}}{\tau_c}} (a + b q) \quad , \quad t > t_{\text{MIR}} \quad (4.9)$$

$$n_{\text{r}}^{\text{II}}(t) = \frac{1}{\tau_{\text{PL}} - \tau_c} \left(e^{-\frac{t-t_{\text{MIR}}}{\tau_{\text{PL}}}} (\tau_c (b - bq) - \tau_{\text{PL}} (a + b)) + e^{-\frac{t-t_{\text{MIR}}}{\tau_c}} \tau_{\text{PL}} (a + bq) \right) \quad (4.10)$$

where $a = n_{\text{nr}}^{\text{I}}(t_{\text{MIR}}) = e^{-\frac{t_{\text{MIR}}}{\tau_c}}$ and $b = n_{\text{r}}^{\text{I}}(t_{\text{MIR}}) = \frac{\tau_{\text{PL}}}{\tau_{\text{PL}} - \tau_c} (e^{-\frac{t_{\text{MIR}}}{\tau_{\text{PL}}}} - e^{-\frac{t_{\text{MIR}}}{\tau_c}})$ are the occupation numbers of the non-radiative and the radiative levels of the unperturbed system at time t_{MIR} , see Equations (4.2) and (4.3). The total non-radiative population dynamics for both regimes can be expressed as

$$n_{\text{nr}}(t) = \begin{cases} n_{\text{nr}}^{\text{I}}(t) \quad , & t_0 \leq t < t_{\text{MIR}} \\ n_{\text{nr}}^{\text{II}}(t) \quad , & t \geq 0 \\ 0 \quad , & \text{otherwise} \end{cases} \quad . \quad (4.11)$$

Analogously, the total radiative population dynamics for both regimes is

$$n_{\text{r}}(t) = \begin{cases} n_{\text{r}}^{\text{I}}(t) \quad , & t_0 \leq t < t_{\text{MIR}} \\ n_{\text{r}}^{\text{II}}(t) \quad , & t \geq 0 \\ 0 \quad , & \text{otherwise} \end{cases} \quad . \quad (4.12)$$

The modeled dynamics of the non-radiative population $n_{\text{nr}}(t)$ given in Equation (4.11) is plotted in Figure 4.6(a) and compared with the unperturbed case $n_{\text{nr}}^{\text{I}}(t)$ without a second excitation. The non-radiative population is induced by a laser pulse at $t_0 = 0$ and shows a monoexponential decay. The second excitation pulse transfers a certain fraction q of the radiative state population into the non-radiative state which is reflected in the instantaneous enhancement of the non-radiative population at time t_{MIR} .

In Figure 4.6(b), the radiative population $n_{\text{r}}(t)$ given in Equation (4.12) is plotted. According to the initial conditions, the radiative population is zero at $t = 0$. The rise time and the decay time of the modeled curve are specified by the parameters τ_{c} and τ_{PL} , respectively. The second excitation pulse induces an abrupt drop of the radiative state population and a subsequent signal recovery due to relaxation processes from the non-radiative level into the radiative one. As above, the detected PL signal is assumed to be proportional to the radiative population given in Equation (4.12). As performed for the unperturbed case, the calculated level occupation number is convoluted with a Gaussian function

$$I_{\text{PL}}(\sigma, t) = I_0 (n_{\text{r}} * G_{\sigma})(t), \quad t > 0. \quad (4.13)$$

In Figures 4.6(c) and 4.6(d), the convoluted functions are shown and compared with the modeled curves. The labels I and II denote the time regimes after the initial excitation and after the mid-infrared pulse, respectively. The most noticeable difference is the reduced dip depth in Figure 4.6(d) due to the simulated time resolution of $\sigma = 15$ ps.

Two fit functions *fit-PL* and *fit-PL-dip* are created that are based on Equations (4.5) and (4.13) for the signal without and with induced quenching, respectively. For analysis of the PL quenching data, the fit procedure is performed in two steps. From the reference trace without quenching, the parameters t_0 , τ_{c} , τ_{PL} , and I_0 are extracted. In a second step, these values are kept fixed. The only free parameters for the fit of the trace with quench using *fit-PL-dip* based on Equation (4.13) are the arrival time of the mid-infrared laser pulse t_{MIR} and the relative quenching q , respectively. The Gaussian width σ was about 25 ps for the mid-infrared quenching experiment and is mainly attributed to laser pulse length and the jitter of the laser synchronization. For all of the fitted PL transients, the PL rise time $\tau_{\text{c}}^{\text{I}}$ is found to have the same values as the PL recovery time after the quenching $\tau_{\text{c}}^{\text{II}}$.

4.3 Probing of local lattice heating

In the example that was shown in the previous subsection, the carrier cooling time and the PL decay times depend strongly on the lattice temperature T_{L} . The increased phonon densities cause faster cooling of the excited carriers leading to shorter PL rise times. The

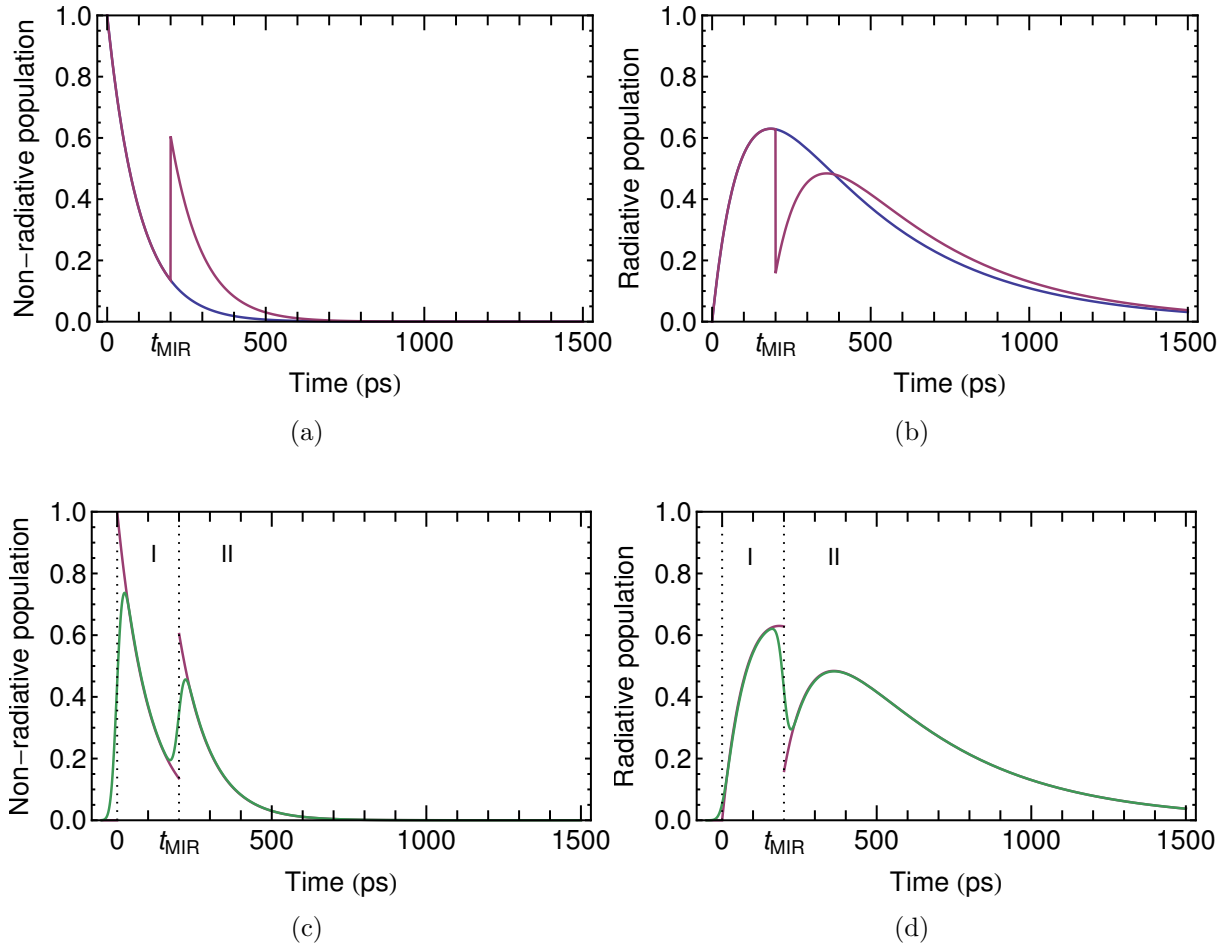


Figure 4.6: Modeled dynamics of the non-radiative $n_{\text{nr}}(t)$ (a) and radiative $n_{\text{r}}(t)$ (b) population after an initial excitation at $t_0 = 0$ (blue). The violet curves show the dynamics of the population with a second excitation at $t = t_{\text{MIR}}$. The curves are plotted with parameters $t_0 = 0$, $t_{\text{MIR}} = 200$ ps, $\tau_{\text{c}} = 100$ ps, $\tau_{\text{PL}} = 400$ ps, $q = 0.75$. The two lower subfigures show the non-radiative (c) and radiative (d) population dynamics with a finite time resolution of $\sigma = 15$ ps.

PL decay becomes slower with increasing temperature as a smaller fraction of excitons is in radiative states.

In the frame of a comparative study, the heat impact into the lattice is investigated depending on the mid-infrared fluence. A first data set is taken at 10 K with increasing mid-infrared fluence and a second one without mid-infrared excitation for different lattice temperatures between 10 K and 35 K. The transient PL signals with mid-infrared excitation at $t = t_{\text{MIR}}$ with fluence $7 \mu\text{J cm}^{-2}$ and without a second excitation for a lattice temperature of 10 K are shown in Figure 4.7(a). The experimentally derived PL transients are well described using the fit functions *fit-PL* and *fit-PL-dip* derived from Equations (4.5) and (4.13), respectively. This simple model allows for the deduction of the cooling time τ_c and the PL decay time τ_{PL} . A linear behavior is found for the decrease of τ_c and the increase of τ_{PL} , see Figures 4.7(b) and 4.7(c). The time constants τ_c and τ_{PL} for the maximum mid-infrared fluence of $51 \mu\text{J cm}^{-2}$ correlate with the data taken for a lattice temperature of 28 K without mid-infrared fluence. Note the labeling of the axes at the top (lattice temperature) and the bottom (MIR fluence) and that both data sets start at 10 K and zero mid-infrared fluence. According to these findings, the PL dynamics can serve as a sensitive probe of local lattice heating in a temperature range with negligible spectral shift. With increasing lattice temperature, a higher number of carriers has a

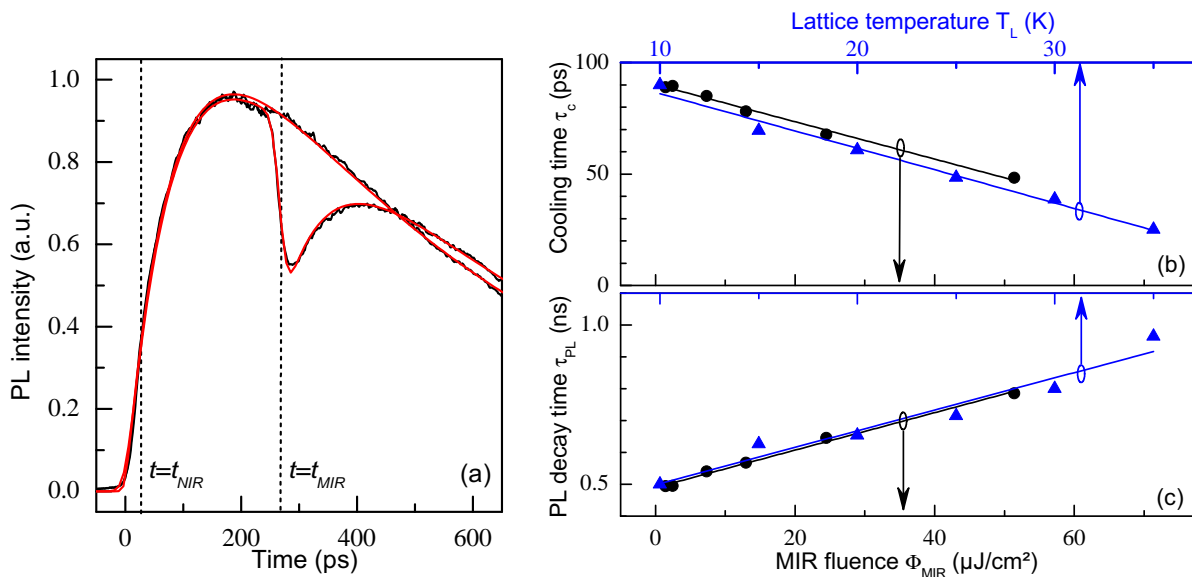


Figure 4.7: (a) Transient PL signal with dip at $t = t_{\text{MIR}}$ for mid-infrared fluence of $7 \mu\text{J cm}^{-2}$. The red curves show the modeled curves. (b) Cooling time τ_c and (c) PL decay time τ_{PL} as a function of mid-infrared fluence (black bullets) and lattice temperature (blue triangles). The solid lines show their corresponding linear fits.

sufficient energy for the emission of fast-relaxation LO phonons [Cer95], which becomes noticeable through the decrease of the cooling time τ_c . The PL decay time τ_{PL} linearly

increases for all measured temperatures. This linear behavior has been shown earlier, e.g. in [Fel87], where a PL decay time of 2 ns at $T_L = 30$ K is reported for a quantum well sample under comparable conditions.

4.4 Polarization dependent photoluminescence quenching

Resonant mid-infrared pulses do not only excite intersubband transitions but induce free-carrier absorption as well. While intersubband transitions require the electric field of the radiation to be parallel to the growth direction of the quantum wells [Hel00], see Section 2.2, free-carrier absorption occurs for electric field within the quantum well plasma. Providing the field component for intersubband transitions can be realized by applying grating couplers on the quantum wells or by coupling the radiation via a waveguide facet. In our experiment, a 45° polished facet as depicted in Figure 4.8 is applied. The near-infrared laser beam is directly focused on the quantum well layers under small angle of incidence. The mid-infrared laser is reflected onto a gold coated surface and coupled into the sample via the facet in order to obtain an electric field component perpendicular (p-polarization) or parallel (s-polarization) to the quantum well plane. In this configuration, intersubband transitions are excited only for p-polarized radiation while free-carrier absorption occurs for both polarization directions. With the second facet, the mid-infrared light is efficiently coupled out to prevent effects that arise from multiple reflections inside the waveguide.

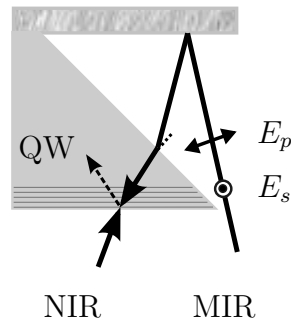


Figure 4.8: Scheme of the measurement geometry for coupling the p- and s-polarized radiation to the 45° facet of the sample.

Intersubband absorption width

Initially, the intersubband energy of sample 1267 was estimated as 157 meV by solving the Schrödinger equation in a one-particle picture based on the nominal growth parameters. However, the intersubband energy becomes larger at higher densities due to many-body

effects as has been derived, e.g., by [Ram90]. From our experiments at 157 meV, it can be concluded that PL quenching at this energy is weak and not sensitive with respect to polarization changes. Thus, the induced quenching was studied for mid-infrared photon energies between 157 meV and 179 meV. The resonant data at 172 meV are compared with PL quenching at detuned photon energies. The results are shown in Figure 4.9. The low absolute values for the dip depth in Figure 4.9(a) are a consequence of the not perfectly aligned spatial overlap of the two laser spots. The difference between p- and s-polarized quenching at $7 \mu\text{J cm}^{-2}$ for different mid-infrared photon energies is shown in Figure 4.9(b). In a first set of measurements, the mid-infrared photon energy was changed between 157 meV and 172 meV resulting in increased dip depth and stronger polarization dependency. A second data set shows a decrease of induced PL quenching between 172 meV and 179 meV.

Polarization-dependent behavior was found for energies between 168 meV and 179 meV. The largest difference between the two polarization directions was found for the intersubband resonance at 172 meV while the absolute numbers vary due to alignment and experimental differences. From these observations, the width of the intersubband absorption line is estimated as 10 meV (FWHM) while the Drude-type free-carrier absorption is observed for all studied photon energies.

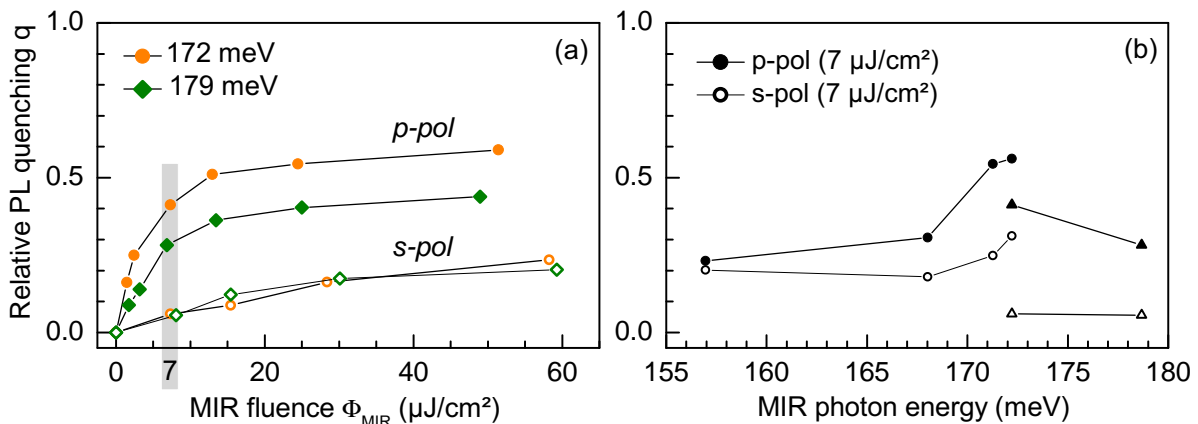


Figure 4.9: Verification of the intersubband resonance. (a) Saturation behaviour of the relative PL quenching for p-polarized (solid symbols) and s-polarized (open symbols) light for mid-infrared photon energies of 172 meV (resonant case) and 179 meV. (b) Two data sets of polarization sensitive PL quenching as a function of mid-infrared photon energy for p-polarized (solid symbols) and s-polarized (open symbols) light.

Saturation behavior of the PL quenching

In the previous subsection, the mid-infrared photon energy 172 meV was identified to be in resonance with the intersubband energy. Under optimized experimental conditions, the PL quenching was studied dependent on polarization direction and mid-infrared fluence at 172 meV photon energy. In a comparative manner, the relative PL quenching is studied

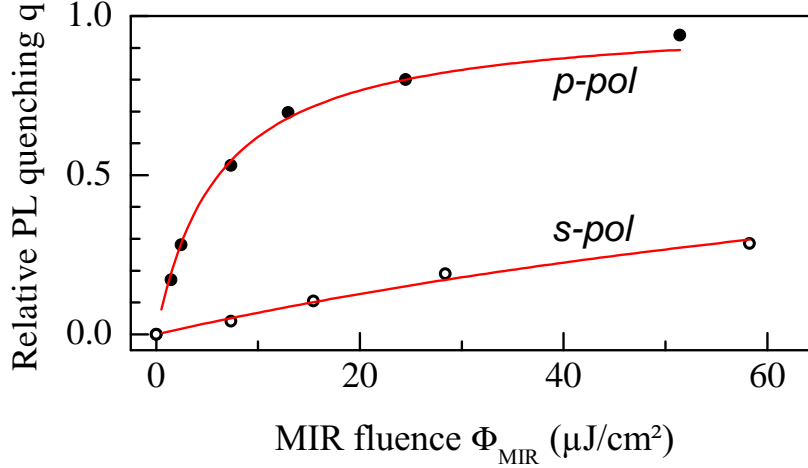


Figure 4.10: Saturation behavior of the relative PL quenching q as a function of mid-infrared fluence for p-polarized (bullets) and s-polarized (circles) mid-infrared pulses. The red lines are the data fitting curves using Equation (4.14).

under mid-infrared irradiation for s- and p-polarized light. In both cases, the relative dip depth increases linearly and saturates towards $q = 1$, i.e., the depletion of the lower level is complete. In Figure 4.10, the saturation behavior of the relative quenching q with increasing MIR fluence Φ_{MIR} is fitted with the general equation

$$q(\Phi_{\text{MIR}}) = \left(1 + \frac{\Phi_{\text{sat}}}{\Phi_{\text{MIR}}}\right)^{-1}, \quad (4.14)$$

where Φ_{sat} is the saturation fluence. As a result, the saturation fluence is $6 \mu\text{J cm}^{-2}$ for p-polarized light while the induced quenching for s-polarized light saturates at $\Phi_{\text{sat}} = 140 \mu\text{J cm}^{-2}$. For pulse widths of 1.6 ps and reflectivity losses at the sample surface of 22% for p-polarized light, the calculated saturation intensity is 3 MW cm^{-2} . Analogously, for s-polarized light, we have 36% reflectivity losses and 56 MW cm^{-2} saturation intensity. From geometric considerations, it is found that only 30% of the incoming p-polarized light intensity has an electric field component perpendicular to the quantum well layer plane. The resulting saturation intensity of 1 MW cm^{-2} agrees well with earlier results for GaAs/AlGaAs quantum wells [Liu88].

4.5 Summary and outlook

In this study of intersubband transitions, we observed the induced PL dynamics as a function of temperature, mid-infrared photon energy, and mid-infrared fluence. The induced population transfer reflects itself in the dip depth and strongly depends on the polarization direction of the mid-infrared beam. This characteristic has been proven to be a valuable tool for accurate monitoring and controlling the timing of infrared and terahertz radiation pulses from accelerator based sources with respect to near-infrared pulses from table-top sources. Several two-color experiments at FELBE benefit from this technique for finding the required temporal overlap, e.g., THz-sideband generation [Wag09b]. For all measurements, the recovery time after the quench has the same values as the PL rise time. Furthermore, we could not find any second time constant in the PL transients as an indication for possible exciton formation processes after optical excitation. According to previous discussion about the exciton formation time, it can be concluded that the observed PL recovery after the quench can be traced back to phonon-assisted cooling of the hot excitons rather than exciton formation. The rise time of the PL transient is associated with the cooling time of dark excitons relaxing back to bright states.

As no PL signal is detected from the excited carriers in the upper level of the conduction band, we propose future studies on the intersubband relaxation dynamics of step quantum wells, see e.g., [Yuh89], or of non-uniformly doped wells. The generated asymmetric band structure changes the parity selection rules and optically bright states get populated after resonant intersubband excitation [Mii90]. From the analysis of the excited PL signal, direct insight into the intersubband relaxation dynamics and recombination processes is expected.

5 Photoluminescence dynamics under pulsed intraexcitonic excitation

In this Chapter, the technique of time-resolved PL spectroscopy is combined with THz pulses that have a photon energy resonant to the $1s$ -to- $2p$ intraexcitonic transition. In the experiment, efficient population transfer between the optically generated excitonic $1s$ state and higher-lying excitonic states is monitored. In the PL spectra, the THz induced carrier redistribution is visible as transient quenching of the $1s$ PL signal and the simultaneous appearance of a $2s$ PL signal. This pronounced effective $1s$ -to- $2s$ transition is surprising, since the THz excitation of the $2s$ state is dipole-forbidden.

In the first part of this chapter, the experimental results on sample DBR42 are shown, that represent the first observation of $2s$ PL excess emission under resonant THz excitation. The effect is explained as efficient Coulomb-scattering mediated mixing of the excitonic $2s$ and $2p$ states which goes along with the THz induced $1s$ -to- $2p$ transition. The theoretical calculations for this specific many-body semiconductor configuration performed by our collaborators Koch et. al correctly predict the appearance of the $2s$ PL.

In a second part of this chapter, the different dynamics of the $1s$ PL quenching and the $2s$ PL signal is investigated on sample H063. In order to analyze the time-resolved PL spectra during the THz induced $1s$ -to- $2p$ transition, a rate equation model is introduced. It describes both, the $1s$ PL quenching and the $2s$ PL dynamics, using a fourth effective level that acts as a reservoir for the dark excitons which do not contribute to the PL emission.

Parts of this chapter have been published previously in [Ric13a, Zyb14].

5.1 Resonant THz spectroscopy

The THz experiment is based on the ideas of the transient PL quenching induced by mid-infrared pulses that was described in Chapter 4. After optical excitation, the transient PL signal is monitored with the streak camera setup that is explained in Chapter 3. Through the combination with temporally delayed THz pulses, the intraexcitonic $1s$ -to- $2p$ population transfer is visible as transient quenching of the $1s$ PL signal.

Already in 1992, the group of M. Sherwin [Qui92] suggested THz experiments which might show significant PL quenching under resonant intraexcitonic excitation. In our experiment, the near-infrared and the THz laser beams illuminate the quantum well close to normal incidence with a temporal delay Δt between the pulses, see Figure 5.1(a). As a prerequisite for PL emission, near-infrared laser pulses populate the conduction band either resonantly or nonresonantly. The latter case involves phonon-assisted scattering towards low momentum states. The corresponding in-plane dispersion of the involved states and possible THz excitations are schematically shown in Figure 5.1(b). Colored arrows indicate the near-infrared induced transition into the electron-hole continuum and the THz-induced $1s$ -to- $2p$ transition. The $2s$ and the $2p$ excitonic states are nearly degenerated. For all experiments, the delayed THz pulse is tuned to resonance with the intraexcitonic transition energy.

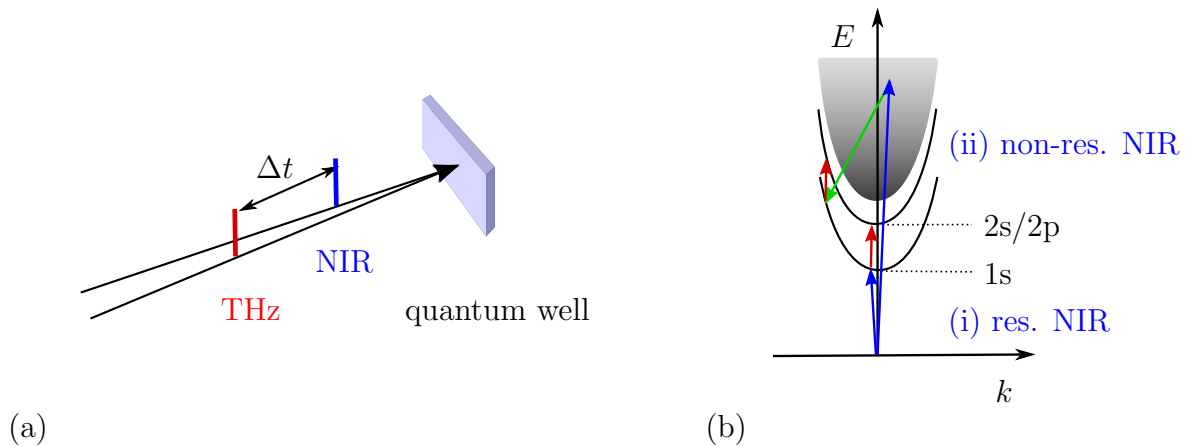


Figure 5.1: Schemes of the intraexcitonic transition studies. (a) Temporal delay Δt between the two exciting pulses that illuminate the sample under an angle close to normal incidence. (b) In-plane dispersion of the involved excitonic states and electron-hole continuum (shaded area). The arrows indicate the induced transitions by near-infrared (blue) and resonant THz (red) pulses. The green arrow represents phonon scattering after non-resonant near-infrared excitation. The figure is adapted from [Kai03].

5.2 Observation of dipole-forbidden exciton transitions

The two-color PL quenching experiment was performed on the InGaAs/GaAs quantum well sample DBR42, for details see Chapter 3. The sample was mounted in an optical cryostat as shown in the schemes of the experimental setup, see Figure 3.2, and kept at a lattice temperature of 10 K. Carriers are excited into the $1s$ (hh) state with near-infrared Ti:Sapph laser pulses of 4 ps length and a resonant photon energy of 1.471 eV. For this particular sample, the required photon energy for the $1s$ -to- $2p$ transition is 6.9 meV

[Ric13a]. The THz pulses from the free-electron laser source have 30 ps duration time for this photon energy. For the experimental setup, the free-electron laser and Ti:Sapph laser spot sizes are approximately $300 \mu\text{m}$ and $50 \mu\text{m}$, respectively. The actual values are estimated using the Spiricon Pyrocam. The excitation density was in the regime below the Mott transition such that the PL emission is dominated by excitons.

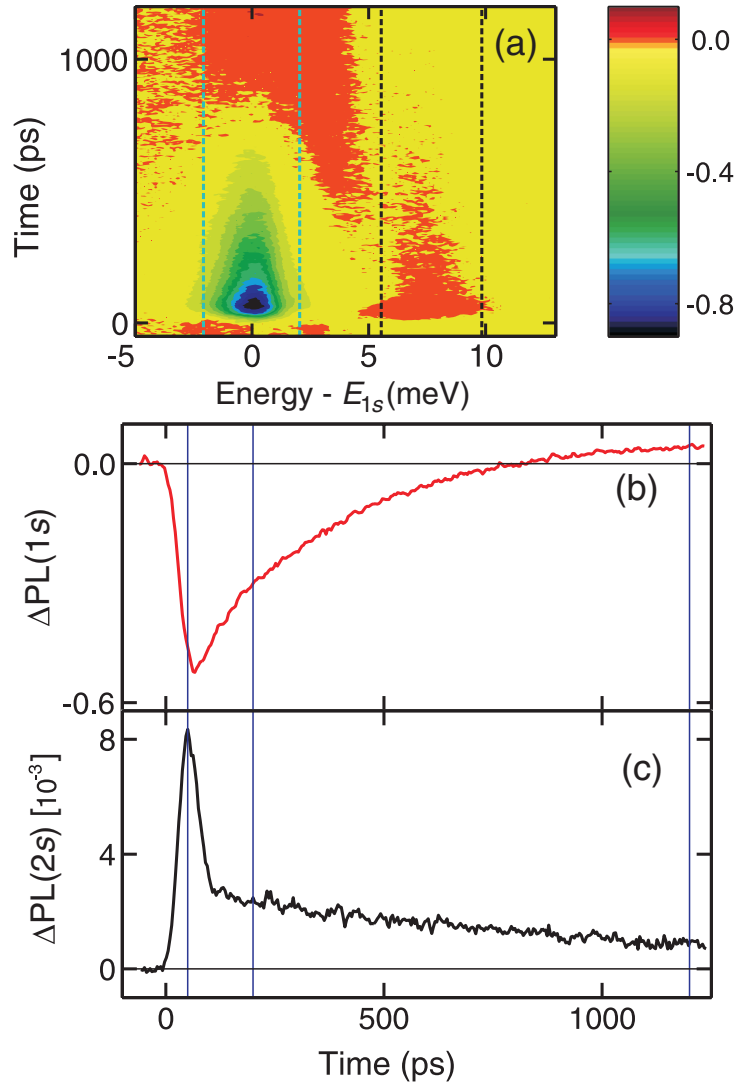


Figure 5.2: THz-induced changes of transient PL emission. (a) Measured PL spectrum in a differential form, for which the reference streak image is subtracted from the measurements taken under resonant THz excitation. The vertical dashed lines mark the integration areas used to create the PL transients (b) $\Delta\text{PL}(1s)$ and (c) $\Delta\text{PL}(2s)$. This Figure has been published in [Ric13a], copyright (2013) by The American Physical Society.

After optical excitation into the conduction band, the excitonic $1s$ PL emission peak is detected at an energy E_{1s} of 1.471 eV. Under resonant THz excitation, an efficient carrier transfer is observed which leads to a transient quenching of the $1s$ PL signal. However,

the most noticeable phenomena for this experiment is the appearance of a simultaneous 2s PL excess signal which is separated from the 1s PL signal by the THz photon energy of 6.9 meV. It emerges at the arrival time t_{THz} of the THz pulse about 195 ps after the optical pulse and decays shortly afterwards. Figure 5.2(a) is a contour plot of exemplary PL data in a differential form, where the reference streak image is subtracted from the measurement taken under resonant THz excitation. In this Figure, the arrival time of the THz pulse defines time zero, and the energy scale is given in $E-E_{1s}$. The negative differential signal $\Delta\text{PL}(1s)$ is plotted in false colors. According to the color bar, positive differential signals are marked red, while yellow indicates areas of the streak image that are not influenced by THz excitation. Vertical dashed lines in Figure 5.2(a) mark 5 meV wide integration areas of $\Delta\text{PL}(1s)$ and $\Delta\text{PL}(2s)$ which are symmetric to the 1s PL and the 2s PL emission energy. Within this energy range, the initial 1s PL quenching, the PL recovery, and the PL overshoot for later times are clearly visible. The detected $\Delta\text{PL}(2s)$ signal has positive values in a spectral range between 5 meV and 10 meV. The integrated 1s PL and 2s PL transients are plotted in Figures 5.2(b) and 5.2(c). Both, the THz-induced 1s quench and the 2s PL excess emission occur within about 50 ps after the arrival time of the THz pulse. After reaching the minimum, $\Delta\text{PL}(1s)$ slowly recovers and overshoots the initial value from $t = 800$ ps on. The 1s PL signal is enhanced long after the arrival time of the THz pulse compared with the unperturbed PL transient. More precisely, during THz excitation, exciton population is transferred into optically dark states which do not contribute to PL emission. As the non-radiative recombination rate is negligible small, the excited excitons relax back into the radiative 1s state and emit PL delayed in time [Ric13a]. It has been verified by time-integrated measurements that the excess signal for later times perfectly compensates for the quenched intensity. The pronounced 2s PL enhancement $\Delta\text{PL}(2s)$ decreases faster than $\Delta\text{PL}(1s)$ recovers and is followed by a slow decaying signal. As can be seen from the PL transients in Figures 5.2(b) and 5.2(c), the 2s PL emission and the 1s PL quench are simultaneous effects. Thus, beside the sequential picture with fast $2p$ -to- $2s$ scattering, THz induced "direct" 1s-to-2s transition can be concluded [Ric13a].

5.3 Coulomb-induced state mixing

In this Section, the PL data are compared with theoretical results based on a microscopic many-body theory which has been developed by Koch et al., see [Kir04], [Koc06], [Ric13a], and Supplemental Material [Ric13b]. Following these references, the excitonic system is a strongly Coulomb-interacting many-body system resulting in a mixed $2s/2p$ state, where Coulomb-assisted THz transitions directly convert 1s excitons into 2s population. The

experimentally observed 2s PL phenomenon is mediated by diffusive Coulomb scattering between the almost degenerated 2s and 2p excitonic state during resonant 1s-to-2p THz excitation.

The microscopic approach includes Coulomb scattering, radiative decay, momentum relaxation, and phonon relaxation among exciton states, where the excitons are defined by two-particle correlations

$$c_X^{\mathbf{q},\mathbf{k}',\mathbf{k}} \equiv \Delta \left\langle e_{\mathbf{k}}^\dagger h_{\mathbf{k}-\mathbf{q}}^\dagger h_{\mathbf{k}'} e_{\mathbf{k}'+\mathbf{q}} \right\rangle \quad (5.1)$$

between the electron $e^\dagger e$ and hole $h^\dagger h$ operators [Ric13a] with carrier momentum \mathbf{k} and photon momentum \mathbf{q} . Here, the special case is considered where the incoming excitons scatter into new momentum states with the constraint that the number of incoming and outgoing two-particle correlations remain constant. The exciton correlation is created in the state $c_X^{\mathbf{q},\mathbf{k}',\mathbf{k}}$ by THz transitions and can scatter to a new state such as $c_X^{\mathbf{q},\mathbf{k}'+\mathbf{K},\mathbf{k}}$ or $c_X^{\mathbf{q},\mathbf{k}',\mathbf{k}+\mathbf{K}}$, where the scattering wave vector \mathbf{K} has a constant magnitude. The influence of the diffusive Coulomb scattering among excitons on the THz-induced exciton transitions is expressed with the ansatz

$$T_{\text{diff}}^{\mathbf{q},\mathbf{k}',\mathbf{k}} = -i\hbar\gamma \left(c_X^{\mathbf{q},\mathbf{k}',\mathbf{k}} - \frac{1}{2\pi} \int_0^{2\pi} d\theta_{\mathbf{K}} c_X^{\mathbf{q},\mathbf{k}'+\mathbf{K},\mathbf{k}+\mathbf{K}} \right) , \quad (5.2)$$

see [Ric13a], where $\theta_{\mathbf{K}}$ is the direction of the scattering wave vector \mathbf{K} and γ defines the overall scattering strength. The 2p and 2s state mixing holds as long as \mathbf{K} is not zero.

For the diffusive model, calculations are restricted to the population of the 1s, 2p, and 2s state that reduces $T_{\text{diff}}^{\mathbf{q},\mathbf{k}',\mathbf{k}}$ (5.2) to a 3×3 matrix T_X . Due to the 2s/2p state mixing, the decay rate of the THz induced 2s population is

$$\tau_{2s}^{-1} = \tau_{\text{rel}}^{-1} - \tau_{\text{conv}}^{-1} , \quad (5.3)$$

where r_{conv} is the 2p-to-2s conversion rate. The corresponding matrix elements are $T_{2p,2s} = r_{\text{conv}}$ and $T_{2s,2p} = -r_{\text{conv}}$. The relaxation rates $r_{2p,2p}$ and $r_{2s,2s}$ of the 2p and the 2s level towards quasiequilibrium are assumed to be equal, $r_{2p,2p} = r_{2s,2s} = -r_{\text{rel}}$. The relaxation rate $r_{1s,1s}$ is set to zero as well as all the other $r_{\lambda,1s}$ elements, resulting in

$$T_X = \begin{pmatrix} 0 & -r_{\text{rel}} - r_{\text{conv}} & -r_{\text{rel}} - r_{\text{conv}} \\ 0 & -r_{\text{rel}} & r_{\text{conv}} \\ 0 & r_{\text{conv}} & -r_{\text{rel}} \end{pmatrix} , \quad (5.4)$$

where the first, second, and third row correspond to the 1s, 2p, and 2s states, respectively.

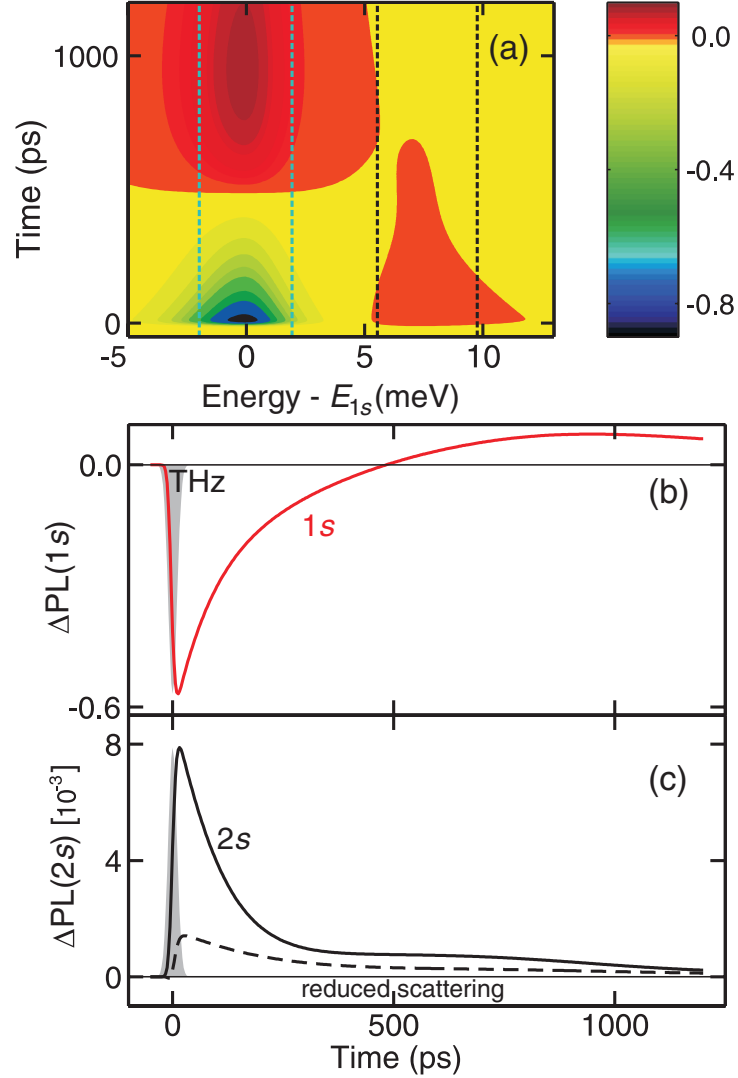


Figure 5.3: (a) Computed differential PL. Integrated differential $\Delta PL_\lambda(t)$ for (b) $\lambda = 1s$ and (c) $\lambda = 2s$ THz-induced effect on PL. The chosen parameters for the calculation are $\tau_{\text{phon}} = 900$ ps, $\tau_{2s} = 120$ ps, $\tau_{\text{conv}} = 56$ ps, $\tau_{\text{rel}} = 38.2$ ps. The gray shaded areas mark the THz pulse and the dashed curves show the $2s$ signal calculated with reduced scattering. This figure has been published in [Ric13a], copyright (2013) by The American Physical Society.

In Figure 5.3(a), a numerical solution of the THz dynamics $\frac{\partial}{\partial t} c_X^{\mathbf{q}, \mathbf{k}', \mathbf{k}}$ is shown, where all relevant optically bright states, the dark excitonic states, and the diffusive Coulomb scattering given in Equation (5.2) are considered. The chosen parameters for the calculation are $\tau_{2s} = 120$ ps, $\tau_{\text{conv}} = 56$ ps, and $\tau_{\text{rel}} = 38.2$ ps. Analogously to the experimental data shown in Figure 5.2(a), dotted lines indicate the 5 meV wide energy range around the 1s PL and the 2s PL differential signals. The modeled PL transients $\Delta\text{PL}(1s)$ and $\Delta\text{PL}(2s)$ are shown in Figures 5.3(b) and 5.3(c), respectively. The measured PL transients are qualitatively reproduced including the 1s PL quenching, the PL recovery, and the 1s PL overshoot. The $\Delta\text{PL}(2s)$ signal features a very fast and a slow decaying component, where the latter is connected to phonon relaxation with time constant $\tau_{\text{phon}} = 900$ ps. The dashed curve in Figure 5.3(c) is produced by an additional computation with reduced scattering. Instead of the pronounced peak, only a very weak $\Delta\text{PL}(2s)$ signal emerges due to thermal relaxation from ionized excitons during the THz excitation [Ric13a]. This behavior emphasizes the significance of Coulomb-assisted THz transition including the dipole-forbidden conversion of a 1s into a 2s population [Ric13a], where the Coulomb scattering is much faster than the relevant relaxation processes. Note that the final matrix T_X (5.4) is of importance in later discussions in Section 5.4.1 where the exciton populations are modeled based on a rate equation system.

5.4 Characterizing intra-exciton Coulomb scattering in THz excitations

The experiment-theory analysis on sample DBR42, that is presented in the previous Sections 5.2 and 5.3, shows that the THz induced intra-exciton transitions can be characterized in terms of Coulomb scattering mechanisms. However, the model does not differentiate between the experimentally observed fast decaying 2s signal and the slow 1s PL recovery. The deduced matrix T_X , see Equation (5.4), implies that the processes of 2s PL decay and 1s PL recovery occur with identical time constants. In the present Section, different relaxation channels are identified that contribute to the slow 1s PL recovery and the fast decay of the 2s state. For this purpose, time-resolved PL measurements are performed on the GaAs/AlGaAs quantum well sample H063. The PL transients are evaluated using a newly created fit function, and the parameters of the 2s PL dynamics are compared with that of the 1s PL quenching.

The unperturbed PL emission of the sample H063 has been characterized in Chapter 3. The required THz photon energy for the intraexcitonic 1s-to-2p transition of 8.7 meV is well known from earlier studies on this specific sample [Wag09b, Wag10]. The sample was installed in an optical cryostat and kept at a lattice temperature of 6 K. Non-resonant

near-infrared laser pulses excite carriers at intermediate densities of about $4 \times 10^{10} \text{ cm}^{-2}$ in the sample. Non-resonant band-to-band excitation initially creates a strong exciton population of the high momentum $1sk$ states that do not contribute to the PL emission signal. The advantage of the energy offset between the $1s$ PL emission and the exciting laser pulse is that the laser stray light is outside the detected spectral range of the streak image.

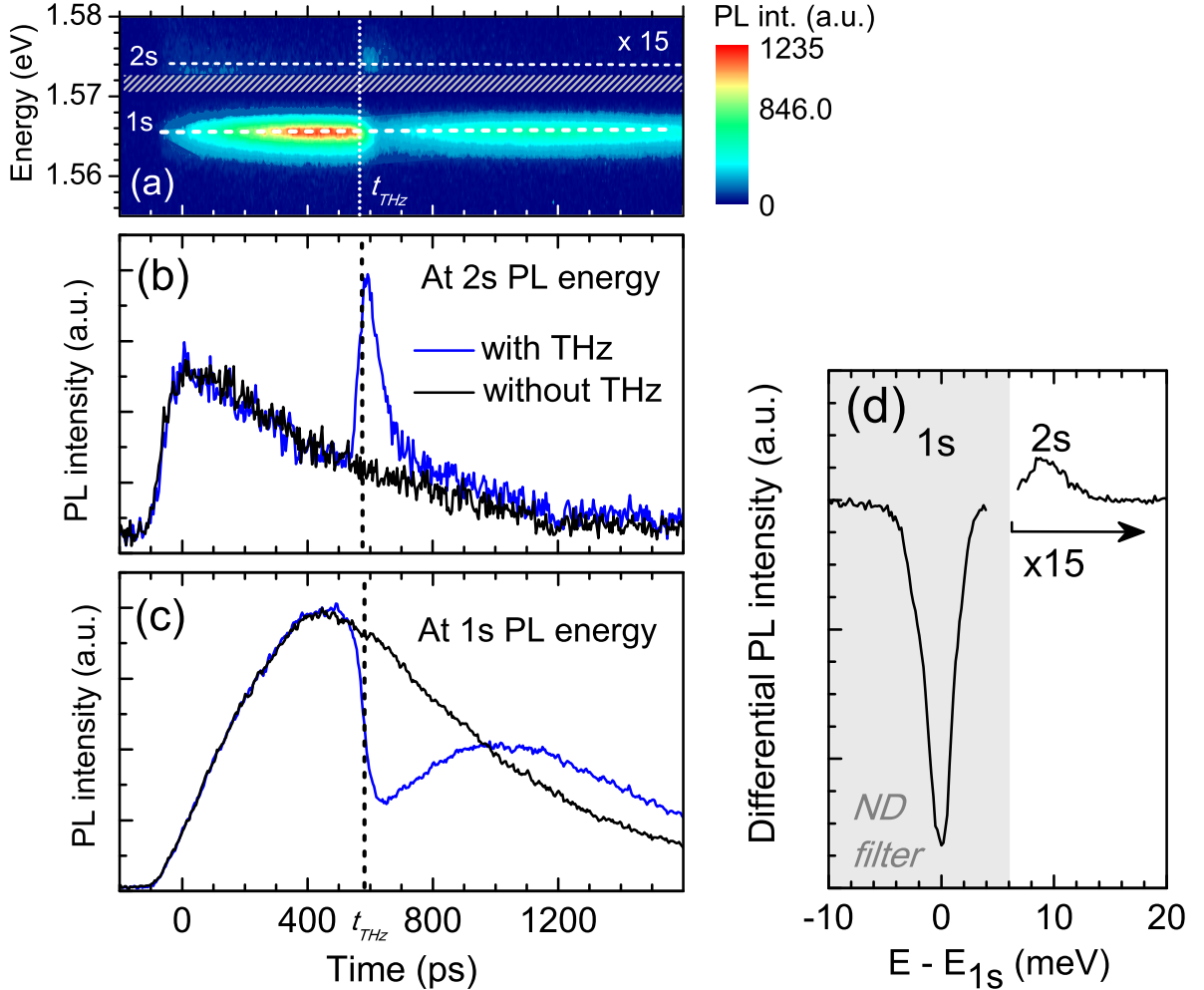


Figure 5.4: (a) Streak image of the time-resolved PL under THz irradiation. The colors indicate the PL intensity. Transient $2s$ PL (b) and $1s$ PL (c) for 8.7 meV THz photon energy excited with 28 nJ cm^{-2} (shaded area) and reference trace (black line). (d) Differential PL spectrum at the arrival time t_{THz} of the THz pulse (dotted vertical line in (a) – (c)) showing the THz induced $1s$ PL quenching and the $2s$ PL emission. Note the different scaling of the PL intensity as the $1s$ PL emission has been attenuated during measurements using a neutral density filter.

About 600 ps after the near-infrared band-to-band excitation, resonant THz pulses induce an efficient carrier transfer to the $2p$ level and $1s$ high momentum states. At the arrival time t_{THz} of the THz pulse, the induced population transfer manifests itself in an

abrupt decrease of the $1s$ PL emission signal. During the THz excitation and shortly afterwards, the PL spectrum features a pronounced peak at the $2s$ energy E_{2s} corresponding to the $2s$ PL emission. The effect is illustrated in Figure 5.4(d) where the differential PL spectrum shows negative values at E_{1s} of 1.564 eV and $2s$ PL excess at $E_{1s} + 8.7 \text{ meV} = 1.573 \text{ eV}$. The detected $2s$ PL intensity is about two orders of magnitude smaller than that of the $1s$ PL. The difference between the detected signal strengths is attributed to the oscillator strength of the $2s$ recombination which is about eight times smaller than that of the $1s$ recombination [Tan95]. Furthermore, Drude-type absorption of the THz pulse enables free-carrier transfer from radiative states to high-momentum states within the same subband. A direct observation of the strong $1s$ PL and the weak $2s$ PL signals is limited by the dynamic range of the streak camera. To overcome this problem, a neutral density filter was placed behind the spectrometer in such a way that the lower-energy part of the spectrum is attenuated by a factor of 15. Note the filter edge around 5 meV above E_{1s} in Figure 5.4(a) and 5.4(d).

For evaluation of the PL transients, horizontal profiles are taken at the $1s$ and $2s$ energies with $\pm 2 \text{ meV}$ integration width corresponding to the line width of the sample. The observed changes in the PL signal are interpreted as the THz-induced dynamics of the exciton population. In Figures 5.4(b) and (c), the PL transients with and without THz excitation are compared. The $1s$ PL signal recovers to an intensity higher than that of the reference trace which compensates for the PL quenching due to the induced carrier transfer to high momentum states. As has been found for the sample DBR42 in Section 5.2, the $2s$ PL signal decays much faster than the $1s$ PL signal recovers. From this, we conclude that there is a negligible direct channel between the excitonic $2s$ state and the bright $1s$ state.

5.4.1 Rate-equation model for intraexcitonic transition

For the theoretical treatment which was introduced in Section 5.3, it is assumed that the populations of the $2s$ and the $2p$ levels directly relax back into the $1s$ state. However, the dynamics of the measured signals has been proven to be dominated by a high momentum exciton population causing a fast decaying $2s$ PL signal compared to the THz induced $1s$ PL quench. In the following, we focus on the decay of the detected $2s$ PL signal and the associated relaxation back into the $1s$ state. For this purpose, the microscopic model published in [Ric13a] is broken down and transferred into a rate equation model for bright and dark exciton densities. This reduces the computational effort, and furthermore, this enables the identification of physically relevant process rates from the experimental data. A rate equation model is introduced which is similar to the model for pulsed intersubband excitation deduced in Section 4.2. While two effective states were considered for the

intersubband model, four effective states are admissible now. The present approach takes into account scattering from $2s$ and $2p$ into high-momentum excitons of the $1s$ exciton manifold. This dark excitons outside the light cone are denoted by $1sk$, where k is the center-of-gravity momentum of the exciton.

In Figure 5.5(a), the THz induced processes are shown schematically. After THz excitation, excitons are Coulomb scattered to the $2s$ level that radiatively decays. The four effective levels and the considered relaxation processes are shown as lines and with arrows in Figure 5.5(b), respectively. The population of the $2s$ and the $2p$ level relax non-radiatively with time constant τ_{rel} to the non-radiative state $1sk$. From this high momentum state, the carriers further relax with time constant τ_k towards the radiative state $1s$, i.e., the electron-phonon scattering is incorporated as one phenomenological time constant. The radiative recombination is measurable as the emitted PL signal with a decay time of τ_{PL} .

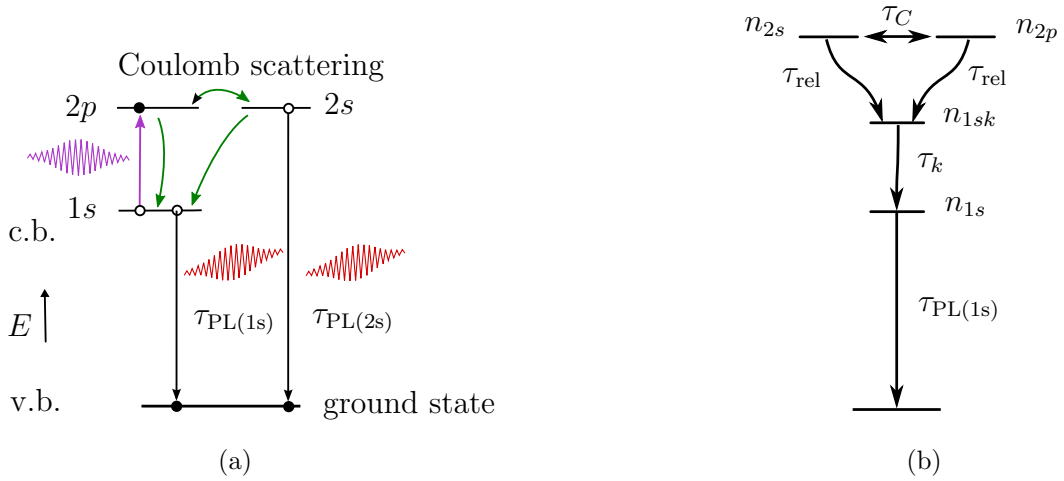


Figure 5.5: (a) The excitonic levels at the arrival time of the THz pulse. The THz excitation is shown in violet, the relaxation processes in green, and the PL recombination in black, respectively. (b) Flow diagram of the model with occupation numbers of the degenerated levels n_{2s} and n_{2p} , of the non-radiative level n_{1sk} , of the radiative level n_{1s} , and the ground state. The arrows indicate the Coulomb scattering τ_C and the relaxation between the effective states with time constants τ_{rel} , τ_k , and τ_{PL} , respectively.

The rate equations form a linear system of ordinary differential equations of first order. This system can be solved analytically, where the solutions are adapted to the adjusted initial conditions corresponding to the different oscillator strengths and the Drude-type $1s$ -to- $1sk$ absorption process. The introduced constants C_{1s} and C_{2s} scale the amplitude of the modeled curves to the measured PL intensities. The detected PL intensities differ by a factor of 30, where the excitonic free-carrier heating is formally identified as the

dominating process. A substantial reason for the dominance of excitonic free-carrier heating is the fact that for higher THz fluences the relative quenching saturates with $q = 1$ which means full depletion of the radiative $1s$ state. This heating cannot be explained by a pure excitonic $1s$ -to- $2p$ interlevel transition. As the fraction of carriers that gets excited into the $2p$ level is small, the $1s$ PL dynamics is not influenced by the relaxation of $2p$ and $2s$ towards $1sk$. The recovery of the $1s$ PL signal after the THz excitation is exclusively described by the momentum relaxation τ_k between the effective $1sk$ and $1s$ level in our model.

The introduced optically bright levels $1s$, $2s$, and $2p$ are simplified states representing thermalized exciton distributions close to equilibrium with the lattice. The $1sk$ state corresponds to a carrier distribution that is optically dark. Note that the real momentum distribution determining the PL dynamics is not described by this four-level model. During resonant $1s$ -to- $2p$ excitation, population is transferred from the $1s$ into the $2p$ level. Subsequently, excitons populate the $2s$ level mediated by efficient Coulomb-scattering. This leads to an instantaneous population of the $2p$ level while the rising edge of $2s$ signal depends on the Coulomb scattering time τ_C . Both signals decay with a time constant τ_{rel} that represents the nonradiative decay into high-momentum states $1sk$.

The transient population of the $2p$ states depends on the diffusive Coulomb scattering time τ_C and the relaxation to the optically dark state $1sk$ with time constant τ_{rel} . The $2s$ state has the same two relaxation channels τ_C and τ_{rel} while being radiative. The intraband relaxation time τ_k of high-momentum states into the optically active $1s$ state dominates the PL rise time. Note that the experimentally observed $2s$ PL decay time includes also non-radiative processes. The radiative $2s$ recombination $\tau_{\text{PL}(2s)}$ is much slower than the non-radiative carrier relaxation to the $1sk$ state, τ_{rel} , and will not be taken into consideration. From the four-level model, a system of rate equations is developed analogously to that of the intersubband experiments in Chapter 4. The solutions describe the transient PL signal under resonant THz excitation.

The rate equations can be written in the form

$$\frac{d}{dt} \begin{pmatrix} n_{2s}(t) \\ n_{2p}(t) \\ n_{1sk}(t) \\ n_{1s}(t) \end{pmatrix} = T' \begin{pmatrix} n_{2s}(t) \\ n_{2p}(t) \\ n_{1sk}(t) \\ n_{1s}(t) \end{pmatrix}, \quad (5.5)$$

where T' is a 4×4 -matrix. The functions $n_{2s}(t)$, $n_{2p}(t)$, $n_{1sk}(t)$, and $n_{1s}(t)$ are the occupation number of the states $2s$, $2p$, $1sk$, and $1s$, respectively. The system of 1st order ordinary differential equations (5.5) simplifies considerably if the scattering rate τ_s from the radiative $1s$ state to high momentum states $1sk$ is neglected. In order to keep the

system as simple as possible, the admissible population transfer $1sk$ -to- $2pk$ between high momentum states is not considered. Based on these assumptions, the matrix T' in Equation (5.5) takes the form

$$T' = \begin{pmatrix} -\tau_{\text{rel}}^{-1} - \tau_{\text{C}}^{-1} & \tau_{\text{C}}^{-1} & 0 & 0 \\ \tau_{\text{C}}^{-1} & -\tau_{\text{rel}}^{-1} - \tau_{\text{C}}^{-1} & 0 & 0 \\ \tau_{\text{rel}}^{-1} & \tau_{\text{rel}}^{-1} & -\tau_{\text{k}}^{-1} & 0 \\ 0 & 0 & \tau_{\text{k}}^{-1} & -\tau_{\text{PL}}^{-1} \end{pmatrix}, \quad (5.6)$$

that is comparable to T_X given in Equation (5.4) extended by a fourth effective state $1sk$. Under THz excitation, the set of coupled rate equations is solved with initial conditions adjusted to the problem. The fraction of carriers that is transferred by the THz pulse to the $2p$ level to $q_{2p} = 0.1q$ is chosen arbitrarily, where q is the percentage of excited carriers. Anyway, the exact value is not relevant as the measured $2s$ PL signal strength is scaled independently of the $1s$ PL intensity. The factor q_{2p} should be small enough such that the relaxation of the $2p$ and $2s$ population does not influence the $1sk$ momentum relaxation τ_k . Under this restriction, the initial conditions are

$$n_{2s}^{\text{II}}(t_{\text{THz}}) = 0 \quad (5.7)$$

$$n_{2p}^{\text{II}}(t_{\text{THz}}) = b q q_{2p} \quad (5.8)$$

$$n_{1sk}^{\text{II}}(t_{\text{THz}}) = a + b q (1 - q_{2p}) \quad (5.9)$$

$$n_{1s}^{\text{II}}(t_{\text{THz}}) = b (1 - q) \quad , \quad (5.10)$$

where $a = n_{1sk}^{\text{I}}(t_{\text{THz}}) = e^{-\frac{t_{\text{THz}}}{\tau_{\text{C}}}}$ and $b = n_{1s}^{\text{I}}(t_{\text{THz}}) = \frac{\tau_{\text{PL}}}{\tau_{\text{PL}} - \tau_{\text{C}}} (e^{-\frac{t_{\text{THz}}}{\tau_{\text{PL}}}} - e^{-\frac{t_{\text{THz}}}{\tau_{\text{C}}}})$ are the occupation numbers of the non-radiative and the radiative level of the unperturbed system at time t_{THz} . Notice that the initial condition for n_{2s} (5.7) reflects that there is no direct carrier transfer into $2s$ by the THz excitation. The coupled rate equations (5.6) can be solved analytically with the solution

$$n_{2s}^{\text{II}}(t) = \frac{b q q_{2p}}{2} e^{-\frac{t-t_{\text{THz}}}{\tau_{\text{rel}}}} \left(1 - e^{-\frac{2(t-t_{\text{THz}})}{\tau_{\text{C}}}} \right), \quad (5.11)$$

$$n_{2p}^{\text{II}}(t) = \frac{b q q_{2p}}{2} e^{-\frac{t-t_{\text{THz}}}{\tau_{\text{rel}}}} \left(1 + e^{-\frac{2(t-t_{\text{THz}})}{\tau_{\text{C}}}} \right), \quad (5.12)$$

$$n_{1sk}^{\text{II}}(t) = \frac{1}{\tau_{\text{k}} - \tau_{\text{rel}}} e^{-t\left(\frac{1}{\tau_{\text{k}}} + \frac{1}{\tau_{\text{rel}}}\right)} \left((a(\tau_{\text{k}} - \tau_{\text{rel}}) + b q (\tau_{\text{k}} - (1 - q_{2p})\tau_{\text{rel}})) e^{\frac{t}{\tau_{\text{rel}}} + \frac{t_{\text{THz}}}{\tau_{\text{k}}}} - b q q_{2p} \tau_{\text{k}} e^{\frac{t}{\tau_{\text{k}}} + \frac{t_{\text{THz}}}{\tau_{\text{rel}}}} \right), \quad (5.13)$$

$$\begin{aligned}
n_{1s}^{\text{II}}(t) = & \frac{b q q_{2p} \tau_{\text{PL}} \tau_{\text{rel}}}{(\tau_{\text{rel}} - \tau_{\text{k}})(\tau_{\text{rel}} - \tau_{\text{PL}})} e^{-\frac{t-t_{\text{THz}}}{\tau_{\text{rel}}}} \\
& + \frac{\tau_{\text{PL}} (a(\tau_{\text{k}} - \tau_{\text{rel}}) + b q (\tau_{\text{k}} - (1 - q_{2p}) \tau_{\text{rel}}))}{(\tau_{\text{k}} - \tau_{\text{PL}})(\tau_{\text{k}} - \tau_{\text{rel}})} e^{-\frac{t-t_{\text{THz}}}{\tau_{\text{k}}}} \\
& + \frac{a \tau_{\text{PL}} (\tau_{\text{PL}} - \tau_{\text{rel}}) - b ((1 - q) \tau_{\text{k}} (\tau_{\text{PL}} - \tau_{\text{rel}}) - \tau_{\text{PL}} (\tau_{\text{PL}} - (1 - q q_{2p}) \tau_{\text{rel}}))}{(\tau_{\text{PL}} - \tau_{\text{k}})(\tau_{\text{PL}} - \tau_{\text{rel}})} e^{-\frac{t-t_{\text{THz}}}{\tau_{\text{PL}}}}.
\end{aligned} \tag{5.14}$$

For the particular case $q = 0$, the above solutions can be rewritten as

$$n_{2s}(t) = 0, \quad n_{2p}(t) = 0, \quad n_{1sk}(t) = e^{-\frac{t}{\tau_{\text{k}}}}, \quad n_{1s}(t) = \frac{\tau_{\text{PL}}}{\tau_{\text{PL}} - \tau_{\text{C}}} \left(e^{-\frac{t}{\tau_{\text{PL}}}} - e^{-\frac{t}{\tau_{\text{C}}}} \right),$$

which are equal the functions of the reference traces without a second excitation, see Equations (4.2) and (4.3).

As in Chapter 4, the functions that describe the change of the occupation number for all $t > 0$ are put together from the solutions in region I and II. An example of a set of model curves is plotted in Figure 5.6, where time zero is defined as the arrival time of the near-infrared laser pulse. The dotted lines indicate the THz excitation at t_{THz} . The quenching parameter q is set to 0.75 which means that under THz irradiation 75% of the bright carriers are excited to the $2p$ and the $1sk$ level. In Figure 5.6(a), the $1s$ level occupation numbers are plotted with and without THz irradiation, respectively. At the arrival time of the short THz pulse, the $1s$ signal is instantaneously reduced and recovers to a value higher than the reference trace. The abrupt carrier transfer from the bright $1s$ level to the dark $1sk$ level is shown in Figure 5.6(c). At the arrival time of the THz pulse t_{THz} , the $2p$ level is populated and the carriers are efficiently scattered to the $2s$ level. The modeled level occupation numbers of the $2p$ and $2s$ levels are shown in Figure 5.6(b) and 5.6(d), respectively. While the $2p$ level is instantaneously populated, the $2s$ level occupation solely depends on the scattering time τ_{C} . The difference between the rising edges of the two curves is depicted in Figure 5.7 on a different time scale. The maximum $2s$ level occupation is reached after the arrival time of the THz pulse t_{THz} . Both curves decay with time constant τ_{rel} . In Figure 5.7(b), the THz induced $2s$ PL signal is compared with the corresponding differential $1s$ level occupation number. According to the initial conditions, only 10% of the THz excited carriers are transferred to the $2p$ level while most of the carriers are Drude-like scattered to higher momentum states $1sk$. Thus, the $2s$ signal intensity is relatively small compared to the $1s$ quench, and the $1s$ recovery occurs on a time scale much slower than the decay of the $2s$ signal. In accordance with the presumption of carrier conservation, the blue areas below and above the zero level compensate in Figure 5.7(b).

In analogy to the modeling of intersubband dynamics in Chapter 4, the intensity of the PL signal is assumed to be proportional to the occupation number of the bright states

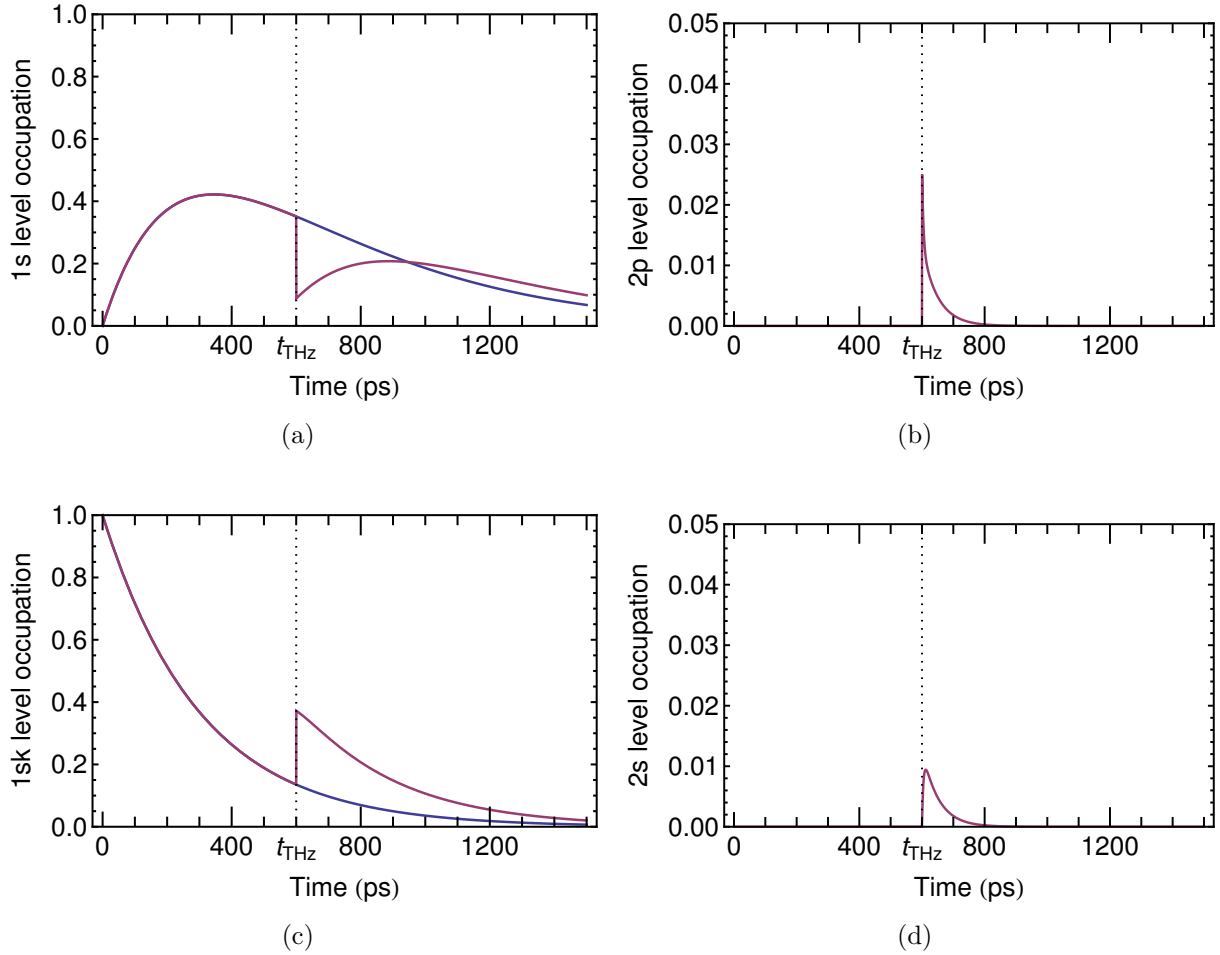


Figure 5.6: Modeled dynamics based on a four-level system after optical excitation at $t_0 = 0$ (blue). The violet curves show the level occupation number with a second excitation at $t = t_{\text{THz}}$ that transfers a fraction q of the population from the radiative effective $1s$ level to the dark $2p$ level. (a) The $1s$ level occupation number $n_{1s}(t)$. (b) The $2p$ level occupation number $n_{2p}(t)$ with THz excitation. (c) The $1sk$ level occupation number $n_{1sk}(t)$. (d) The $2s$ level occupation number $n_{2s}(t)$ with THz excitation. The chosen parameters for the plotted curves are $t_0 = 0$, $t_{\text{THz}} = 600$ ps, $\tau_k = 100$ ps, $\tau_{\text{PL}} = 400$ ps, $q = 0.75$, $q_{2p} = 0.1 q$, $\tau_C = 10$ ps, and $\tau_{\text{rel}} = 50$ ps.

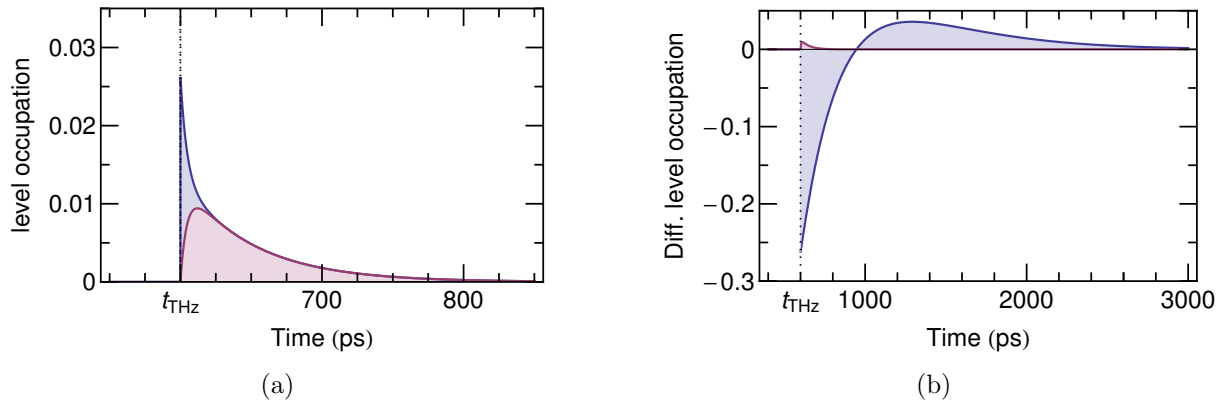


Figure 5.7: (a) Zoom into the $2s$ (red) and the $2p$ (blue) level occupation $n_{2s}(t)$ and $n_{2p}(t)$, respectively. (b) The $2s$ (red) and differential $1s$ (blue) level occupation number calculated from the transient with quench $n_{1s}(t)$ minus the reference trace $n_{1s}^I(t)$ without quenching.

$1s$ and $2s$. The calculated $1s$ -level occupation number $n_{1s}(t)$ and the $2s$ -level occupation number $n_{2s}(t)$ are convoluted with a Gaussian function that accounts for the THz pulse length and the jitter of the synchronization

$$I_{2s\text{PL}}(\sigma, t) = I_0 (n_{2s} * G_\sigma)(t), \quad t > 0, \quad (5.15)$$

$$I_{1s\text{PL}}(\sigma, t) = I_0 (n_{1s} * G_\sigma)(t), \quad t > 0. \quad (5.16)$$

Two fit functions are created, namely *fit-2s* and *fit-1s-dip*, based on the modeled PL signal intensity $I(\sigma, t)$ using Equations (5.15) and (5.16), respectively. With this set of fit functions based on rate equations, THz induced PL dynamics at the $1s$ PL and the $2s$ PL emission energy is evaluated.

5.4.2 PL dynamics at the $1s$ energy and the $2s$ energy

In this section, the PL dynamics at the $1s$ energy and the $2s$ energy is analyzed using the model fit that was developed in the previous section. The relative $1s$ PL quenching and the $2s$ PL emission strength are studied as a function of THz fluence between 0 and 65 nJ cm^{-2} . Particularly, the results taken with THz photon energy of 8.7 meV , that is resonant to the $1s$ -to- $2p$ transition, are compared with the case of slightly off-resonant THz photon energy (10.6 meV). This study indicates how differently the Drude type intraband absorption and the intraexcitonic transition influence the PL dynamics. The experimental details of the PL measurements were given in the first part of Section 5.4.

In order to distinguish between the dynamics of the THz induced $1s$ PL quenching and $2s$ PL emission, two transients of the measured PL signal are evaluated at the $1s$ energy

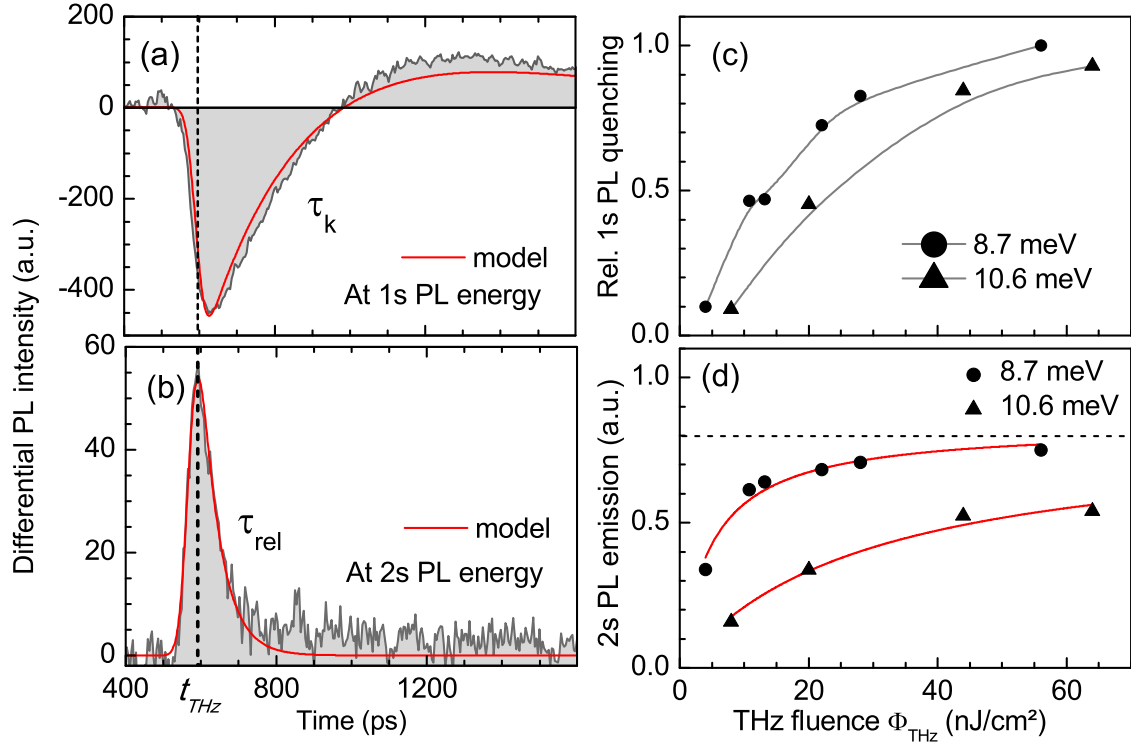


Figure 5.8: Differential plots of the transient PL signals at 1s energy (a) and 2s energy (b) for resonant THz excitation. The red lines are the fits based on the rate equation model *fit-1s-dip* and *fit-2s*, respectively. The PL recovery after the quench is characterized by the PL rise time τ_k . The dynamics of the differential 2s PL signal is determined by the relaxation to the optically dark state $1sk$ with time constant τ_{rel} . The right panels show the relative quenching of the 1s PL intensity (c) and the THz induced 2s PL emission (d) as a function of THz fluence Φ_{THz} for two different THz photon energies 8.7 meV (resonant to $1s$ -to- $2p$ transition, bullets) and 10.6 meV (triangles). The black lines (c) are guides to the eyes and the red lines (d) are saturation fits to the data.

of 1.564 eV and 2s energy of 1.573 eV, respectively. The fit procedure is performed in three steps for each measurement without and with THz excitation. In a first step, the reference 1s PL trace is fit using the function *fit-PL* based on Equation (4.5) in order to extract the PL rise time τ_k , the PL decay time τ_{PL} , the arrival time t_0 of the near-infrared pulse, and the amplitude scaling factor C_{1s} . Second, the 1s PL trace with quench is fit using the function *fit-1s-dip* based on Equation (5.16), where the relative PL quenching q and the arrival time of the THz pulse t_{THz} are the only free parameters. In a last step, the 2s PL transient is evaluated using the function *fit-2s* based on Equation (5.15) with the scaling factor C_{2s} as the only free parameter. For all fits, the Coulomb scattering is set to $\tau_C = 10$ ps which is below the time resolution of our experiment.

The fit functions describe the data quite well with parameters $\tau_k = 390$ ps, $\tau_{\text{rel}} = 40$ ps, and $\tau_C = 10$ ps for all measured fluences. An example is shown in Figure 5.8 where the fits are applied to the 1s PL and the differential 2s PL transients. The differential transients in Figure 5.8(a) and 5.8(b) illustrate the different dynamics in analogy to the plot in Figure 5.7, whereas the PL rise τ_k around t_0 and the PL decay τ_{PL} of the 1s PL transient are not visible. The non-radiative relaxation process between the 2s and 1sk states is found being about ten times faster than the cooling of the 1s high momentum states towards $k = 0$. The scaling parameters C_{1s} and C_{2s} differ by a factor of 30, i.e., only 1/30 of the 1s population which becomes excited by the THz signal can be detected as a bright 2s signal.

Furthermore, it is investigated how the relative quenching q of the 1s PL signal changes as a function of THz fluence Φ_{THz} . The relative quenching parameter q is obtained by the model fit and plotted in Figure 5.8(c). For resonant 1s-to-2p excitation with THz photon energy of 8.7 meV, the amount of quenching strongly increases between 0 and 20 nJ cm⁻² and converges to 1, which corresponds to a 100% depletion of the bright 1s states in the saturation regime. A second set of data has been taken for a THz photon energy of 10.6 meV which is energetically slightly off resonance. For the corresponding data set, the induced quench of the 1s PL transient shows a similar behavior with increasing THz fluence and the fitted time constants are the same as for the resonant case. From this observation, the conclusion is drawn that the 1s dynamics is dominated by the Drude-like excitation process within the 1s level.

Additionally, the change in the THz induced 2s PL is explored relative to the absolute signal intensity measured at the 2s energy including the background. In Figure 5.8(d), the change of the 2s PL signal with increasing THz fluence is plotted. It can be described with a general saturation fit to the measured PL intensity

$$I(\Phi_{\text{THz}}) = I_{\text{sat}} \left(1 + \frac{\Phi_{\text{sat}}}{\Phi_{\text{THz}}} \right)^{-1}, \quad (5.17)$$

where the saturation intensity I_{sat} is indicated by a horizontal dashed line. The results of the fit are $I_{\text{sat}} = 0.84$ and $\Phi_{\text{sat}} = 4.8 \text{ nJ cm}^{-2}$ for the resonant THz photon energy of 8.7 meV. From a comparison of Figure 5.8(c) and 5.8(d), it is obvious that the 2s PL emission reaches its saturation value while the 1s quenching is still in the linear regime. For the data set with detuned photon energy of 10.6 meV, the relative THz induced 2s PL emission converges towards 0.82. However, the saturation fluence of 28.9 nJ cm^{-2} is much higher resulting from weaker THz absorption where less excitons are Coulomb scattered into 2s.

From our rate equation analysis, it can be concluded that scattering into $1sk$, followed by momentum relaxation into radiative 1s excitons with zero momentum, is in fact the dominant relaxation mechanism. As the most prominent signature, the present rate equation correctly reproduces the observed PL dynamics under THz excitation, i.e., a difference of about one order of magnitude between the fast 2s PL decay time and the much slower 1s PL recovery. While the 2s PL signal decays within about 40 ps, the 1s PL recovery time is comparable to the initial PL rise time immediately after non-resonant interband excitation, where similar relaxation of the exciton momentum comes into play.

5.5 Summary and outlook

With time-resolved PL spectroscopy combined with THz pulses resonant to the $1s$ -to- $2p$ intraexcitonic transition, the induced changes of the PL dynamics of GaAs quantum well samples are investigated. The enhancement of the 2s-exciton PL emission was observed when THz pulses resonantly excite intraexcitonic $1s$ -to- $2p$ transitions. The effect has been explained by a microscopic many-body theory of the efficient Coulomb-scattering mediated mixing of the 2s and the 2p states, which correctly predicts the appearance of the 2s PL. With this approach, the resonant THz pulse induces a direct transition between the excitonic 1s to the 2s state which is forbidden by dipole selection rules. The experimental evidence of the 2s PL emission is a good fingerprint to identify excitonic populations.

The results of the comparative study with two different THz photon energies strongly supports the hypothesis that the 1s PL quench originates mostly from an efficient carrier transfer to a continuum of dark states within the same level. The energy tuning of the free-electron laser to higher photon energies does not influence the 1s PL quenching much while a strongly reduced occupation probability of the 2s level is observed for the detuned case. Further work is needed to determine the 2s PL signal strength and decay time as a function of near-infrared fluence and lattice temperature. The question to be answered

is how the optical phonon density influences the relaxation process of the $2s$ population towards the dark $1sk$ level population.

As an outlook, the technique of time-resolved PL studies applied to the "classical" excitonic system in GaAs quantum wells may enhance the knowledge on ultrafast dynamics in novel materials. Recently, PL emission has been investigated on two-dimensional systems without band gap, where excited carriers cannot form excitons and do not radiatively recombine at the band minimum as for conventional PL emission. However, significant broad band light emission from pristine monolayer graphene [Nov04, Nov05] has been detected during short pulse laser excitation, where the electron system is driven out of equilibrium and is partially thermalized with phonons [Sto10, Lui10]. The combination of time-resolved PL spectroscopy with a second excitation might be a technique to get valuable insight into the carrier dynamics of graphene. To extend the time scale of relaxation, one could think of two-color studies on confined systems like graphene nanoribbons (1D) or graphene quantum dots (0D). Another interesting class of two-dimensional materials with finite band gap are transition metal dichalcogenides (TMDCs) that are promising candidates for flexible and transparent optoelectronic device applications [Wan12]. In particular, molybdenum and tungsten based TMDCs, such as MoS_2 , MoSe_2 , WS_2 , WSe_2 , are semiconductor materials with band gaps ranging from the visible to the near-infrared. In TMDC stacks, PL quenching has been observed due to a direct to indirect band gap transition [Yua15].

6 Magnetic control of excitonic photoluminescence emission

In the previous Chapter 5, the technique of time-resolved PL spectroscopy was combined with THz pulses resonant to the $1s$ -to- $2p$ intraexcitonic transition revealing efficient Coulomb scattering mechanism between the $2p$ and the $2s$ excitonic state of the GaAs quantum well samples. In the present Chapter, time-resolved PL measurements are performed with a modified setup, where the GaAs quantum well sample H063 is placed in a magneto-optical cryostat.

In a first part of this Chapter, intra-magnetoexcitonic transitions are identified from the strength of the THz induced $1s$ PL quenching in the magnetic field range between 0 T and 7 T. The time-resolved PL experiment is performed with the resonant THz photon energy of 8.7 meV, as well as for detuned photon energies of 9.4 meV, 10.5 meV, and 12.8 meV. At the arrival time of the THz pulse, the $1s$ PL intensity abruptly drops and recovers to a value higher than the reference trace. A variety of resonances is present in the magnetic field scans between 0 T and 7 T that are identified as $1s$ -to- np_{\pm} transitions of the quantum-well-confined magnetoexcitons and the electron-cyclotron resonance (e-CR). In a second part, the magnetic-field control of the $2s$ PL emission is studied between 0 T and 3 T. The reduced Coulomb scattering for elevated magnetic fields results in a decrease of the $2s$ PL signal strength. At the end of this chapter, the experimental obtained parameters for the $1s$ PL quenching and the $2s$ PL enhancement are compiled in summary plots and compared with theoretical curves for the THz induced $1s$ -to- np_{\pm} transitions.

Portions of this chapter have been published previously [Bha14].

6.1 THz induced intra-magnetoexcitonic transitions

For the PL studies with magnetic field, a magneto-optical cryostat was included in the experimental set-up connected with changes in the beam path as described in Section 3. In Faraday geometry, the homogeneous magnetic field is directed parallel to the wave vector of the THz beam such that the carrier motion lies within the quantum well layers.

The GaAs/AlGaAs quantum well sample H063 was mounted on the sample stick and kept at 8 K lattice temperature in the center of the magneto-optical cryostat.

During the experiment, higher excitonic states are populated after non-resonant excitation across the band gap by near-infrared laser pulses with photon energy of 1.627 eV. Through phonon relaxation, the induced population relaxes to the lowest excitonic level in the quantum well $1s$ state with an energy of 1.566 eV. For the transient studies, again, the time-resolved PL detection using the streak camera setup is combined with short pulse THz excitation. Through the near-infrared excitation and the external magnetic field, magnetoexcitons are created and the applied THz pulses induce transitions between their states. The magnetic field strength is manually tuned using an external control panel. For each of the chosen magnetic field values, a streak image of the PL signal is saved and compared with the reference measurement taken without THz excitation.

The results are interpreted as caused by the field-induced shift of the excitonic transition energies and the lifted degeneracy of the $2s$ and $2p$ energy states. The data analysis supports the new finding that the efficient Coulomb scattering between energetically degenerate states can be externally controlled by means of a magnetic field.

6.2 Magnetic-field control of THz induced $1s$ PL quenching

In Figure 6.1, calculated magnetoexcitonic $1s$ -to- np_{\pm} transitions are plotted according to [Bha14], [SR91]. The strong line splits into $1s$ -to- $2p_{+}$ and $1s$ -to- $2p_{-}$ with increasing field. While the $2p_{+}$ monotonically increases, the $2p_{-}$ curve initially exhibits a red shift with a minimum value around 1 T and subsequently it exhibits a blue shift. This behavior has been reported earlier, e.g., by [Nic00, Bar02, Mi09]. At zero field, the THz photon energy of 8.7 meV is resonant to the $1s$ -to- $2p_{\pm}$ transition according to the findings in Chapter 5. For all measured $1s$ PL transients, time profiles of the transient PL intensity are taken at the $1s$ energy and compared with the reference trace. As for the data presented in Chapter 5, the THz induced quenching q is analyzed using the model fit *fit-PL* and *fit-1s-dip* that are based on Equations (4.5) and (5.16), respectively. The strength of the PL quenching decreases with increasing magnetic field strength. In Figure 6.2(a), two excitation scenarios are plotted under resonant THz excitation with fluence of $\Phi_{\text{THz}} = 39 \text{ nJ cm}^{-2}$. Under these experimental conditions, the PL quenching saturates between 0 T and 2 T independently of the near-infrared fluence. In particular for lower THz fluence shown in Figure 6.2(b), several local maxima of $1s$ PL quenching are observed. These signatures are labeled according to the identified transitions shown in Figure 6.1.

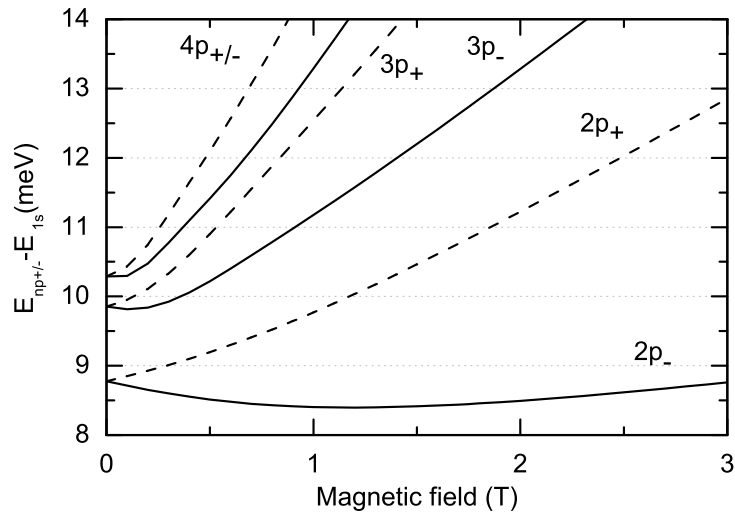


Figure 6.1: Calculated magnetoexcitonic 1s-to- np_{\pm} transitions showing the line splitting with magnetic field strength [Bha14, SR91].

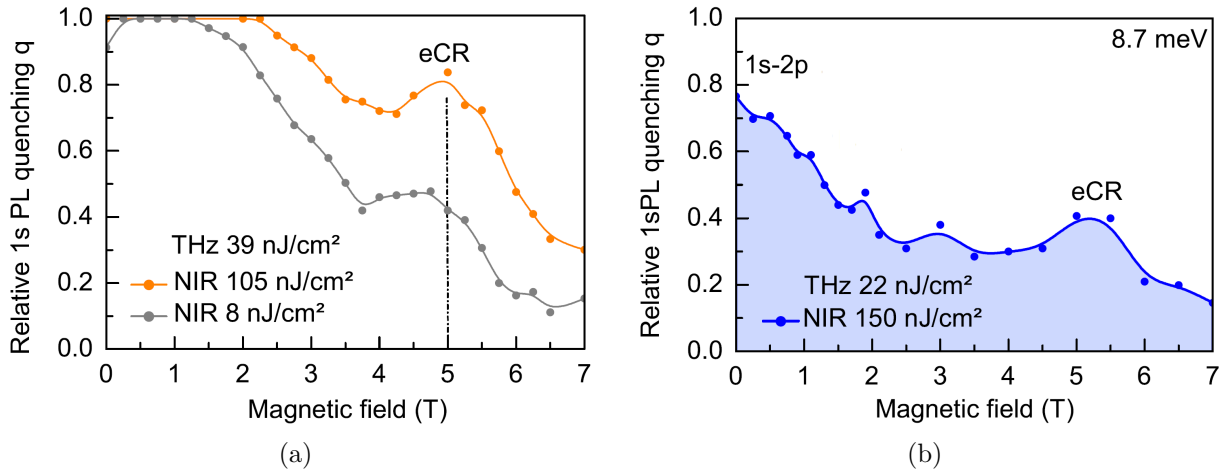


Figure 6.2: Relative 1s PL quenching q under resonant THz excitation of 8.7 meV with magnetic field. The colors indicate different combinations of near-infrared and THz fluences. (a) Strong THz excitation of $\Phi_{\text{THz}} = 39 \text{ nJ cm}^{-2}$ combined with near-infrared fluence of $\Phi_{\text{NIR}} = 105 \text{ nJ cm}^{-2}$ (orange) and of $\Phi_{\text{NIR}} = 8 \text{ nJ cm}^{-2}$ (gray). (b) Weaker THz excitation of $\Phi_{\text{THz}} = 22 \text{ nJ cm}^{-2}$ combined with near-infrared fluence of $\Phi_{\text{NIR}} = 150 \text{ nJ cm}^{-2}$.

However, the enhanced quenching around 5 T cannot be assigned to intraexcitonic transitions. The peak coincides with the electron-cyclotron resonance (e-CR) investigated, e.g., by [Nic00]. These findings are consistent with the observed dependency on the near-infrared induced carrier density shown in Figure 6.2. A large number of photogenerated carriers induced by a high near-infrared fluence results in a strong 1s PL quenching due to the e-CR. A high THz fluence, on the other hand, enhances the quenching caused by intraexcitonic transitions. The energetic structure of these transitions, however, is better resolved at lower THz fluences as the peaks saturate and merge at high THz fluences.

For higher THz photon energies, the $1s$ -to- $2p_+$ transition is non-resonant at zero field. The peaks shift according to the energy shift of the intraexcitonic transitions. For THz photon energies of 9.5 meV and 10.6 meV, the relative 1s PL quenching with magnetic field is shown in Figures 6.3(a) and 6.3(b), respectively. The excitation conditions are the same as for the measurements with 8.7 meV THz photon energy shown in Figure 6.2. The

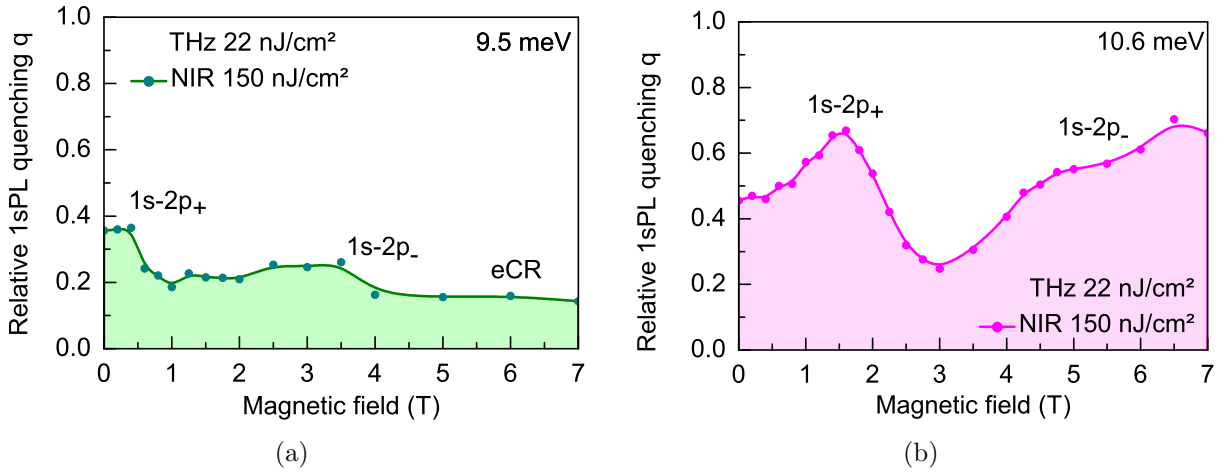


Figure 6.3: Relative 1s PL quenching q for different non-resonant THz photon energies: (a) 9.5 meV and (b) 10.6 meV. Both with THz fluence of $\Phi_{\text{THz}} = 22 \text{ nJ cm}^{-2}$ and NIR fluence of 150 nJ cm^{-2} .

weak quenching in 6.2(a) is seen as a consequence of the poor spatial overlap during laser excitation for this particular measurement. For a THz photon energy of 10.6 meV shown in 6.2(b), the $1s$ -to- $2p_+$ transition is visible as a peak centered at 1.5 T. The $1s$ -to- $2p_-$ transition induces enhanced quenching between 4 T and 7 T. In contrast to the $1s$ -to- np_+ transitions, different spin states are detectable for $1s$ -to- np_- intraexcitonic transitions [Nic00]. This fact might lead to the observed broadening of the resonance.

Furthermore, the induced quenching of the 1s PL is analyzed for a THz photon energy of 12.8 meV. The $1s$ -to- $2p_+$ resonance is expected at about 3.5 T, see Figure 6.1 and [Nic00]. For a magnetic field strength of 3.3 T, the obtained PL transients with and without THz excitation are shown in Figure 6.4(a) together with the model fit. The obtained quenching

parameter q is plotted for three different excitation scenarios as a function of the magnetic field strength in Figure 6.4(b). The resonance peak centered around 3.3 T is identified as

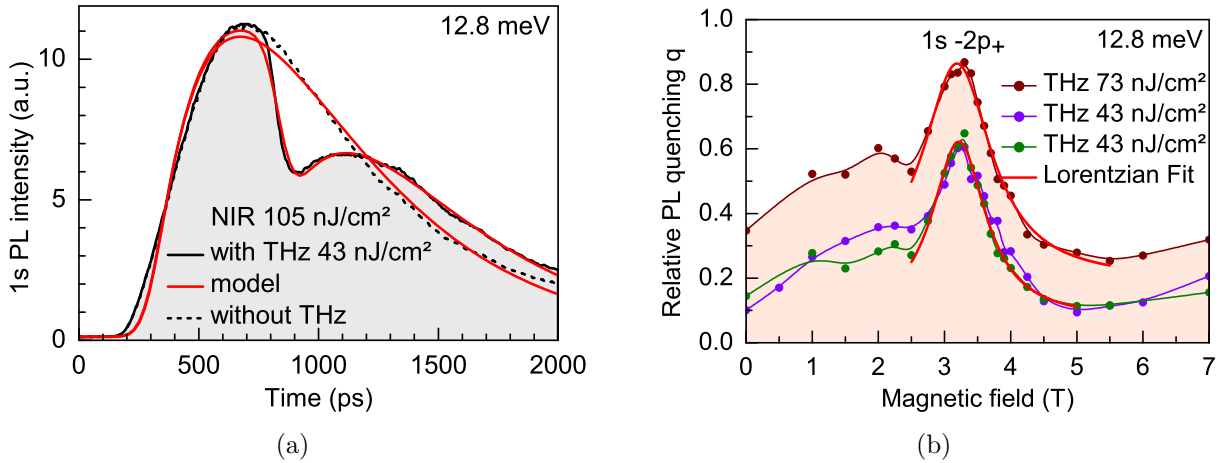


Figure 6.4: (a) Transient 1s PL intensity for 12.8 meV THz photon energy excited with 43 nJ cm^{-2} (shaded area) and the reference trace (dotted line) at the resonance peak around 3.3 T. (b) Relative 1s PL quenching q for nonresonant THz excitation (12.8 meV) with magnetic field. The colors indicate different combinations of near-infrared and THz excitation fluences. From upper to lower curve: NIR 8 nJ cm^{-2} and THz 73 nJ cm^{-2} ; NIR 105 nJ cm^{-2} and THz 43 nJ cm^{-2} ; NIR 8 nJ cm^{-2} and THz 43 nJ cm^{-2} . The red line is a Lorentzian fit to the $1s\text{-to-}2p_+$ transition peak.

the $1s\text{-to-}2p_+$ transition while the enhanced quenching between 1 T and 2.2 T is attributed to possible higher-order transitions $1s\text{-to-}3p_{\pm}$. The relative PL quenching reaches its maximum value around 3.3 T. It is 0.6 for both data sets that were taken with the lower THz fluence of 43 nJ cm^{-2} . The line width was obtained by a Lorentzian fit to a FWHM of 0.7 T. For an increased THz excitation density of 73 nJ cm^{-2} , the quenching at resonance saturates and the peak broadens to a FWHM of 1.26 T. The relative quenching for all the remaining magnetic field values changes linearly with the increased THz fluence. A synopsis of these experimental results is schematically shown below in form of the diagram presented in Figure 6.8.

6.3 Magnetic-field control of the THz induced 2s PL emission

In this Section, we focus on the magnetic control of the THz induced 2s PL emission strength. Simultaneously to the change in the 1s PL signal, the dynamics of the induced 2s PL emission is studied. At zero field, the quasi-degenerate 2s and 2p excitonic states have an energy of 1.575 eV. The energetic shift of the $1s\text{-to-}2p$ transitions between 0 T

and 7 T is studied for three different THz photon energies, namely 8.7 meV, 9.4 meV, and 10.6 meV. As the degeneracy of the states is lifted, the scattering strength between the $2p$ and the $2s$ state decreases with elevated magnetic field. The intensity of the $2s$ emission peak is expected to be much weaker than the $1s$ PL. The dynamical range of the CCD camera limits the detection of weak signals. In order to image the strong $1s$ as well as the weak $2s$ signal, a neutral density filter was installed after the spectrometer as described previously in Section 5.4.

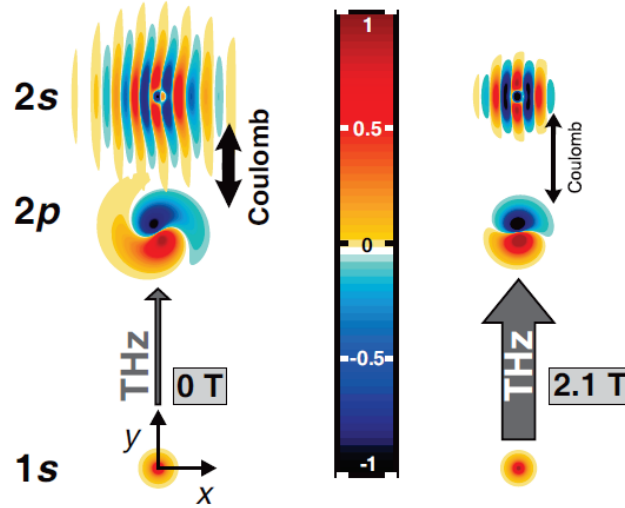


Figure 6.5: Visualization of the exciton wave function without magnetic field (left column) and with 2.1 T (right column). Horizontal and vertical directions x and y represent spatial coordinates. The perpendicular magnetic field squeezes the $1s$, $2p$, and $2s$ wave function (from lower to upper row). This figure has been published in [Bha14], copyright (2014) by The American Physical Society.

The spatial extent of the excitonic wave function is essential for the interpretation of the results. Calculations demonstrate the efficient reduction of the wave function's spatial extent and, thus, an increase of the THz-transition strength. The exciton wave functions and the influence of the magnetic field are depicted in Figure 6.5. The comparison between the situation for 0 T and 2.1 T visualizes the contraction of the $2p$ and $2s$ wave functions that reduces the scattering cross section between the respective excitonic states [Bha14]. The spiral shape is caused by the excitation-induced dephasing and is present only for the p -like states [Kir11].

6.3.1 Rate-equation analysis

With the experimental setup, the $2s$ PL signal strength is detected and controlled by tuning the magnetic field for a fixed THz photon energy. Strong $1s$ PL quenching at

zero field was found for 8.7 meV, where the photon energy is resonant to the $1s$ -to- $2p_{\pm}$ transition. With increasing magnetic field, the signal strength of the detected $2s$ emission peak gradually decreases and vanishes for all values larger than 2.5 T.

From the streak camera images, the PL transients were integrated over 3 meV at the $1s$ PL and the $2s$ PL energy. For analysis, the fit functions based on the rate equations are used as for the zero field experiment in the previous Chapter 5. In Figures 6.6(a) and 6.6(b), the transient $1s$ PL signal and the differential $2s$ PL signal are plotted for different magnetic field strengths together with a rate equation fit. Note the different scaling of Figures 6.6(a) and 6.6(b). In Figure 6.6(a), both transients are plotted to visualize the difference between the detected intensities and the PL dynamics. For the rate equation fit with *fit-1s-dip* based on Equation (5.16), the free parameters are the PL decay time τ_{PL} and the PL recovery time τ_k . The obtained time constants have the same value for all studied magnetic field strengths. There is no detectable change of the dynamics with increasing magnetic field. For all measured transients of this sample H063, the PL decay time $\tau_{\text{PL}} = 385$ ps matches the PL rise and recovery time τ_k . The $2s$ PL dynamics is simulated by the scattering times $\tau_{\text{rel}} = 40$ ps and $\tau_{\text{C}} = 10$ ps, where the latter is shorter than the time resolution of the signal $\sigma = 20$ ps. Note that for this approach, the amplitude scaling factor C_{2s} is the only free fitting parameter for the $2s$ PL emission. The slower decaying component is attributed to slow phonon relaxation, see [Ric13a], that is not regarded in the rate equation model.

From the evaluation of the PL transients, the decay of the $2s$ PL emission is found to be about ten times faster than the recovery of the $1s$ PL quench with a time constant of $\tau_k = 385$ ps. The $2s$ PL decay is limited by the nonradiative relaxation process of the $2s$ state into the high momentum $1sk$ states as has been found in the analysis of the zero field data in Chapter 5.

Results of the rate-equation analysis are plotted in Figure 6.7. The relative quench q of the $1s$ PL intensity and the THz-induced $2s$ PL emission at the arrival time of the THz pulse are plotted versus the magnetic field in Figures 6.7(a) and 6.7(b), respectively.

The change of the $2s$ PL emission strength with magnetic field is attributed to two effects that both correlate with the energy shift of the excitonic $2p$ state. Firstly, the photon energy of the THz pulse is not longer resonant to the $1s$ -to- $2p$ transition. The energetic width of the resonance can be estimated from that of the $1s$ quenching peak which ranges from 1 T to 1.5 T. Secondly, the $2p$ -to- $2s$ scattering rate decreases with the field strength as the degeneracy of the $2p$ and the $2s$ state is lifted.

For the data set taken with a THz photon energy of 10.6 meV, the induced $1s$ PL quenching q is about 0.5 at 0 T, see Figure 6.7(a). With elevated magnetic field strength, this relative PL quenching increases until it reaches its maximum value of 0.7 at 1.6 T

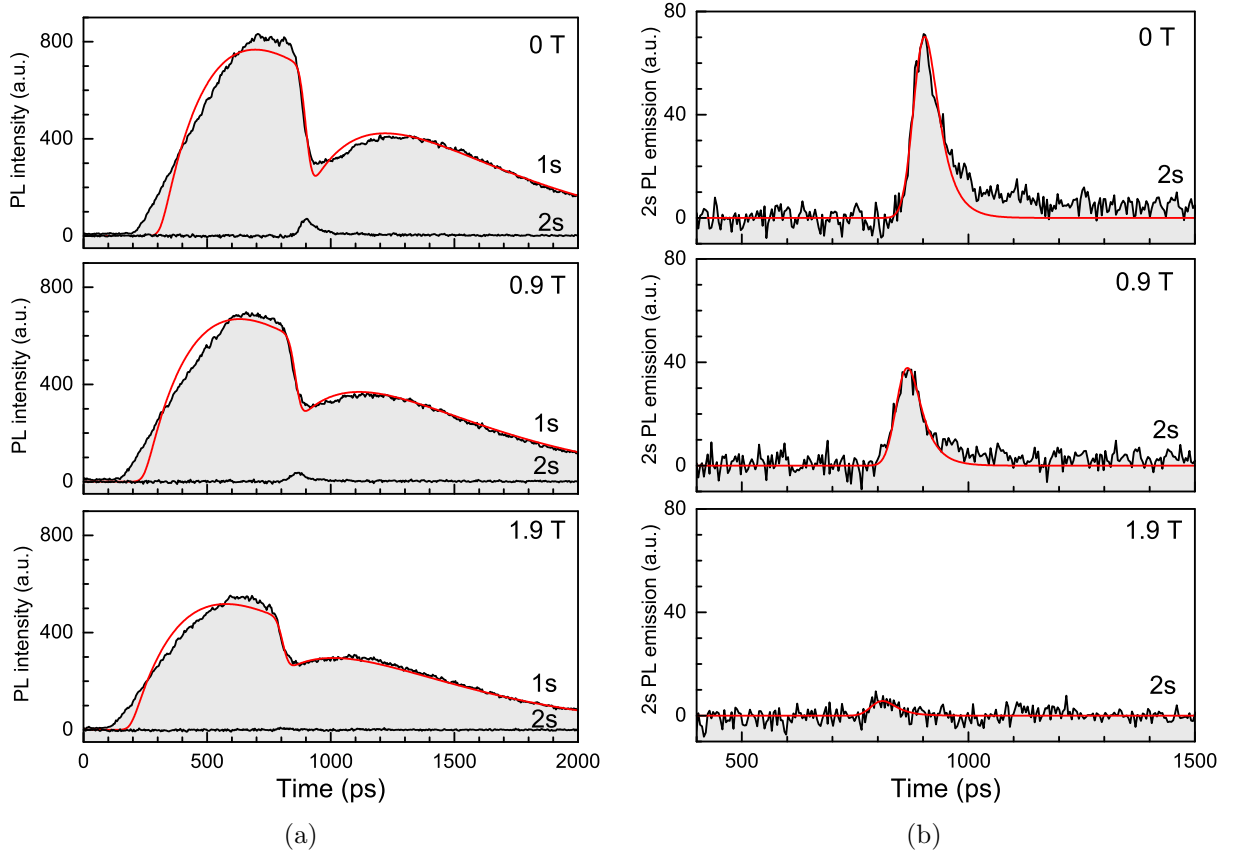


Figure 6.6: Transient PL intensity under THz excitation with 8.7 meV photon energy for 0 T, 0.9 T, and 1.9 T (from upper to lower panel). (a) PL emission at the 1s and the 2s energy. The red lines are the model fits to the data with parameters $\tau_{\text{PL}} = 383$ ps, $\tau_k = 385$ ps. The time resolution of the signal is $\sigma = 20$ ps. (b) Zoom into the 2s PL signal. The 2s PL signal is simulated with the time constants $\tau_{\text{rel}} = 40$ ps and the Coulomb scattering time $\tau_{\text{C}} = 10$ ps.

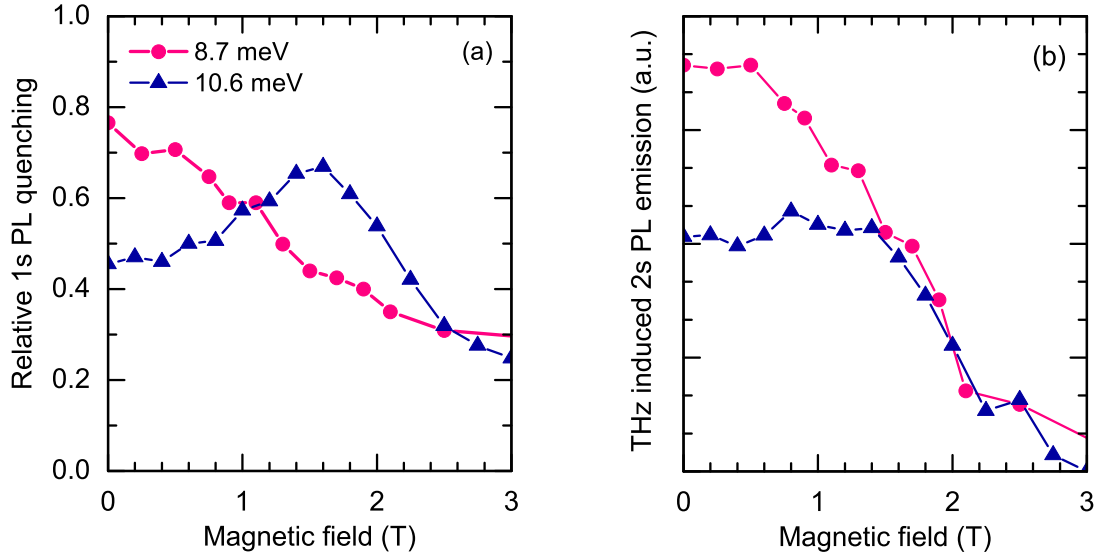


Figure 6.7: (a) Relative quench of the 1s PL intensity and (b) the THz induced 2s PL emission at the arrival time of the THz pulse as a function of the externally applied magnetic field. Pink and blue bullets show measurements taken with THz photon energies of 8.7 meV and 10.6 meV, respectively.

and decreases to about 0.2 at 3 T. The asymmetric shape of the resonance peak results from allowed higher-order excitonic transitions in the regime below 1.6 T.

6.4 Comparison between experiment and theory

In Figure 6.8, the experimental results of the present Chapter are summarized to a comprehensive magnetic field and THz photon energy dependence. The THz induced 1s PL quenching and the 2s PL emission are shown in the upper and the lower panel, respectively. The strength of the signatures is encoded both as symbol size and color, where small blue and big red bullets represent minimum and maximum, respectively. Note that the actual values only scale within the same THz photon energy. Black solid and dashed lines represent the calculated energy dispersion curves for the allowed transitions from the 1s ground state to the p -symmetry excited states $1s$ -to- np_{\pm} that were shown before in Figure 6.1 and [Bha14]. The linear change of the e-CR is marked with a red line according to [Nic00]. For all the evaluated THz energies, the strongest PL quenching is in good agreement with the calculated transition energies of the $2p_{+}$ branch. The bending of the $2p_{-}$ branch is reflected in a decreased 1s PL quenching around 1 T and an increased relative quenching at about 3 T.

In the lower panel of Figure 6.8, the strength of the corresponding 2s PL signal is plotted. For all studied THz photon energies, the detected 2s PL signal intensity has a finite value for $B = 0$ and tends to zero for magnetic field strengths larger than 2.5 T. In

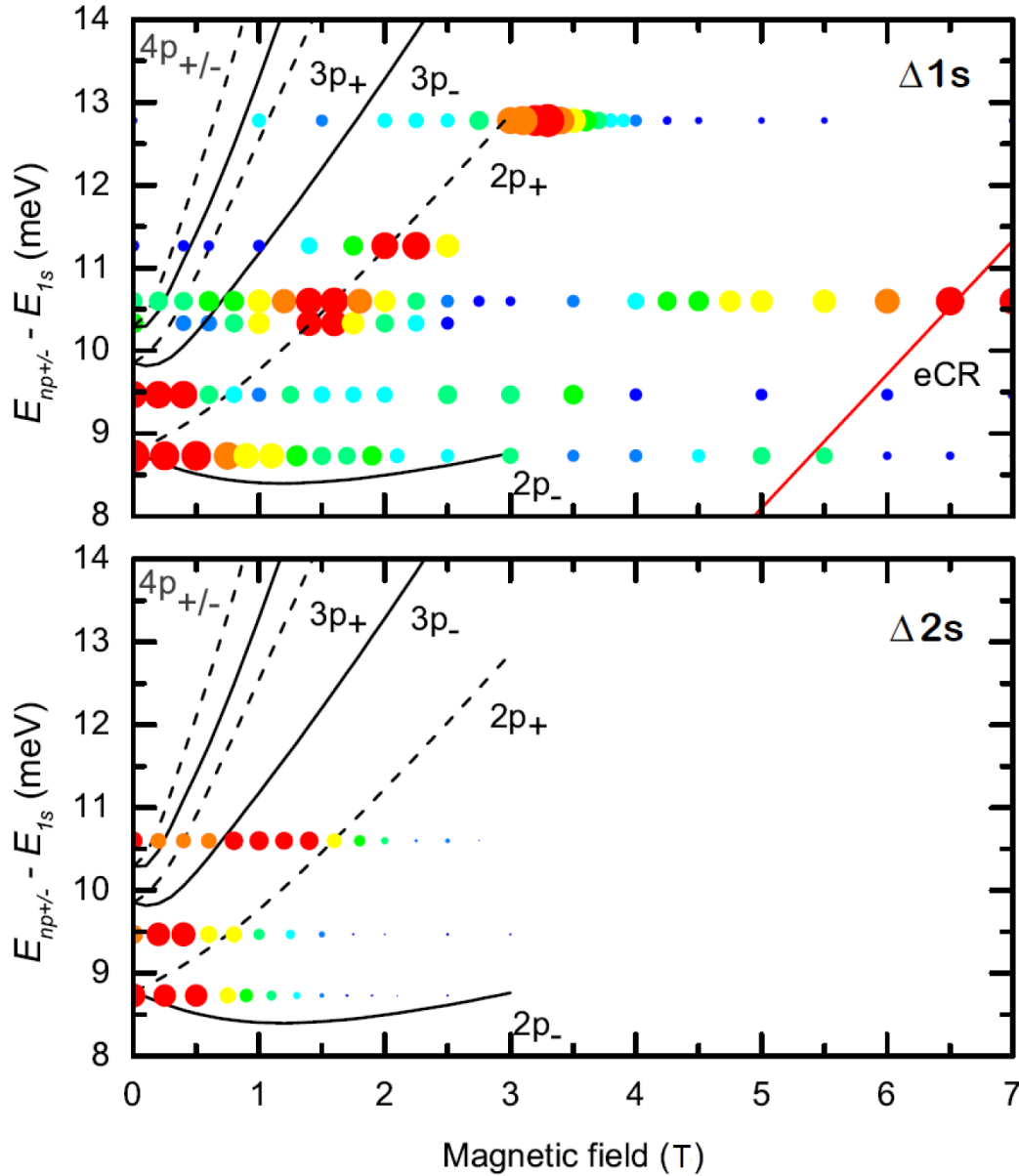


Figure 6.8: Overview of the THz induced changes of the transient PL signal with magnetic field together with calculated transitions [Bha14] (black lines). All data points are plotted as color and size mapped bullets, where small blue bullets represent the minimum values and the big red bullets represent maximum values. The THz induced quenching of the 1s PL signal is shown in the upper panel. The red line shows the change of the electron cyclotron resonance [Nic00]. The THz induced 2s PL at the arrival time of the THz pulse is plotted in the lower panel.

case of THz excitation with photon energy of 8.7 meV, that is resonant to the $1s$ -to- $2p$ transition without magnetic field, the $2s$ PL signal decreases linearly above 0.5 T. For slightly detuned THz photon energy of 9.4 meV, the overall $2s$ PL strength is weaker and shows a faster decrease with increasing magnetic field. At about 0.8 T, where the THz photons are resonant to the $1s$ -to- $2p_+$ transition, the Coulomb scattering is less efficient and the population transfer into the radiative $2s$ level is reduced.

The many-body theory developed by Kira et al. [Kir11, Bha14] supports the finding that the picture of the Coulomb mediated $1s$ -to- $2s$ scattering is not sufficient to explain the experimentally observed transient PL changes. Calculated PL emission based on a limited system of only the $1s$, $2s$, $2p_-$, and $2p_+$ state, or without any scattering is not in accordance with the detected PL dynamics. These calculations lead to the reverse conclusion that all excitonic states are involved in the internal dynamics [Bha14].

With this setup, it is not possible to cover the necessary energy-magnetic-field space in infinitely small steps with data points. Automatic scanning through the parameter space is not possible with our setup. The magnetic field can be manually tuned in 10 μ T steps but the free electron laser is set at a certain energy and cannot be arbitrary changed. The water absorption lines are quite dense in the relevant energy scale and thus, limit the operation of the free-electron laser to certain "working" wavelengths. And of course we have had really limited beam time. However, the summary plot in Figure 6.8 consistently supports the interpretation of the peaks based on six studied THz photon energies.

6.5 Summary and outlook

Time-resolved PL measurements are performed on quantum wells subject to a static magnetic field in growth direction. Firstly, intra-magnetoexcitonic transitions are identified from the strength of the THz induced $1s$ PL quenching between 0 T and 7 T. In a second experiment, the strength of the induced $2s$ emission signal is traced synchronously to the $1s$ PL quenching. With our experimental method, we show that the diffusive Coulomb scattering between the excitonic states is strongly dependent on the magnetic field strength. For all studied magnetic fields strengths, the $2s$ PL decay time τ_{rel} is about ten times faster than the PL recovery τ_{PL} . Possible changes of the Drude absorption with field are not resolvable.

The transient intra-magnetoexcitonic PL study shows that the quantum states experience experimental significant effects which could be used for the development of radiation-emitting nanoscale devices. Externally applied magnetic fields might be used to control the photon energy and the emission intensity output of optoelectronic devices based on quantum wells.

Bibliography

- [Amo06] A. Amo, M. D. Martin, L. Viña, A. I. Toropov, and K. S. Zhuravlev, Interplay of exciton and electron-hole plasma recombination on the photoluminescence dynamics in bulk GaAs, *Phys. Rev. B* **73**, 035205 (2006).
- [Amo08] A. Amo, D. Ballarini, D. Sanvitto, E. Kozhemyakina, L. Viña, A. Lemaître, D. Bajoni, and J. Bloch, Optically induced ultrafast quenching of the semiconductor quantum well luminescence, *Appl. Phys. Lett.* **92**, 061912 (2008).
- [Amo10] A. Amo, D. Sanvitto, and L. Viña, Collective dynamics of excitons and polaritons in semiconductor nanostructures, *Semiconductor Science and Technology* **25**, 043001 (2010).
- [Bal00] M. Balkanski and R. F. Wallis, *Semiconductor Physics and Applications*, (Oxford Univ. Press, New York, 2000).
- [Bar02] Z. Barticevic, M. Pacheco, C. A. Duque, and L. E. Oliveira, Magnetoabsorption spectra of intraexcitonic transitions, *J. Appl. Phys.* **92**, 1227 (2002).
- [Bas88] G. Bastard, *Wave Mechanics Applied to Semiconductor Heterostructures*, (Les Editions de Physique, Paris, 1988).
- [Bha11] J. Bhattacharyya, M. Wagner, S. Zybell, S. Winnerl, D. Stehr, M. Helm, and H. Schneider, Simultaneous time and wavelength resolved spectroscopy under two-colour near infrared and terahertz excitation, *Rev. Sci. Instrum.* **82**, 103107 (2011).
- [Bha14] J. Bhattacharyya, S. Zybell, F. Eßer, M. Helm, H. Schneider, L. Schneebeli, C. N. Böttge, B. Breddermann, M. Kira, S. W. Koch, A. M. Andrews, and G. Strasser, Magnetic control of Coulomb scattering and terahertz transitions among excitons, *Phys. Rev. B* **89**, 125313 (2014).
- [Blo93] P. W. M. Blom, P. J. van Hall, C. Smit, J. P. Cuypers, and J. H. Wolter, Selective exciton formation in thin GaAs/Al_xGa_{1-x}As quantum wells, *Phys. Rev. Lett.* **71**, 3878 (1993).

- [Bug86] M. Bugajski, W. Kuszko, and K. Regiński, Diamagnetic shift of exciton energy levels in GaAs/Ga_{1-x}Al_xAs quantum wells, *Solid State Commun.* **60**, 669 (1986).
- [Cer95] J. Cerne, A. G. Markelz, M. S. Sherwin, S. J. Allen, M. Sundaram, A. C. Gossard, P. C. van Son, and D. Bimberg, Quenching of excitonic quantum-well photoluminescence by intense far-infrared radiation: Free-carrier heating, *Phys. Rev. B* **51**, 5253 (1995).
- [Cer96] J. Cerne, J. Kono, M. S. Sherwin, M. Sundaram, A. C. Gossard, and G. E. W. Bauer, Terahertz dynamics of excitons in quantum wells, *Phys. Rev. Lett.* **77**, 1131 (1996).
- [Cha03] S. Chatterjee, *Exciton formation dynamics in semiconductor quantum wells*, Ph.D. thesis, The University of Arizona (2003).
- [Cha04] S. Chatterjee, C. Ell, S. Mosor, G. Khitrova, H. M. Gibbs, W. Hoyer, M. Kira, S. W. Koch, J. P. Prineas, and H. Stolz, Excitonic photoluminescence in semiconductor quantum wells: Plasma versus excitons, *Phys. Rev. Lett.* **92**, 067402 (2004).
- [Chr90] J. Christen and D. Bimberg, Line shapes of intersubband and excitonic recombination in quantum wells: Influence of final-state interaction, statistical broadening, and momentum conservation, *Phys. Rev. B* **42**, 7213 (1990).
- [Dam90] T. C. Damen, J. Shah, D. Y. Oberli, D. S. Chemla, J. E. Cunningham, and J. M. Kuo, Dynamics of exciton formation and relaxation in GaAs quantum wells, *Phys. Rev. B* **42**, 7434 (1990).
- [Dev91] B. Deveaud, F. Clérot, N. Roy, K. Satzke, B. Sermage, and D. S. Katzer, Enhanced radiative recombination of free excitons in GaAs quantum wells, *Phys. Rev. Lett.* **67**, 2355 (1991).
- [Ecc91] R. Eccleston, R. Strobel, W. W. Rühle, J. Kuhl, B. F. Feuerbacher, and K. Ploog, Exciton dynamics in a GaAs quantum well, *Phys. Rev. B* **44**, 1395 (1991).
- [Els91] T. Elsaesser, J. Shah, L. Rota, and P. Lugli, Initial thermalization of photoexcited carriers in GaAs studied by femtosecond luminescence spectroscopy, *Phys. Rev. Lett.* **66**, 1757 (1991).
- [Fai94] J. Faist, F. Capasso, D. L. Sivco, C. Sirtori, A. L. Hutchinson, and A. Y. Cho, Quantum cascade laser, *Science* **264**, 553 (1994).

- [Fel87] J. Feldmann, G. Peter, E. O. Göbel, P. Dawson, K. Moore, C. Foxon, and R. J. Elliott, Linewidth dependence of radiative exciton lifetimes in quantum wells, *Phys. Rev. Lett.* **59**, 2337 (1987).
- [Gal05] I. Galbraith, R. Chari, S. Pellegrini, P. J. Phillips, C. J. Dent, A. F. G. van der Meer, D. G. Clarke, A. K. Kar, G. S. Buller, C. R. Pidgeon, B. N. Murdin, J. Allam, and G. Strasser, Excitonic signatures in the photoluminescence and terahertz absorption of a GaAs/Al_xGa_{1-x}As multiple quantum well, *Phys. Rev. B* **71**, 073302 (2005).
- [Hel89] M. Helm, P. England, E. Colas, F. de Rosa, and S. J. Allen, Intersubband emission from semiconductor superlattices excited by sequential resonant tunneling, *Phys. Rev. Lett.* **63**, 74 (1989).
- [Hel00] M. Helm, *Semiconductor and Semimetal*, vol. 62, chap. The basic physics of intersubband transitions, 1–99, (Academic Press, 2000).
- [Hen07] E. Hendry, M. Koeberg, and M. Bonn, Exciton and electron-hole plasma formation dynamics in ZnO, *Phys. Rev. B* **76**, 045214 (2007).
- [Hoy05] W. Hoyer, C. Ell, M. Kira, S. W. Koch, S. Chatterjee, S. Mosor, G. Khitrova, H. M. Gibbs, and H. Stolz, Many-body dynamics and exciton formation studied by time-resolved photoluminescence, *Phys. Rev. B* **72**, 075324 (2005).
- [Kai03] R. A. Kaindl, M. A. Carnahan, D. Hägele, R. Lovenich, and D. S. Chemla, Ultrafast terahertz probes of transient conducting and insulating phases in an electron-hole gas, *Nature* **423**, 734 (2003).
- [Kai09] R. A. Kaindl, D. Hägele, M. A. Carnahan, and D. S. Chemla, Transient terahertz spectroscopy of excitons and unbound carriers in quasi-two-dimensional electron-hole gases, *Phys. Rev. B* **79**, 045320 (2009).
- [Kap05] L. Kappei, J. Szczytko, F. Morier-Genoud, and B. Deveaud, Direct observation of the Mott transition in an optically excited semiconductor quantum well, *Phys. Rev. Lett.* **94**, 147403 (2005).
- [Kas84] K. Kash and J. Shah, Carrier energy relaxation in In_{0.53}Ga_{0.47}As determined from picosecond luminescence studies, *Appl. Phys. Lett.* **45**, 401 (1984).
- [Kir04] M. Kira and S. W. Koch, Exciton-population inversion and terahertz gain in semiconductors excited to resonance, *Phys. Rev. Lett.* **93**, 076402 (2004).

- [Kir11] M. Kira and S. W. Koch, *Semiconductor Quantum Optics*, (Cambridge University, Cambridge, 2011).
- [Kla01] F. Klappenberger, A. A. Ignatov, S. Winnerl, E. Schomburg, W. Wegscheider, K. F. Renk, and M. Bichler, Broadband semiconductor superlattice detector for THz radiation, *Appl. Phys. Lett.* **78**, 1673 (2001).
- [Koc06] S. W. Koch, M. Kira, G. Khitrova, and H. M. Gibbs, Semiconductor excitons in new light, *Nat. Mat.* **5**, 523 (2006).
- [Koh54] W. Kohn and J. M. Luttinger, Quantum theory of cyclotron resonance in semiconductors, *Phys. Rev.* **96**, 529 (1954).
- [Kum96] R. Kumar, A. S. Vengurlekar, S. S. Prabhu, J. Shah, and L. N. Pfeiffer, Picosecond time evolution of free electron-hole pairs into excitons in GaAs quantum wells, *Phys. Rev. B* **54**, 4891 (1996).
- [Kus89] J. Kusano, Y. Segawa, Y. Aoyagi, S. Namba, and H. Okamoto, Extremely slow energy relaxation of a two-dimensional exciton in a GaAs superlattice structure, *Phys. Rev. B* **40**, 1685 (1989).
- [Lee95] I. Lee, S. M. Goodnick, M. Gulia, E. Molinari, and P. Lugli, Microscopic calculation of the electron-optical-phonon interaction in ultrathin GaAs/Al_xGa_{1-x}As alloy quantum-well systems, *Phys. Rev. B* **51**, 7046 (1995).
- [Leo88] K. Leo, W. W. Rühle, and K. Ploog, Hot-carrier energy-loss rates in GaAs/Al_xGa_{1-x}As quantum wells, *Phys. Rev. B* **38**, 1947 (1988).
- [Liu88] H. C. Liu, A novel superlattice infrared source, *J. Appl. Phys.* **63**, 2856 (1988).
- [Lob89] H. Lobentanzer, W. Stolz, J. Nagle, and K. Ploog, Cooling of hot carriers in three- and two-dimensional Ga_{0.47}In_{0.53}As, *Phys. Rev. B* **39**, 5234 (1989).
- [Lui10] C. H. Lui, K. F. Mak, J. Shan, and T. F. Heinz, Ultrafast photoluminescence from graphene, *Phys. Rev. Lett.* **105**, 127404 (2010).
- [Lut56] J. M. Luttinger, Quantum theory of cyclotron resonance in semiconductors: General theory, *Phys. Rev.* **102**, 1030 (1956).
- [Man12] G. Manzke, D. Semkat, and H. Stolz, Mott transition of excitons in GaAs-GaAlAs quantum wells, *New J. Phys.* **14**, 095002 (2012).

- [Men82] E. E. Mendez, G. Bastard, L. L. Chang, L. Esaki, H. Morkoc, and R. Fischer, Effect of an electric field on the luminescence of GaAs quantum wells, *Phys. Rev. B* **26**, 7101 (1982).
- [Mi09] X. Mi, D. Li, F. Meng, and H. Zhao, Magnetoabsorption spectra of magnetoexciton transitions in GaAs/Ga_{0.7}Al_{0.3}As quantum wells, *Chin. Opt. Lett.* **7**, 335 (2009).
- [Mii90] Y. J. Mii, K. L. Wang, R. P. G. Karunasiri, and P. F. Yuh, Observation of large oscillator strengths for both 1→2 and 1→3 intersubband transitions of step quantum wells, *Appl. Phys. Lett.* **56**, 1046 (1990).
- [Nic00] H. A. Nickel, G. Kioseoglou, T. Yeo, H. D. Cheong, A. Petrou, B. D. McCombe, D. Broido, K. K. Bajaj, and R. A. Lewis, Internal transitions of confined neutral magnetoexcitons in quantum wells, *Phys. Rev. B* **62**, 2773 (2000).
- [Nov04] K. S. Novoselov, A. K. Geim, S. V. Morozov, D. Jiang, Y. Zhang, S. V. Dubonos, I. V. Grigorieva, and A. A. Firsov, Electric field effect in atomically thin carbon films, *Science* **306**, 666 (2004).
- [Nov05] K. S. Novoselov, A. K. Geim, S. V. Morozov, D. Jiang, M. I. Katsnelson, I. V. Grigorieva, S. V. Dubonos, and A. A. Firsov, Two-dimensional gas of massless dirac fermions in graphene, *Nature* **438**, 197 (2005).
- [Obe12] D. Y. Oberli, Intertwining of Zeeman and Coulomb interactions on excitons in highly symmetric semiconductor quantum dots, *Phys. Rev. B* **85**, 155305 (2012).
- [Pel12] I. Pelant and J. Valenta, *Luminescence Spectroscopy of Semiconductors*, (Oxford Univ. Press, Oxford, 2012).
- [Pse03] J. Psenčík, Y. Z. Ma, J. B. Arellano, J. Hála, and T. Gillbro, Excitation energy transfer dynamics and excited-state structure in chlorosomes of *Chlorobium phaeobacteroides*, *Biophys. J.* **84**, 1161 (2003).
- [Qui92] S. M. Quinlan, A. Nikroo, M. S. Sherwin, M. Sundaram, and A. C. Gossard, Photoluminescence from Al_xGa_{1-x}As/GaAs quantum wells quenched by intense far-infrared radiation, *Phys. Rev. B* **45**, 9428 (1992).
- [Ram90] M. Ramsteiner, J. D. Ralston, P. Koidl, B. Dischler, H. Biebl, J. Wagner, and H. Ennen, Doping density dependence of intersubband transitions in GaAs/Al_xGa_{1-x}As quantum-well structures, *J. Appl. Phys.* **67**, 3900 (1990).

- [Ric13a] W. D. Rice, J. Kono, S. Zybell, S. Winnerl, J. Bhattacharyya, H. Schneider, M. Helm, B. Ewers, A. Chernikov, M. Koch, S. Chatterjee, G. Khitrova, H. M. Gibbs, L. Schneebeli, B. Breddermann, M. Kira, and S. W. Koch, Observation of forbidden exciton transitions mediated by Coulomb interactions in photoexcited semiconductor quantum wells, *Phys. Rev. Lett.* **110**, 137404 (2013).
- [Ric13b] W. D. Rice, J. Kono, S. Zybell, S. Winnerl, J. Bhattacharyya, H. Schneider, M. Helm, B. Ewers, A. Chernikov, M. Koch, S. Chatterjee, G. Khitrova, H. M. Gibbs, L. Schneebeli, B. Breddermann, M. Kira, and S. W. Koch, Supplemental material (2013).
- [Rum96] S. Rumyantsev and M. Shur, *Handbook Series on Semiconductor Parameters*, vol. 2, (World Scientific, 1996).
- [Sak85] H. Sakaki, Y. Arakawa, M. Nishioka, J. Yoshino, H. Okamoto, and N. Miura, Light emission from zero-dimensional excitons – photoluminescence from quantum wells in strong magnetic fields, *Appl. Phys. Lett.* **46**, 83 (1985).
- [Sch06a] H. Schneider and H. C. Liu, *Quantum Well Infrared Photodetectors: Physics and Applications*, (Springer Series in Optical Sciences, 2006).
- [Sch06b] G. D. Scholes and G. Rumbles, Excitons in nanoscale systems, *Nat. Mat.* **5**, 683 (2006).
- [Sne92] M. J. Snelling, E. Blackwood, C. J. McDonagh, R. T. Harley, and C. T. B. Foxon, Exciton, heavy-hole, and electron g factors in type-I GaAs/Al_xGa_{1-x}As quantum wells, *Phys. Rev. B* **45**, 3922 (1992).
- [SR91] S. Schmitt-Rink, J. Stark, W. Knox, D. Chemla, and W. Schfer, Optical properties of quasi-zero-dimensional magneto-excitons, *Applied Physics A* **53**, 491 (1991).
- [Sta90] J. B. Stark, W. H. Knox, D. S. Chemla, W. Schäfer, S. Schmitt-Rink, and C. Stafford, Femtosecond dynamics of excitons under extreme magnetic confinement, *Phys. Rev. Lett.* **65**, 3033 (1990).
- [Ste08] M. Stern, V. Garmider, V. Umansky, and I. Bar-Joseph, Mott transition of excitons in coupled quantum wells, *Phys. Rev. Lett.* **100**, 256402 (2008).
- [Sto10] R. J. Stoehr, R. Kolesov, J. Pflaum, and J. Wrachtrup, Fluorescence of laser-created electron-hole plasma in graphene, *Phys. Rev. B* **82**, 121408 (2010).

- [Suz09] T. Suzuki and R. Shimano, Time-resolved formation of excitons and electron-hole droplets in Si studied using terahertz spectroscopy, *Phys. Rev. Lett.* **103**, 057401 (2009).
- [Szc04] J. Szczytko, L. Kappei, J. Berney, F. Morier-Genoud, M. T. Portella-Oberli, and B. Deveaud, Determination of the exciton formation in quantum wells from time-resolved interband luminescence, *Phys. Rev. Lett.* **93**, 137401 (2004).
- [Sze07] S. M. Sze and K. K. Ng, *Physics of Semiconductor Devices*, (Wiley, 2007).
- [Tak92] Y. Takahashi, S. Owa, S. S. Kano, K. Muraki, S. Fukatsu, Y. Shiraki, and R. Ito, Two-dimensional exciton dynamics in InGaAs/GaAs quantum wells, *Appl. Phys. Lett.* **60**, 213 (1992).
- [Tan95] C. Tanguy, Optical dispersion by Wannier excitons, *Phys. Rev. Lett.* **75**, 4090 (1995).
- [Tsa01] F. Y. Tsai, C. P. Lee, O. Voskoboynikov, H. H. Cheng, J. Shen, and Y. Oka, Time-resolved photoluminescence study of InGaAs/GaAs quantum wells on (111)B GaAs substrates under magnetic fields, *J. Appl. Phys.* **89**, 7875 (2001).
- [Tse01] K. Tsen, *Ultrafast Phenomena in Semiconductors*, (Springer-Verlag, 2001).
- [Vur01] I. Vurgaftman, J. R. Meyer, and L. R. Ram-Mohan, Band parameters for III-V compound semiconductors and their alloys, *Journal of Applied Physics* **89**, 5815 (2001).
- [Wag09a] M. Wagner, *Terahertz studies on semiconductor quantum heterostructures in the low and high field regime*, Ph.D. thesis, Forschungszentrum Dresden-Rossendorf and Technische Universität Dresden (2009).
- [Wag09b] M. Wagner, H. Schneider, S. Winnerl, M. Helm, T. Roch, A. M. Andrews, S. Schartner, and G. Strasser, Resonant enhancement of second order sideband generation for intraexcitonic transitions in GaAs/AlGaAs multiple quantum wells, *Appl. Phys. Lett.* **94**, 241105 (2009).
- [Wag10] M. Wagner, H. Schneider, D. Stehr, S. Winnerl, A. M. Andrews, S. Schartner, G. Strasser, and M. Helm, Observation of the intraexciton Autler-Townes effect in GaAs/AlGaAs semiconductor quantum wells, *Phys. Rev. Lett.* **105**, 167401 (2010).
- [Wal98] S. N. Walck and T. L. Reinecke, Exciton diamagnetic shift in semiconductor nanostructures, *Phys. Rev. B* **57**, 9088 (1998).

- [Wan12] Q. H. Wang, K. Kalantar-Zadeh, A. Kis, J. N. Coleman, and M. S. Strano, Electronics and optoelectronics of two-dimensional transition metal dichalcogenides, *Nature Nanotechnology* **7**, 699712 (2012).
- [Wes85] L. C. West and S. J. Eglash, First observation of an extremely large-dipole infrared transition within the conduction band of a GaAs quantum well, *Appl. Phys. Lett.* **46**, 1156 (1985).
- [Yua15] J. Yuan, S. Najmaei, Z. Zhang, J. Zhang, S. Lei, P. M. Ajayan, B. I. Yakobson, and J. Lou, Photoluminescence quenching and charge transfer in artificial heterostacks of monolayer transition metal dichalcogenides and few-layer black phosphorus, *ACS Nano* **9**, 555 (2015).
- [Yuh89] P. F. Yuh and K. L. Wang, Optical transitions in a step quantum well, *J. Appl. Phys.* **65**, 4377 (1989).
- [Zvy09] S. A. Zvyagin, M. Ozerov, E. Čížmár, D. Kamenskyi, S. Zherlitsyn, T. Herrmannsdörfer, J. Wosnitza, R. Wünsch, and W. Seidel, Terahertz-range free-electron laser electron spin resonance spectroscopy: Techniques and applications in high magnetic fields, *Rev. Sci. Instrum.* **80**, 073102 (2009).
- [Zyb11] S. Zybell, H. Schneider, S. Winnerl, M. Wagner, K. Köhler, and M. Helm, Photoluminescence dynamics in GaAs/AlGaAs quantum wells under pulsed intersubband excitation, *Appl. Phys. Lett.* **99**, 041103 (2011).
- [Zyb14] S. Zybell, J. Bhattacharyya, S. Winnerl, F. Eßer, M. Helm, H. Schneider, L. Schneebeli, C. N. Böttge, M. Kira, S. W. Koch, A. M. Andrews, and G. Strasser, Characterizing intra-exciton coulomb scattering in terahertz excitations, *Appl. Phys. Lett.* **105**, 201109 (2014).

List of Figures

2.1	Conduction and valence band profile	6
2.2	Hydrogen atom and possible electron-hole configurations	13
2.3	The in-plane energy dispersion	14
2.4	Exciton Mott transition	14
2.5	Gradual Mott transition	15
2.6	Recombination	19
3.1	Streak camera	23
3.2	Experimental setup	24
3.3	Magneto-optical superconducting magnet system	26
3.4	Experimental setup for magneto PL	27
3.5	PL signal of sample 1267	29
3.6	Temperature dependent PL signal	29
3.7	Time integrated spectra of sample H063 for high excitation densities	30
4.1	In-plane energy dispersion under resonant mid-infrared excitation	34
4.2	Quenched PL transients from sample 1267	36
4.3	Excitation and relaxation processes in the quantum well	37
4.4	Experimental and modeled PL transients on samples 1267	39
4.5	Rate equation fit on the temperature dependent data	39
4.6	Modeled population dynamics	42
4.7	Parameter of fitted PL curves	43
4.8	Wave guide geometry	44
4.9	Intersubband resonance	45
4.10	Polarization dependent PL quenching	46
5.1	Schemes of the intraexcitonic transition studies.	50
5.2	THz-induced changes of transient PL emission	51
5.3	Computed differential PL	54
5.4	Time-resolved PL under THz irradiation	56
5.5	The excitonic levels at the arrival time of the THz pulse	58

5.6	Modeled dynamics based on a four level system	62
5.7	Modeled level occupation number	63
5.8	Relative quenching of 1s PL intensity	64
6.1	Calculated magnetoexcitonic 1s-to-np _± transitions	71
6.2	Relative 1s PL quenching under resonant THz excitation	71
6.3	Relative 1s PL quenching under non-resonant THz excitation	72
6.4	Quenching of 1s PL intensity with magnetic field	73
6.5	Visualization of exciton wave function	74
6.6	Transient PL intensity under THz excitation	76
6.7	THz induced signal on magnetoPL	77
6.8	Summary plot	78

List of Tables

2.1	Comparison of hydrogen atom, Wannier exciton, and Frenkel exciton . . .	13
3.1	Characteristics of the studied samples.	28

The following publications have been released in connection with the preparation of this dissertation:

- 11/2014 S. Zybell, J. Bhattacharyya, S. Winnerl, F. Eßer, M. Helm, and H. Schneider, L. Schneebeli, C. N. Böttge, M. Kira, and S. W. Koch, A. M. Andrews, and G. Strasser, **Characterizing intra-exciton Coulomb scattering in terahertz excitations**,
Applied Physics Letters **105**, 201109 (2014).
- 03/2014 J. Bhattacharyya, S. Zybell, F. Eßer, M. Helm and H. Schneider, L. Schneebeli, C. N. Böttge, B. Breddermann, M. Kira, S. W. Koch, A. M. Andrews, and G. Strasser, **Magnetic control of Coulomb scattering and terahertz transitions among excitons** ,
Physical Review B **89**, 125313 (2014).
- 02/2013 W. D. Rice, J. Kono, S. Zybell, S. Winnerl, J. Bhattacharyya, H. Schneider, M. Helm, B. Ewers, A. Chernikov, M. Koch, S. Chatterjee, G. Khitrova, H. M. Gibbs, L. Schneebeli, B. Breddermann, M. Kira, and S. W. Koch, **Observation of forbidden exciton transitions mediated by Coulomb interactions in photoexcited semiconductor quantum wells**,
Physical Review Letters **110**, 137404 (2013).
- 04/2012 J. Bhattacharyya, S. Zybell, S. Winnerl, M. Helm, M. Hopkinson, L. R. Wilson, and H. Schneider, **In-plane interdot carrier transfer in InAs/GaAs quantum dots**,
Applied Physics Letters **100**, 152101 (2012).
- 10/2011 J. Bhattacharyya, M. Wagner, S. Zybell, S. Winnerl, D. Stehr, M. Helm, and H. Schneider, **Simultaneous time and wavelength resolved spectroscopy under two-colour near infrared and terahertz excitation**,
Review of Scientific Instruments **82**, 103107 (2011).
- 07/2011 S. Zybell, H. Schneider, S. Winnerl, M. Wagner, K. Köhler, and M. Helm, **Photoluminescence dynamics in GaAs/AlGaAs quantum wells under intersubband excitation**,
Applied Physics Letters **99**, 041103 (2011).

Other publications of the author:

- 02/2015 F. Schubert, S. Zybelle, J. Heitmann, T. Mikolajick, and S. Schmult, **Influence of the substrate grade on structural and optical properties of GaN/AlGaN superlattices**,
Journal of Crystal Growth, *in press* (2015).
- 10/2006 C. V.-B. Tribuzy, S. Ohser, S. Winnerl, J. Grenzer, H. Schneider, M. Helm, J. Neuhaus, T. Dekorsy, K. Biermann, and H. Künzel, **Femtosecond pump-probe spectroscopy of intersubband relaxation dynamics in narrow InGaAs/AlAsSb quantum well structures**,
Applied Physics Letters **89**, 171104 (2006).
- 12/2004 H. L. Xu, M. Nilsson, S. Ohser, N. Rauhut, S. Kröll, M. Aguiló, and F. Díaz, **Hyperfine structure and homogeneous broadening in Pr³⁺:KY(WO₄)₂**,
Physical Review B **70**, 214115 (2004).

Acknowledgements

I'm grateful to many people for unfailing support over many years.

Manfred – for giving me the opportunity to write this dissertation and arranging for excellent working conditions

Harald – for your energy for long discussions, your patience, and your ability to handle problems in an unproblematic way

Stephan – for your continuous encouragement and enthusiasm, for your imperturbable interest and curiosity, and for your attachment to oddities

Jayeeta – for filling our office and labs with expertise and fun. Thank you for all the discussions about physics, and life beyond physics.

Martin, Martin, Martin, Uta, Daniel, Dominik, Rainer, Fabian, Markus, Johannes, Matthias, Falk, Faina, Carsten, Sanni, Wolfgang and many more colleagues at the HZDR – for friendly cooperation and a nice time together

Our collaborators Mackillo Kira, Stephan Koch, Lukas Schneebeli, Sangam Chatterjee, Benjamin Ewers, Benjamin Bredderman from the Philipps-Universität of Marburg, Jun Kono and Bill Rice from Rice University, Houston, Texas – for scientific impact and stimulating discussions

Peter Michel and his team – for providing us with free-electron laser pulses

Johannes Heitmann and my colleagues from the Institut für Angewandte Physik, TU Bergakademie Freiberg – for the guided tour through the GaN topic, the pleasant work environment, and open communication

Many thanks to my family and all my friends – for sharing the adventures in everyday life and for nights out

My *Young Investigators Group* Per Arne, Oskar, Freja, and Lutz – Danke!

Versicherung

gemäß §5(1) Nr. 5 der Promotionsordnung der Fakultät Mathematik und Naturwissenschaften der Technischen Universität Dresden.

Die vorliegende Arbeit entstand am Helmholtz-Zentrum Dresden-Rossendorf unter wissenschaftlicher Betreuung durch Prof. Dr. Manfred Helm, Professor am Institut für Angewandte Physik der Fakultät Mathematik und Naturwissenschaften der Technischen Universität Dresden.

Hiermit versichere ich, dass ich die vorliegende Arbeit ohne unzulässige Hilfe Dritter und ohne Benutzung anderer als der angegebenen Hilfsmittel angefertigt habe; die aus fremden Quellen direkt oder indirekt übernommenen Gedanken sind als solche kenntlich gemacht. Die Arbeit wurde bisher weder im Inland noch im Ausland in gleicher oder ähnlicher Form einer anderen Prüfungsbehörde vorgelegt.

Ich erkenne die Promotionsordnung der Fakultät Mathematik und Naturwissenschaften der Technischen Universität Dresden in der aktuell gültigen Fassung vom 23.02.2011 an.

Dresden,

Sabine Zybell